AN INVESTIGATION OF CRACK INITIATION AND PROPAGATION DURING NANOINDENTATION OF SILICATE GLASSES

A Dissertation

by

YVONNE CHANTAL DIEUDONNÉ

Submitted to the Graduate and Professional School of
Texas A&M University
in partial fulfillment of the requirements for the degree of

DOCTOR OF PHILOSOPHY

Chair of Committee,	George M. Pharr
Committee Members,	Hong Liang
	Ankit Srivastava
	Kelvin Xie
Head of Department,	Ibrahim Karaman

May 2023

Major Subject: Materials Science and Engineering

ABSTRACT

Glass surface damage is a major issue for glass makers, suppliers, and end users. The cracking behavior that governs glass surface damage is not yet completely understood. In many cases, fracture results from a sharp contact loading. Nanoindentation is a promising tool to replicate this sharp contact as it has various advantages: it does not require complicated sample geometries nor preexisting flaws in the material, as plasticity from the indent itself is assumed to create the precursor flaw.

Different aspects of the cracking behavior have been studied using nanoindentation with triangular pyramidal indenters with center-line to face angles in the range of cube corner (35.3°) to Berkovich (65.3°). Two different glass structures have been analyzed and compared: anomalous glass (fused silica) and normal glass (soda-lime glass), which deform primarily by densification and shearing processes, respectively. These different deformation processes are anticipated to lead to different stress fields around the contact resulting in different cracking morphologies. Nanoindentation at various loads (1 mN - 20 N) was used to identify a load dependency of the cracking behavior. Subsequently, surface and subsurface cracking was documented using atomic force microscopy, scanning electron microscopy, 3D laser scanning confocal microscopy, and focused ion beam cross-sectioning. Results show that cracking is enhanced by sharper indenters and higher loads. However, there exists a distinct crack initiation threshold, below which no crack formation can be observed, which is dependent on the glass system as well as the indenter geometry. In addition to crack initiation, the crack propagation has been analyzed using relations for the median-radial and Palmqvist-radial crack systems. Results show that the known relations are inadequate to fully describe the fracture toughness of the materials. However, differences in cracking morphology may have to be considered when determining fracture toughness obtained from indentation experiments.

CONTRIBUTORS AND FUNDING SOURCES

Contributors

Funding Sources

Abbreviations

ABS alumino-borosilicate

AFM atomic force microscopy

Ca calcium

DCB double cantilever beam

DT double torsion

FEA Finite Element Analysis

FQ fused quartz

FS fused silica

Ge germanium

HPFS high purity fused silica

LEM Lawn-Evans-Marshall

LSCM laser scanning confocal microscope

Na sodium

Pt platinum

SEM scanning electron microscopy

SENB single edge notched beam

Si silicon

Si$_3$N$_4$ silicon nitride

SLG soda-lime glass

SLS soda-lime silicate

SLSG soda-lime silicate glass

WC tungsten carbide

Symbols

a indentation size

α_M prefactor for the median crack theory

α_P prefactor for the Palmqvist crack theory

β indenter face angle

c crack length

d_{ind} indentation depth

$d_{plastic\,zone}$ plastic zone diameter

E modulus

ε_i effective indentation strain

H hardness

$P/c^{3/2}$ indentation fracture parameter for median cracks

$P/a \cdot l^{1/2}$ indentation fracture parameter for Palmqvist cracks

K stress intensity factor

K_c fracture toughness

k_0 free-surface correction factor

l crack length

L_C/L_F bowed-in parameter

m crack depth

ν Poisson's ratio

μ coefficient of friction

P load

P_c cracking threshold

ϕ center-line to face angle

ϕ_{ce} center-line to edge angle

$\phi_{eff,ex}$ excluded effective cone angle

ϕ_{eff} included effective cone angle

$r_{plastic\,zone}/a$ relative plastic zone size

σ stress

σ_y yield stress

τ_c Tabor constraint factor

TABLE OF CONTENTS

LIST OF FIGURES

LIST OF TABLES

1. INTRODUCTION AND LITERATURE REVIEW

1.1 Nanoindentation of Glasses

Nowadays, glasses are an omnipresent class of material in our lives. Especially the ongoing advancements in e.g., smart devices, have made glass an increasingly important material in today's community. For touch-screen applications, it is necessary to have a material that is transparent, thin, and strong. While glass certainly satisfies the first two criteria, it is a brittle material, so it cracks easily when contacted with a sharp object. While some of the issues are of aesthetic nature, cracks can also significantly influence the performance of a device or become a serious safety issue. To make a glass more durable seems to be an obvious step, but therefore, the first step is to understand the underlying mechanisms explaining why and how cracks form. The benefits of nanoindentation as a tool to answer these questions is two-fold. At small scales glasses deform plastically before they fracture. In macroscopic failure analysis, such as compression testing, the material shatters quickly into multiple pieces not allowing for a more detailed analysis of the cracking event. Stresses around an indentation impression decay quickly, allowing the cracks to arrest before catastrophic failure [1]. These cracks can then be analyzed for cracking morphologies, and their lengths can be measured allowing for fracture toughness calculations of the material. Additionally, impressions performed using nanoindentation only probe small volumes, so it can be assumed that the indentation itself is responsible for the crack formation and not preexisting flaws as originally assumed by Lawn and Evans [2]. Thus, nanoindentation allows to simulate the sharp contact event in a controlled manner. It also allows to investigate the influence of the shape of the sharp object using different shapes of indenters (Figure 1.1).

Historically, macroscopic hardness testing was done with a Vickers indenter (Figure 1.1a), but due to its four-sided pyramidal geometry, it is prone to chisel-edge
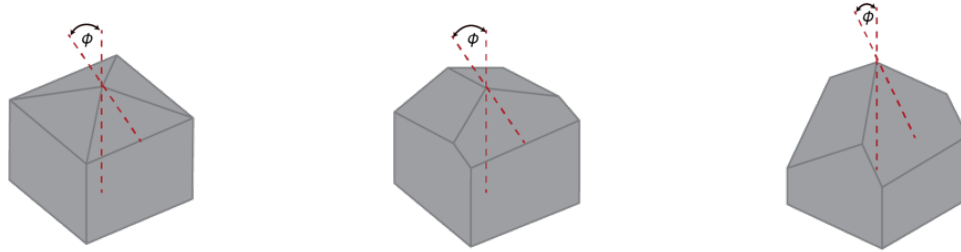
(a) Vickers: $\phi = 68°$ (b) Berkovich: $\phi = 65.3°$ (c) Cube Corner: $\phi = 35.3°$

Figure 1.1: Schematic illustration of different indenter tips typically used in nanoindentation. (reprinted from [3].)

development, which gives rise to large geometrical deviations from the ideal shape. For small-scale nanoindentation however, due to its sensitive nature, the geometry of the indenter must be well-known, and the indenter tip must be machined with highest precision. With advancements in nanoindentation, a three-sided Berkovich tip (Figure 1.1b) was created, that has a similar depth-to-area ratio as a Vickers, but due to the three-sided pyramidal shape, it allows for a precise tip manufacturing that avoids chisel-edge development issues [4]. The cube corner indenter (Figure 1.1c) is another common shape used in nanoindentation, which is also of three-sided geometry. Compared to the Berkovich indenter, it has a smaller center-line to face angle ϕ. This difference in ϕ makes the cube corner indenter significantly sharper, so that during the indentation process it displaces a larger volume, allowing certain deformation and fracture mechanisms to occur sooner.

1.2   Silicate Glasses

Glasses are a group of materials that can be defined as amorphous solids that only possess a short range atomic structure [5]. Silicate glasses are an important subcategory, and they can be divided into two classes, normal and anomalous glasses [6–8]. The respective mechanical behavior of those two categories is determined by the molecular structure of the material as seen in Figure 1.2. High purity fused

2

silica (HPFS), as a representative of anomalous glasses, consists of a three dimensional network of amorphous SiO_2. Its open network structure results in a significant amount of free volume, and it therefore deforms primarily by densification. Soda-lime silicate glass (SLSG) on the other hand, representing normal glasses, contains metallic ions, e.g., sodium (Na) and calcium (Ca), which occupy the free space in the network and deformation occurs by plastic flow, rather than densification [9]. Also, Na is a network modifier, which breaks up the strong 3D connectivity of the amorphous network and thereby allows for more plasticity by shear. While plastic or shear flow is a process that conserves volume, densification results in a volume change [8, 10].
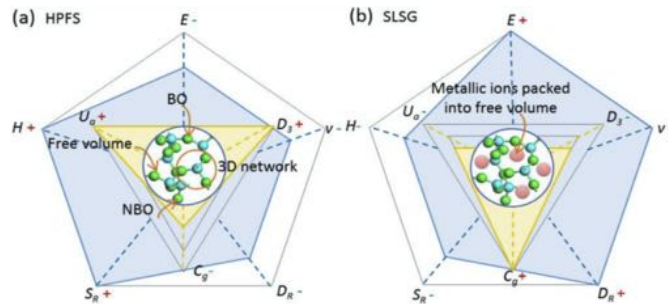
Figure 1.2: Differences between fused silica and soda-lime glass (reprinted with permission from [9]).

1.3 Crack Morphologies

The difference in deformation mechanism is thought to result in different cracking morphologies [11]. The most common morphologies introduced by nanoindentation are shown in Figure 1.3. A method to distinguish the cracking morphology is grouping the cracks by their location of occurrence. Cone (Figure 1.3a) and Palmqvist (Figure 1.3d) cracks start at the surface close to the contact periphery of the indentation, whereas median (Figure 1.3c) and lateral (Figure 1.3b) cracks initiate below the indentation at the elastic-plastic boundary. Another criterion is the direction of crack propagation. While cone and lateral cracks propagate predominantly parallel to the surface, median

and Palmqvist cracks propagate perpendicular to the surface and critically influence the component strength [7, 12–14]. Thus one major aspect of the current work will be to determine when and how the radial cracks (median and Palmqvist) form. Another crack morphology is the half-penny crack as shown in Figure 1.3e. This morphology could occur in two ways. It could have either started in the subsurface as a median crack and grow towards the surface as it propagates. Alternatively, it could have started on the surface as a Palmqvist crack and then grow down. In other words, if the load is high enough, it can not be determined anymore if the crack is of median or Palmqvist character.

(a) Cone   (b) Lateral

(c) Median   (d) Palmqvist   (e) Half-penny
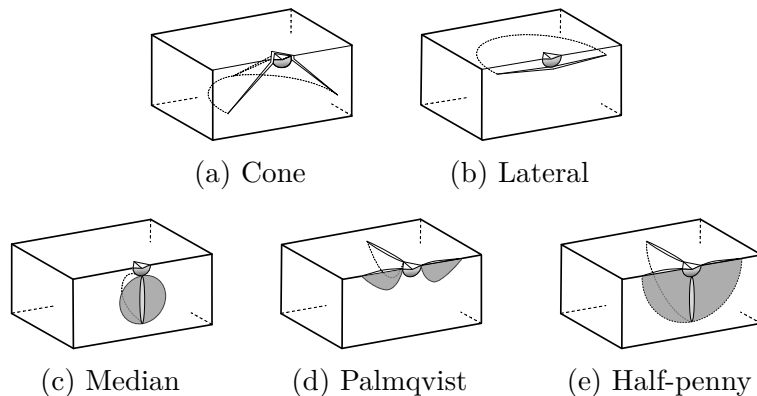
Figure 1.3: Most common crack morphologies introduced by nanoindentation (modified from [14]).

Originally, the main focus of the work was thought to be on the initiation and propagation of the radial crack systems. An example of radial cracks is shown in Section 1.3. However, in recent literature another crack system was discovered, which is only reported very sparsely, but seems to play a significant role in the initiation of radial cracks. These are called edge cracks [15–17], which grow along the contact periphery and are therefore also sometimes referred to as borderline, picture frame, or circular cohesive cracks [9, 18–20]. Figure 1.4b shows an example of this crack morphology. From a sub-surface view, these cracks are very shallow and considered surface oriented [21].

4
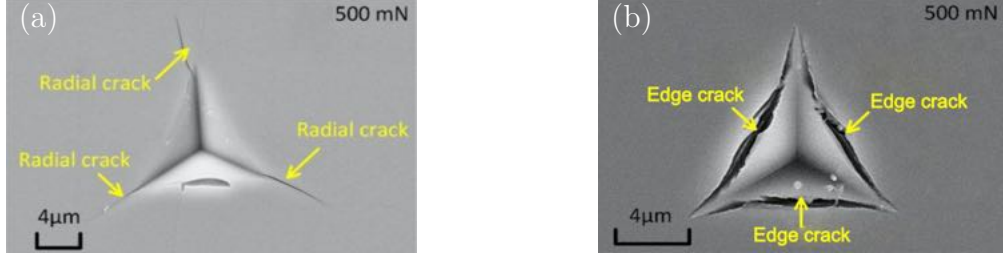
Figure 1.4: Comparison between (a) radial and (b) edge cracks (modified from [9]).

1.4 Crack Initiation

When and how a crack initiates and which crack morphology is dominant, i.e., initiates first, is determined by the indented material, the indentation load, and the indenter shape. Different research groups have found that a minimum load is needed for cracks to form around an indentation. A model to describe crack initiation was first presented by Lawn et al. [2, 22]. They assumed that if hardness H is a material property describing its resistance to deformation and fracture toughness K_c describes its resistance to fracture, then there has to be a combination of these two material properties to describe the brittleness or the onset of cracking of the material, which has the form described by

$$P_c = \Omega \cdot \left(\frac{K_c}{H} \right)^3 \cdot K_c \,, \tag{1.1}$$

where Ω is a material independent dimensionless parameter.

As shown in Figure 1.5a, using Hill's expanding cavity solution to describe the stress-field around the indentation and based on the assumption that there are preexisting flaws conveniently located at the elastic/plastic boundary, then the non-dimensional parameter Ω is about $2 \cdot 10^4$.

Another critical assumption is that the preexisting flaw has to be big enough to initiate a crack. Given that the indent itself grows slower than the crack, every flaw smaller than the indent will be subsumed within the indentation impression resulting in a critical flaw size of at least the size of the indentation. Hagan [23] criticized this
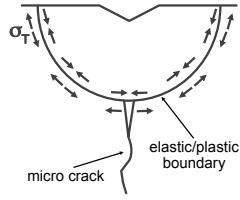
(a) Lawn and Evans (adapted from [2]).
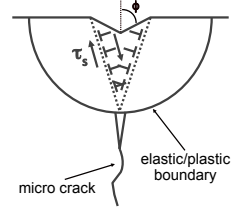
(b) Hagan (adapted from [23]).
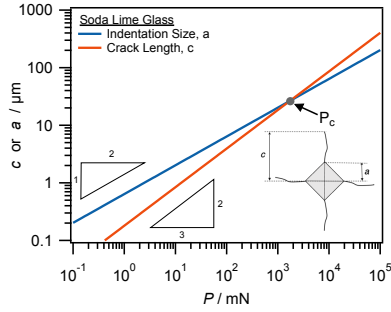
(c) Harding (modified from [24]).
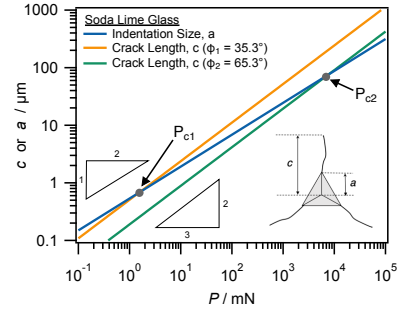
(d) Harding (modified from [24]).

Figure 1.5: Theoretical determination of the indentation cracking threshold for radial cracks based on different assumptions.

assumption based on the fact that in some materials, those flaws of critical size would have to be so big that they would be visible in the material. Since that is not the case, there has to be a different mechanism responsible for the onset of cracking around the indentation impression, which comes from the indentation process itself [23]. Hagan attributed the initiation of cracks to the pile-up of dislocations at intersecting slip lines, as depicted in Figure 1.5b. The intersection hinders further dislocation movement, giving rise to locally high tensile stresses that can open up a crack. Hagan's model also leads to the form of Equation (1.1) by using the dislocation pile-up model developed by Stroh [25] in the late 1950s. However, the value for Ω is approximately $1 \cdot 10^3$, which is an order of magnitude lower than predicted by Lawn et al.. When discussing amorphous materials, it should be noted that they do not have dislocations. However, the same concept would apply to shear bands or slip faults.

In 1995, Harding [24] developed a model based on the assumption that the indentation itself is the critical flaw and that the sharp corners of the indenter act as the

precursor. Similar to Lawn et al., Harding assumed that in presence of a load cracks grow faster than the corresponding indentation. So, for crack initiation, the critical point is the intersection of the crack length c and the indentation size a (Figure 1.5c). Using the well-established equations for H [26] and K_c [27] and assuming that crack initiation occurs when

$$c = \theta \cdot a \, , \tag{1.2}$$

where θ accounts for the corners of the indent not being perfectly sharp. In Harding's model, P_c is a function of the material properties hardness and fracture toughness once again following Equation (1.1), but instead of Ω simply being a dimensionless parameter, it is now material dependent in itself [24], through

$$\Omega = \frac{\theta^6 H^2}{8\alpha^4 E^2} \, . \tag{1.3}$$

Here, α represents an important parameter in the fracture toughness equation and will be discussed in detail in Section 1.5.1.

Figure 1.6a shows the dependency of the cracking threshold with respect to hardness and fracture toughness for different silicate glasses.

When comparing the materials to the aforementioned theories, it is obvious that Equation (1.1) describes the general trend well. However, the slope Ω, determined by the models of Lawn et al. and Hagan, significantly underestimates the actual material behavior by several orders of magnitude [8, 13, 28–32]. Harding's model, however, describes the cracking behavior for silicates and sodium-aluminosilicates well. Using $9\,\mathrm{GPa}$ and $72\,\mathrm{GPa}$ as typical values for hardness and modulus for silicate glasses, as well as $\theta = 1.48$ and $\alpha = 0.016$ for a Vickers indenter, then $\Omega \approx 3 \cdot 10^5$, which is very close to the slope for a fit through the data for silicates and sodium-aluminosilicates. The extremely high cracking threshold for the $PbO\text{-}ZnO\text{-}B_2O_3$ can not be predicted with any of the theories.
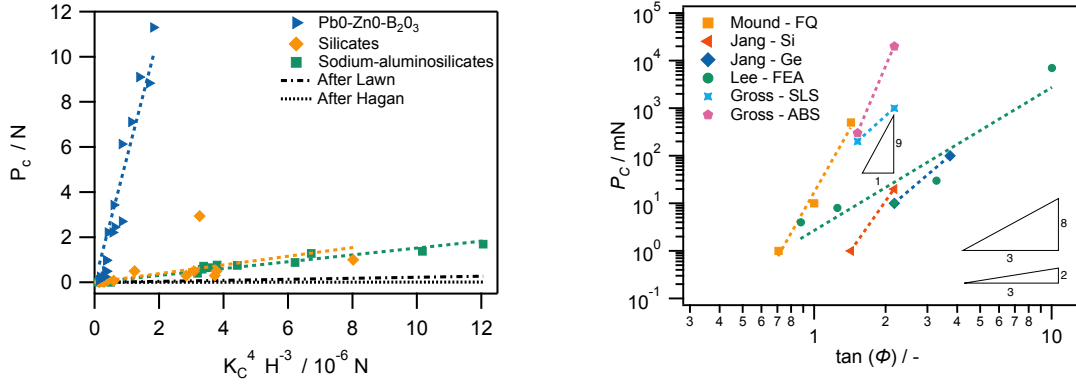
(a) Material dependency (modified from [31]). (b) Angular dependency (modified from [21]).

Figure 1.6: Dependencies of the radial cracking threshold for different glasses in comparison with the theories after Lawn and Evans [2], Hagan [23], and Harding [24].

Another important criterion when determining the cracking threshold is the shape of the indenter, the sharpness in particular, which can be described using the center-line to face angle ϕ. The smaller ϕ the sharper the indenter and the earlier the material starts to show cracks. Hagan's and Harding's models allow one to correlate the cracking threshold with ϕ; specifically, P_c is proportional to $(\tan \phi)^\kappa$. The power law exponent κ can be determined to be 2/3 using Hagan's model based on the Stroh crack approach and Hill's expanding cavity solution. Harding's approach, on the other hand, leads to a κ-value of 8/3. On a log-log plot of the cracking threshold as a function of the angle (Figure 1.6b), the slope is a measure of κ.

Similar to the material dependency (Figure 1.6a), experimentally observed dependencies of the cracking threshold on the indenter angle indicate that the cracking threshold does in fact scale with $\tan(\phi)$. However the 2/3 prediction from Hagan significantly underestimates the strong angular dependency. Harding's 8/3 prediction describes some of the materials better, e.g., soda-lime silicate (SLS) [33] and germanium (Ge) [34]. Finite Element Analysis (FEA) of a model material with parameters similar to silicon (Si) can be described as well [1]. However, experimental observations for silicon, as well as fused quartz (FQ) and alumino-borosilicate (ABS) can not be described with either theory.

8

For fused quartz, Mound and Pharr [21] concluded that the power law exponent κ is significantly higher at about 9. This indicates that the fracture mechanics origin of the cracking threshold remains not well understood, and additional work is necessary to explain the strong angular dependency for some materials.

While the median-radial crack system is most often discussed in literature, there is some more recent research documenting the formation of the edge cracks [9, 15–21]. However, that is primarily experimental observations for glasses and a limited amount of finite element analysis for other brittle materials, such as tungsten carbide-coatings. Similar to radial cracks, there are certain parameters that govern the onset of cracking. One of them is a material dependency. When comparing Figure 1.4a and Figure 1.4b, it should be noted that radial cracks form in soda-lime glass, while edge cracks form in fused silica, when the indentation conditions are exactly the same, namely an indentation with a Berkovich indenter to a peak load of 500 mN.

Additionally, there is also an angular dependency on the cracking threshold of edge cracks. Yoshida et al. suggested that the onset of cracking can be correlated to the extent of how much the edges of the indenter bow in [16]. As shown in Figure 1.7, the bowed-in parameter L_C/L_F is defined as the ratio between the length L_c, which is measured from the center of the indent to the corner of the indent and the length L_F, which is measured from the center of the indent to the center of the edge of the indent. Figure 1.7 shows the dependency of the bowed-in parameter on the indenter angle for indentations with a load of 1 N in soda-lime glass. For perfectly straight edges, L_C/L_F = 2.00, but it increases the more the edges bow in. The blunter the indenter, i.e., the smaller the indenter face angle β, the more bowed in is the edge of the indentation, increasing stresses at the midpoint of the edge. Those locations experiencing high stresses can serve as initiation points for edge cracks to form [15]. It should be noted that Yoshida et al. reported the exterior indenter angle β instead of the interior angle ϕ, thus $\beta = 90°\text{-}\phi$.
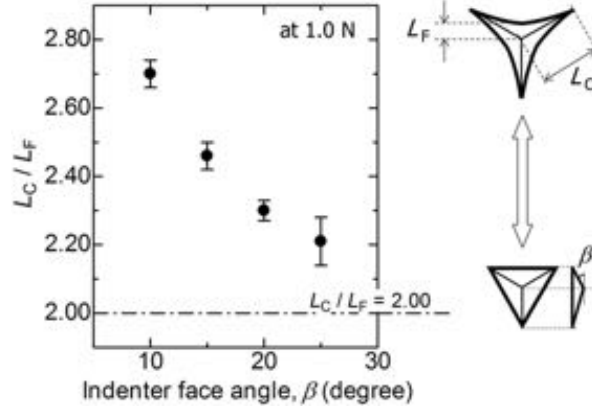
Figure 1.7: Bowed-in parameter (L_C/L_F) as a function of indenter angle (reprinted from [16]).

With increasing sharpness of the indenter, edge cracks form in an earlier stage of the load-unload cycle (Figure 1.8). For an indenter with an indenter face angle β of 10°, no edge cracks are initiated during the entire loading unloading cycle to a peak load of 10 N. For $\beta = 15°$ and $\beta = 20°$, edge cracks start to form during the unloading process at 5.8 N and 9.2 N, respectively. However, for a Berkovich indenter, with an indenter face angle of 25°, edge cracks form during loading at 6.1 N. Once an edge crack has started, either during loading or unloading, it continues to grow during the loading-unloading cycle [16]. In the sharpest case for the study by Yoshida et al., namely the Berkovich indentation, radial cracks can be observed in addition to edge cracks after full unload. Yoshida et al. [15] states that in those scenarios radial cracks may be the extension of the edge cracks.

1.5 Crack Propagation

Once the crack initiates, it propagates with increasing load P and arrests at distances away from the indent where the stress drops below the critical stress intensity. This allows for crack measurements and consequently fracture toughness K_c determination. Nanoindentation is extremely valuable when it comes to testing components at the micro- and nanoscale, where traditional fracture toughness measurements, such as double
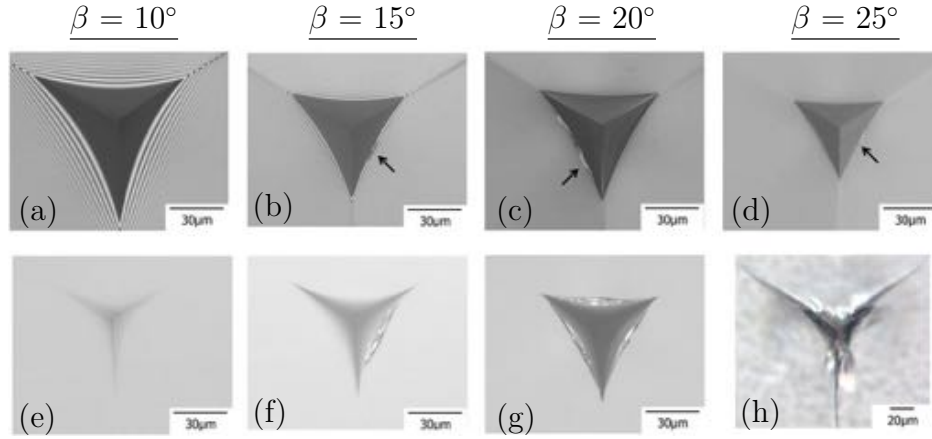
Figure 1.8: Angular dependency of the edge cracking threshold in soda-lime glass (reprinted from [16]). (a) at full load of $P = 10\,\mathrm{N}$, (b) and (c) during unload at $P = 5.8\,\mathrm{N}$ and $P = 9.2\,\mathrm{N}$, (d) during load at $6.1\,\mathrm{N}$, and (e-f) at full unload.

cantilever beam (DCB), single edge notched beam (SENB), or double torsion (DT), are not easily achievable since very small components do not offer enough material to machine the large standardized specimens required [35–37]. Additionally, machining those standardized samples can be very expensive and time consuming. Over the last 50 years, much research has been performed to find a method based on nanoindentation to overcome this drawback. The theory most often cited in literature is based on the measurements of median-radial cracks and was proposed by Lawn et al. [27] in the early 1980s. It is often referred to as the Lawn-Evans-Marshall (LEM) method in which the fracture toughness is computed from measured indentation parameters using

$$K_c = \alpha_M \cdot \left(\frac{E}{H}\right)^{1/2} \cdot \frac{P}{c^{3/2}}\,, \tag{1.4}$$

where α_M represents a dimensionless parameter, which was originally introduced to correlate the indentation fracture toughness to fracture toughness determined through conventional methods [38]. The values P, E, and H in Equation (1.4) can be determined from the nanoindentation test itself, where E and H need to be determined with a Berkovich tip, since the Oliver-Pharr method [26] only works well with that geometry, but breaks down as the indenter tip becomes sharper. The crack length c has to be

measured post mortem and is measured from the center of the indent to the corner of the crack as shown in Figure 1.9a and Figure 1.9b. Special attention has to be given to the prefactor α_M as it is not simply a dimensionless correction parameter. Its importance will be discussed in Section 1.5.1.

(a) Surface view.

(b) Subsurface view of median-radial crack.

(c) Subsurface view of Palmqvist-radial crack.
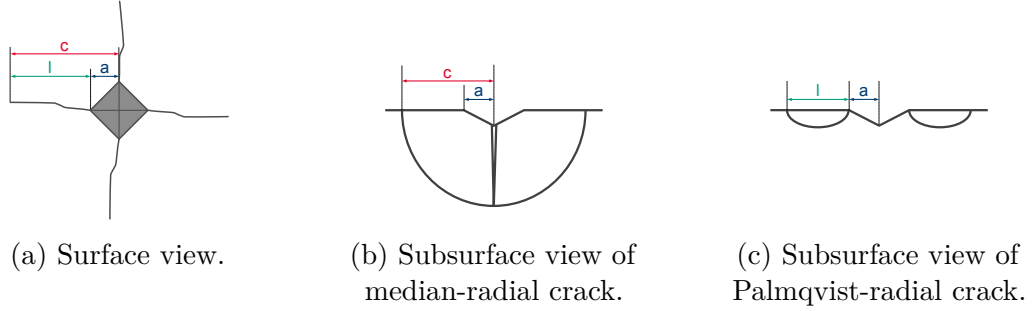
Figure 1.9: Subsurface differences between median-radial (adapted from [27]) and Palmqvist-radial (adapted from [39]) cracks.

Another crack system that has been used to measure fracture toughness is the one consisting of Palmqvist-radial cracks [39]. Compared to median-radial cracks, Palmqvist cracks form near the surface at the corner of the indentation (see Figure 1.9c). While both crack systems look similar when observing the surface of the material, they are significantly different in the sub-surface. When the load is high enough, they may also be similar in the sub-surface, but the origin of the crack is different [40, 41]. In the case of a Palmqvist-radial crack, Niihara et al. [42] proposed a relation based on the crack length l, see Equation (1.5), which is of similar form to the LEM-method

$$K_c = \alpha_P \cdot \left(\frac{E}{H} \right)^{2/5} \cdot \frac{P}{a \cdot l^{1/2}} \, ,$$
(1.5)

where α_P represents a dimensionless parameter.

The aforementioned methods differ in how the most important characteristic value, the length of the cracks, is measured. However, the Niihara method (Equation (1.5))

is not based on the crack length alone, but also incorporates the indentation size a. Furthermore, it should be noted that the exponent in E/H of the two theories differs from 1/2 in LEM's approach to 2/5 in Niiahara's approach. This difference comes from the fact that they both fit experimental results during their derivations to simplify the equations. In fact, different research groups have adjusted the original LEM method and determined exponents of 0, 1/4, and 2/3 in addition to the aforementioned values [43]. Compared to the difference in fitting parameters that determine the exponent of the different theories, the ratio of modulus and hardness is of much greater importance when comparing the different crack morphologies. The E/H-ratio describes how the material accommodates deformation. Based on Finite Element Analysis (FEA), Johanns et al. [44] found that if E/H is low, the material deforms primarily elastically, and is more prone to crack median-radially. However, if E/H is high, the material deformation is primarily plastic and the formation of Palmqvist-radial cracks is more likely (see Figure 1.10). This difference in behavior can be attributed to the effective indentation strain ε_i, which is proportional to E/H. The change in ε_i causes redistribution of the stress and strain fields under the pyramidal indenter. If ε_i is small, median cracks start at medium indentation depths. Large ε_i however, can not be easily accommodated by brittle materials, so cracks initiate at small loads [1].
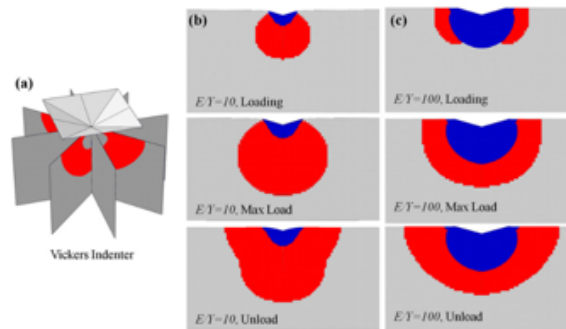
Figure 1.10: Influence on the E/H-ratio on the development of median-radial and Palmqvist-radial cracks based on Finite Element Analysis (reprinted with permission from [44]).

1.5.1 Prefactor α

Basing their analysis on the LEM method (Equation (1.4)) to determine the fracture toughness, Anstis et al. [36] suggested that $\alpha_M = 0.016 \pm 0.004$ would be a good calibration constant as an average for common brittle materials when the material is indented with a Vickers indenter. Pharr et al. [45] showed that the same constant can be achieved when using the three-sided equivalent Berkovich indenter and averaging multiple materials (Figure 1.11a). However, for both Vickers and Berkovich indenters, high loads (0.5–10 N) are required to introduce radial cracks [45]. Furthermore, in brittle materials such as FS and SLG, radial cracks are most often accompanied by other crack systems, such as cone and edge cracks. Therefore, it is questionable if the radial cracks alone can be used to determine the fracture toughness [38]. As a result, much research has been done to determine whether a sharper three-sided indenter, such as a cube corner ($\phi = 35.3°$) could be better suited for these measurements. In fact, sharper indenters lead to materials cracking at lower loads, because the additional volume displacements increase the stresses around the indentation [45]. Additionally, Bruns et al. [38] showed that cube corner indents in fused silica only exhibit radial cracks and no other crack systems that might have to be considered in the fracture toughness analysis.

As shown in Figure 1.11, the prefactor α_M depends on the indentation angle and is higher for sharper indenters. Pharr et al. [45] determined α_M for a cube corner indenter to be 0.0319 as an average over different materials.

However, since the cracks initiate at very low loads when indenting with a cube corner, it does not take much to bring shallow lateral cracks and chipping into the picture. Small indentation loads yield very small indents, which can make it hard to image them accurately for measurements of the indentation size and the crack length. It is straight forward that finding an optimal angle forming big enough indents allowing for accurate measurements of the necessary quantities while still only introducing

14
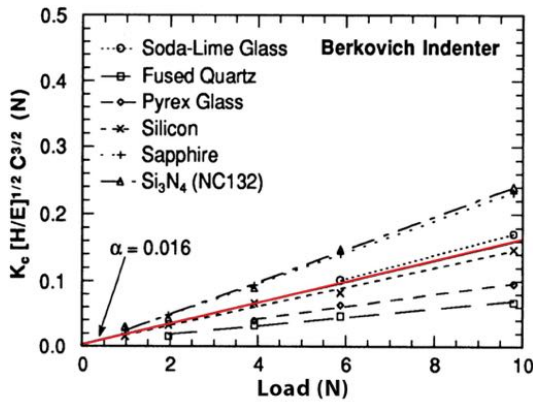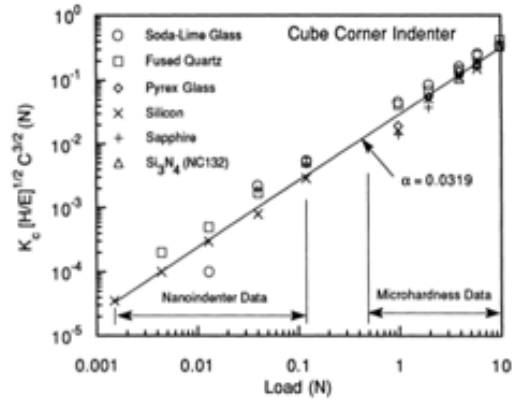
(a) Berkovich: $\phi = 65.3°$ (b) Cube Corner: $\phi = 35.3°$

Figure 1.11: Experimental determination of the prefactor α_M (reprinted with permission from [45]).

radial cracks during the indentation process is of great interest. Based on experimental comparison and theoretical relations between a Berkovich and a cube corner indenter alone, Harding [24] suggested that α_M is proportional to $(\cot\phi)^{2/3}$. Jang and Pharr [34] verified this angular dependency using three-sided indenters with center-line to face angles from 35.3–75° and two materials, silicon (Si) and germanium (Ge) (see Figure 1.12).
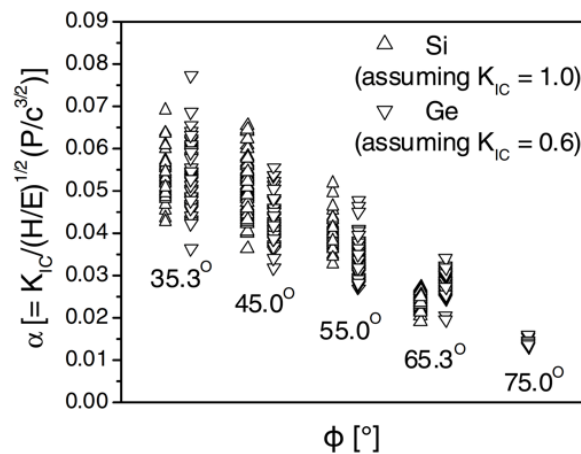
Figure 1.12: Angular dependency of the prefactor α_M using silicon and germanium as material examples (reprinted with permission from [34]).

15

While the angular dependency suggested by Harding [24] can be verified, the actual magnitude of α_M for a Berkovich and a cube corner indenter do not match the values originally reported [24, 27]. Carefully re-deriving the original analysis by Lawn et al. [27] using a three-sided indenter instead of a four-sided indenter, Jang and Pharr [34] showed that there might be a material dependency in the prefactor of the toughness relation (Equation (1.4)) given by

$$\alpha_M = \frac{0.0352}{1 - \nu}(\cot \phi)^{2/3} \, , \tag{1.6}$$

where ν is the Poisson's ratio of the material [34].

It should be noted that this analysis was performed using only two different materials (Si and Ge), so similar analyses are needed using additional materials in order to fully verify the expression suggested by Jang and Pharr [34]. Just for a cube corner indenter alone, α_M can range from 0.022–0.054 as shown by many different research groups in experimental and computational works for a variety of materials [24, 34, 45–50].

Irrespective of the exponent for the different expressions (Equation (1.4) and Equation (1.5)), it should be noted that if the crack is short $(c < 2.5 \cdot a)$, the fracture toughness is not proportional to $P/c^{2/3}$ anymore [42, 51, 52]. Instead, for short cracks, Niihara has suggested that K_c is proportional to $P/a \cdot l^{1/2}$ [42]. Figure 1.13 shows this change in behavior for different materials indented with a Vickers indenter. The vertical intercept on the log-log plot reflects the prefactor α when fitting the normalized fracture toughness as a function of c/a for materials that exhibit median-like cracking and l/a for materials showing Palmqvist-like cracking with a simple power-law relationship. For median-like cracking, α_M is determined to be 0.033, and for Palmqvist-like cracking, α_P is 0.009.

In Figure 1.14, K_c has been calculated as a function of load and c/a-ratio for independent data sets of Vickers indentation of tungsten carbide (WC) and silicon
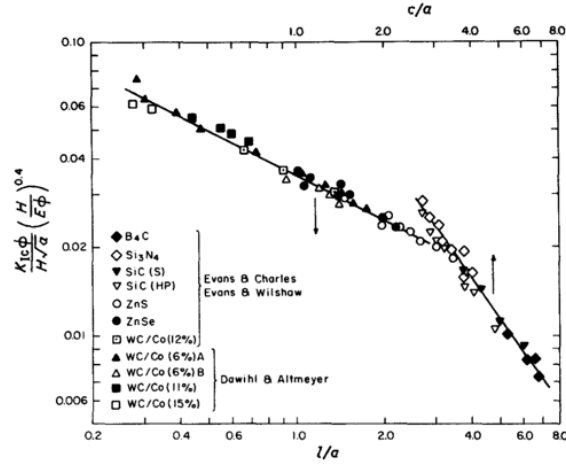
Figure 1.13: Normalized fracture toughness as a function of c/a and l/a showing the change in behavior for materials with median-like and Palmqvist-like cracks, respectively (reprinted with permission from [42]).

nitride (Si_3N_4). WC and Si_3N_4 are representative of the short crack range and long crack range in Figure 1.13, respectively.
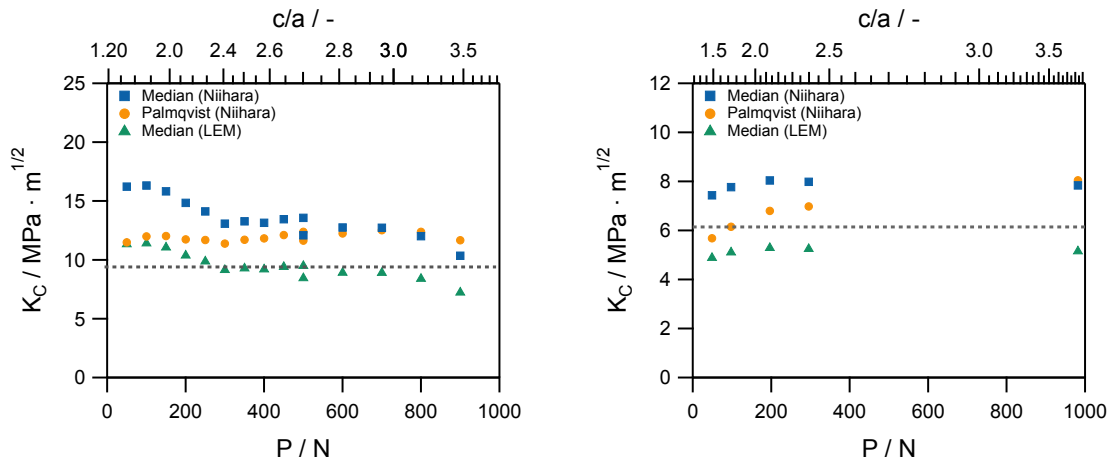
(a) WC-5.1%Co (with data from [53]).

(b) Si_3N_4 (with data from [54]).

Figure 1.14: Fracture toughness K_c measured using the different models [27, 42]. The gray dotted line shows the value of K_c determined with conventional methods.

The different expressions developed by Niihara et al. [42] and Lawn et al. [27] were used to calculate K_c using the prefactors determined by averaging over a variety of

17

materials. It is important to point out that for WC, the fracture toughness calculated assuming a median crack system decreases with increasing load, whereas K_c is constant when basing the calculations on the assumption of a Palmqvist-like cracking behavior (Figure 1.14a). In Figure 1.14b, on the other hand, Si_3N_4 exhibits the reverse behavior. Median cracking assumptions yield an approximately constant K_c, whereas, for the Palmqvist equation, K_c increases with increasing load. It should also be noted that this behavior is true for a range of c/a beyond 2.5. In the literature, this value is often suggested to be the transition value between median- and Palmqvist-like cracking behavior [52].

Irrespective of which cracking behavior is observed in a material, Figure 1.14 shows that simply using α as a dimensionless calibration constant does not yield a reliable value for the fracture toughness as determined through other conventional techniques (gray dotted line). Therefore, it is critical to continue research on α and its influential factors, such as the material dependency suggested by Jang and Pharr [34].

1.6 Summary and Proposed Work

Since its commercialization at the end of the 20th century, nanoindentation has been proven to be a promising tool to probe the mechanical behavior of materials. For brittle materials, glasses in particular, it is most critical to understand the cracking behavior. Much research has been performed using nanoindentation which indicates different crack morphologies are observed. The activation of these crack morphologies depends on the indented material and the indenter geometry. Radial and edge cracks are the two most important crack systems in the present work. It has been shown that for these cracks, there are distinct thresholds, which depend sensitively on the indenter angle and the indented material. However, conventional theories of the cracking threshold seem to fall short when describing the actual material behavior of normal and anomalous glasses. Theoretical relations between load, modulus, and hardness can be used to estimate the fracture toughness K_c of different materials, even for $c/a < 2.5$.

While past research has made significant progress on understanding the cracking phenomena in silicate glasses, there are several aspects that remain unclear. To gain further understanding on the mechanisms that govern cracking, the present research work is designed to answer the following questions:

- Which crack morphologies are activated in fused silica and soda lime glass? Do they affect each other's initiation?
- What are the cracking thresholds (radial and edge cracks) and the fracture toughness of soda lime glass and fused silica?
- Can existing theories be used to determine cracking threshold and fracture toughness? How can they be improved?
- What are factors that influence cracking threshold, fracture toughness, and crack morphology?

2. MATERIALS AND METHODS

To investigate the cracking behavior, systematic nanoindentation experiments on soda-lime glass (SLG) and fused silica (FS) were performed using a KLA iMicro Nanoindenter and a Zwick hardness tester with a customized indenter head. The resulting indents were then carefully imaged with different microscopy techniques, in particular atomic force microscopy (AFM), scanning electron microscopy (SEM), and 3D laser scanning confocal microscope (LSCM). The images were analyzed using a custom program developed in WaveMetrics Igor Pro to measure indentation size a and crack length c. Three key aspects that influence indentation cracking were considered. These were a material, load, and angular dependency as specified below in Section 2.1 and Section 2.3.

2.1 Materials

Two different glass structures with chemical compositions given in Table 2.1 were tested. These were soda-lime glass (SLG) microscope slides (type II per ASTM 438 – 92 [55]), representative of a normal glass, made by Corning Inc., and fused silica (FS) disks (HPFS 7980), representing anomalous glasses, likewise made by Corning Inc. Both materials belong to the group of silicate glasses, but they fundamentally differ in their primary deformation mechanisms, as discussed in Section 1.2. Indentation was performed on the as received samples.

Table 2.1: Chemical compositions for soda-lime glass (SLG) and fused silica (FS).

Material	Mass / wt%					
	SiO_2	Na_2O	CaO	MgO	Al_2O_3	K_2O
SLG	72	16	5	4	2	1
FS	100	-	-	-	-	-

2.2 Sample Preparation

The glass samples were mounted on an aluminum SEM pin stub mount using Crystalbond™ 509. Typically, the sample is directly mounted on a standard aluminum puck. Mounting the sample directly on the SEM mount saves the step of heating the sample to remove it from the standard puck and transfer it to the SEM mount for imaging. This ensures that the crack growth is not influenced by heat and manual handling during remounting. Special aluminum pucks as shown in Figure 2.1 that fit in the sample tray of the nanoindenter were machined. They were designed to have a hole in the center to fit the SEM mount, which was secured by an M3 set screw coming in from the side. It was verified that the frame stiffness was not significantly influenced by this set-up.
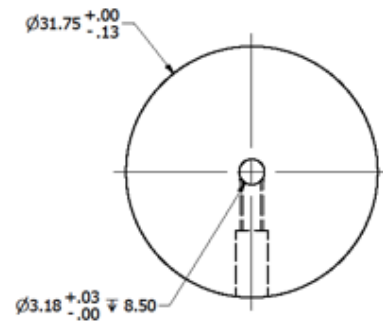
(b) Top view technical drawing.

(a) 3D Model.
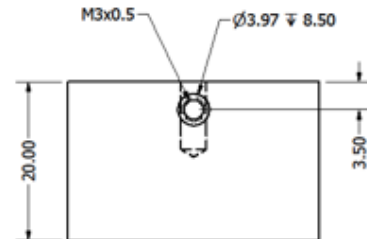
(c) Side view technical drawing.

Figure 2.1: Custom aluminum puck for indentation.

Figure 2.2 shows that copper tape was generously applied on the glued sample, leaving enough room for indentations. The copper tape helped with charging issues and hence image quality in the subsequent SEM imaging, and it provided an easy reference point for finding indentations during imaging at small scales.
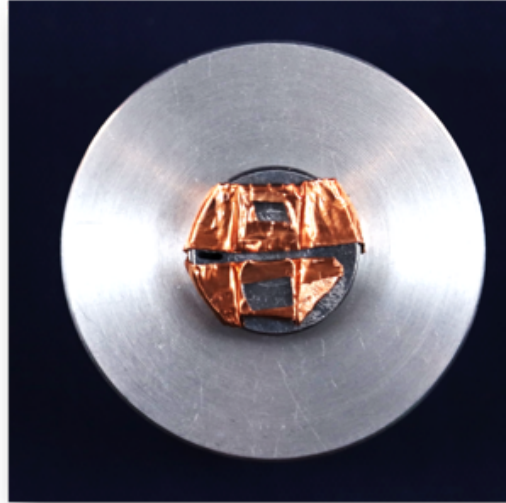
Figure 2.2: Samples prepared for indentation and subsequent imaging.

2.3 Indentation

During the indentation process, two different aspects that influence the cracking behavior were investigated, load and angular dependency. First, 10 indents each were performed at different peak loads ($1\,\mathrm{mN}$ - $20\,\mathrm{N}$), as seen in Figure 2.3a. Once severe cracking was observed, no additional load increase was performed. Additionally, the center-line to face angle (ϕ) was varied in four discrete steps $\phi = 35.3°$, $45.0°$, $55.0°$, and $65.3°$. According to ASTM C1327 − 15, the indents were spaced at least five times their crack length apart (Figure 2.3b) to ensure they do not influence each other's behavior. Although this standard was developed for the four-sided Vickers indenter [56], the same convention was used for the three-sided pyramidal indentations in this work.
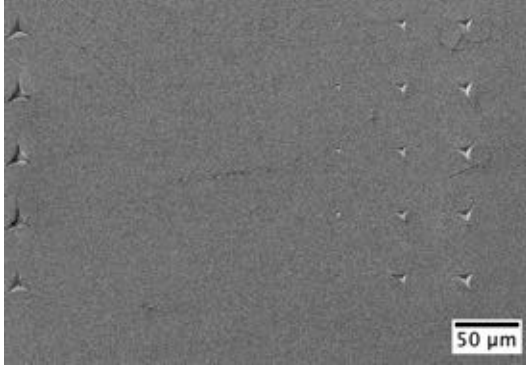
(a) Exemplary array of indents showing peak loads.
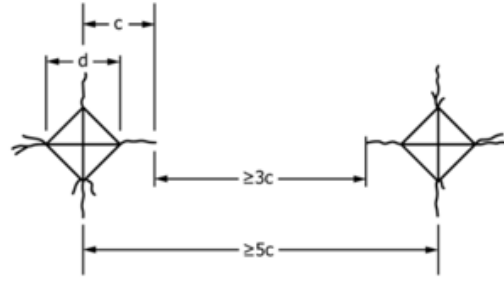
(b) Permitted minimum spacing.

Figure 2.3: Indentation according to ASTM C1237 - 15 [56].

2.3.1 Nanoindenter

Indentation in the smaller loading range was performed using a KLA iMicro Nanoindenter equipped with a 1 N load cell (Figure 2.4a). Peak loads of 1, 3, 10, 30, 100, 300, 500, and 1000 mN were tested for all indenter angles whenever possible depending on the severity of cracking. The 45.0° indenter yielded a distinct cracking threshold P_c for FS within a load range of 30–100 mN. These loads resulted in indentations big enough to image in great detail in the SEM, but at the same time small enough to perform automated serial sectioning, as discussed later in Section 2.4.1. For a more accurate determination of P_c and thus being able to perform subsurface analysis right at P_c, additional indents were performed at peak loads of $P = 65$, 70, 75, 80, and 85 mN. In order to analyze a material dependency of the subsurface cracking behavior, the same additional peak loads were tested for SLG. In addition, peak loads of 5, 7, and 9 mN were tested for SLG to determine P_c for the 45.0° indenter more accurately, as well. However, since P_c is relatively low and the indents were therefore relatively small, automated serial sectioning could not be performed around the cracking threshold for SLG.

The loading profile for the indentation with the iMicro is shown for a 100 mN indent in Figure 2.4b and can be described as follows: first, the sample was loaded using a

23

constant $\dot{P}/P = 0.05\,\mathrm{s}^{-1}$ to the desired peak load, here $100\,\mathrm{mN}$. The peak load was held for $10\,\mathrm{s}$. Before fully unloading, the sample was partially unloaded to $10\,\%$ of the peak load in $0.9\,\mathrm{s}$, at which it was held for $80\,\mathrm{s}$ to measure for thermal drift.
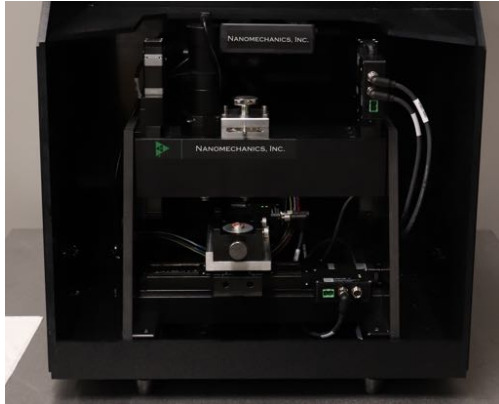
(a) Detailed view of KLA iMicro nanoindenter.
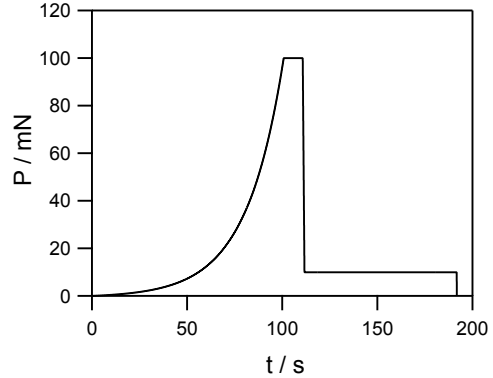
(b) Typical loading pattern.

Figure 2.4: Indentation at low loads ($1\,\mathrm{mN} \leq P \leq 1\,\mathrm{N}$).

Using a Berkovich indenter ($\phi = 65.3°$), material properties such as modulus E and hardness H were determined according to the Oliver-Pharr method [26]. E and H are needed for different analyses throughout the dissertation.

2.3.2 Hardness Tester

Indentations were also performed with a Zwick hardness tester to achieve higher loads (Figure 2.5a). This hardness tester is a dead-weight system and capable to apply nine discrete loads of 10, 25, 50, 100, 200, 300, 500, 1000, and $2000\,\mathrm{gf}$ ($\approx 100\,\mathrm{mN}$ - $20\,\mathrm{N}$), which were all tested for the $55.0°$ and the $65.3°$ indenter in SLG and FS. However, this hardness tester is only equipped with a four-sided Vickers tip. Consequently, a specialized adapter (Figure 2.5b) was manufactured, which allows the Zwick tester to be used with the same tips as used in the iMicro nanoindenter.

Since the Zwick hardness tester is calibrated for a specific indenter, it was deemed necessary to verify that the combination of adapter and tip in the Zwick tester yields
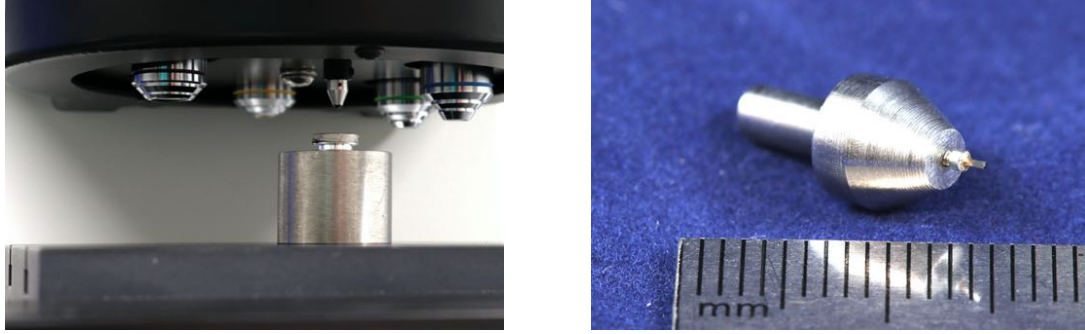
(a) Detailed view of Vickers hardness tester. (b) Custom made adapter for testing with triangular pyramidal indenters.

Figure 2.5: Indentation at higher loads ($100\,\text{mN} \leq P \leq 20\,\text{N}$).

the same results as when only the tip is used in the iMicro. In doing so, it was assumed that the tested materials are strain rate insensitive, since the loading profiles differ between the two instruments. For the hardness tester the load is applied in accordance with ASTM Standard E384 − 17 [57]. For accurate load measurements, the adapter was designed so that the combined weight of adapter and tip meets Zwick's requirements of $(1.50 \pm 0.15)\,\text{g}$. Figure 2.6 shows the comparison in terms of measurements of the indentation size a and the crack length c. A detailed description on how a and c were measured is provided later in Section 2.5.1.

(a) Indentation size a

(b) Crack length c
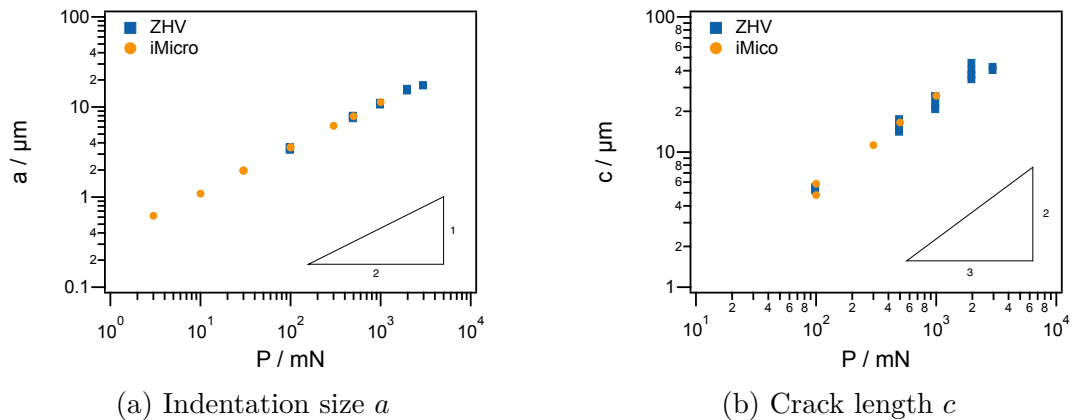
Figure 2.6: Comparison between Zwick Vickers hardness tester and KLA iMicro nanoindenter for indentation with a 55.0° indenter in SLG.

The Zwick hardness tester also allows to induce cracks with a Vickers indenter. The symmetry of this geometry may aid to distinguish whether the crack system in soda-lime glass and fused silica show median-radial or Palmqvist-radial characteristics.

2.4 Microscopy

Imaging was performed at least 12 h after indentation to account for delayed crack initiation and propagation [33]. Depending on the size of the indentation, imaging techniques of different resolutions were available for capturing the indentations and their surrounding cracks. Atomic force microscopy (AFM) was performed using either a Bruker Dimension Icon AFM or a MFP-3D™ Origin AFM by Oxford Instruments (Figure 2.7a). For best results, 512x512 scans were taken in tapping mode at a scan speed of 0.5 Hz. Prior to imaging the indentation, the condition of the tip was verified using a standard sample. Scanning electron microscopy (SEM) was performed on either a Tescan Lyra3 FIB-SEM or a Thermo Scientific™ Helios™ G4 CX DualBeam™ FIB (Figure 2.7b). To achieve the highest image quality, a working distance of 4 mm, an acceleration voltage of 2 kV, and a beam current of 170 pA was chosen for the SEM imaging. Lastly, for relatively large indents, a 3D laser scanning confocal microscope (LSCM) of type VK-X1100 manufactured by the Keyence Corporation was used (see Figure 2.7c). Due to the transparent character of the tested materials, the LSCM could also be used to draw some first order conclusions of the subsurface cracking behavior.
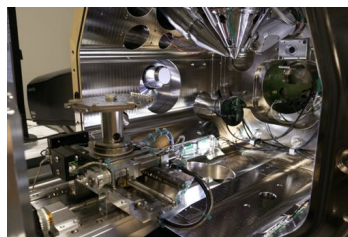
(a) AFM   (b) DualBeam FIB/SEM   (c) 3D LSCM

Figure 2.7: Different imaging techniques available for analysis.

In oder to be able to use data sets acquired from the different imaging techniques in the same analysis, it was verified that they do yield identical measurements of the indentation size a and the crack length c, as shown in Figure 2.8.

(a) Indentation size a (b) Crack length c
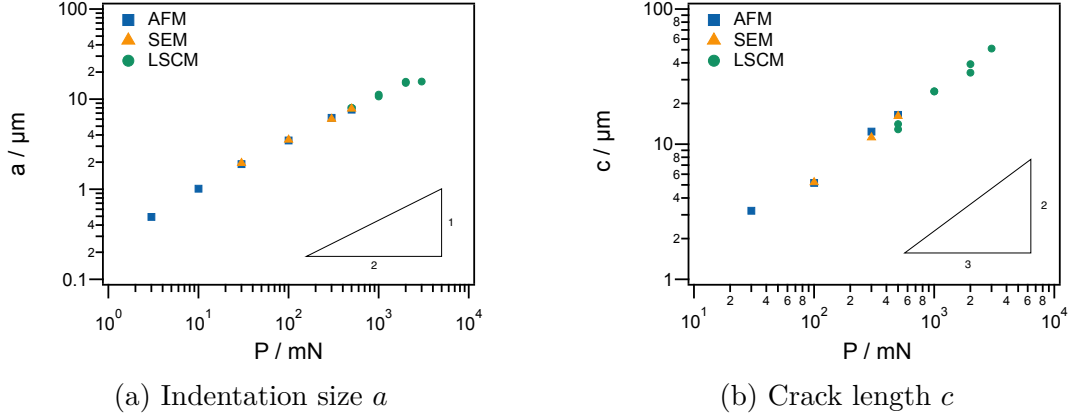
Figure 2.8: Comparison of measurements from images acquired from atomic force microscopy (AFM), scanning electron microscopy (SEM), and laser scanning confocal microscope (LSCM) for indentations with a 55.0° indenter in SLG.

2.4.1 FIB Tomography

Detailed subsurface analysis of both, three- and four-sided indentations, was performed using a gallium focused ion beam cross-sectioning in the Helios™ G4 CX DualBeam™ microscope. In order to perform fully automated serial sectioning, the samples were coated with a 4 nm Au/Pd coating to mitigate charging and drift issues. Figure 2.9 shows the benefits of the coating, as the charging streaks present in Figure 2.9a were prevented, as shown in Figure 2.9b.

For ten indents, each at three different loads ($P = 30$, 100, and 300 mN), indentation size and crack length were measured and compared between the coated and uncoated sample. Figure 2.10 shows that no significant difference could be observed. While the coating benefits the image quality enormously, it did not close up the cracks, which was initially a point of concern.

27

(a) Uncoated   (b) Coated with 4 nm Au/Pd.
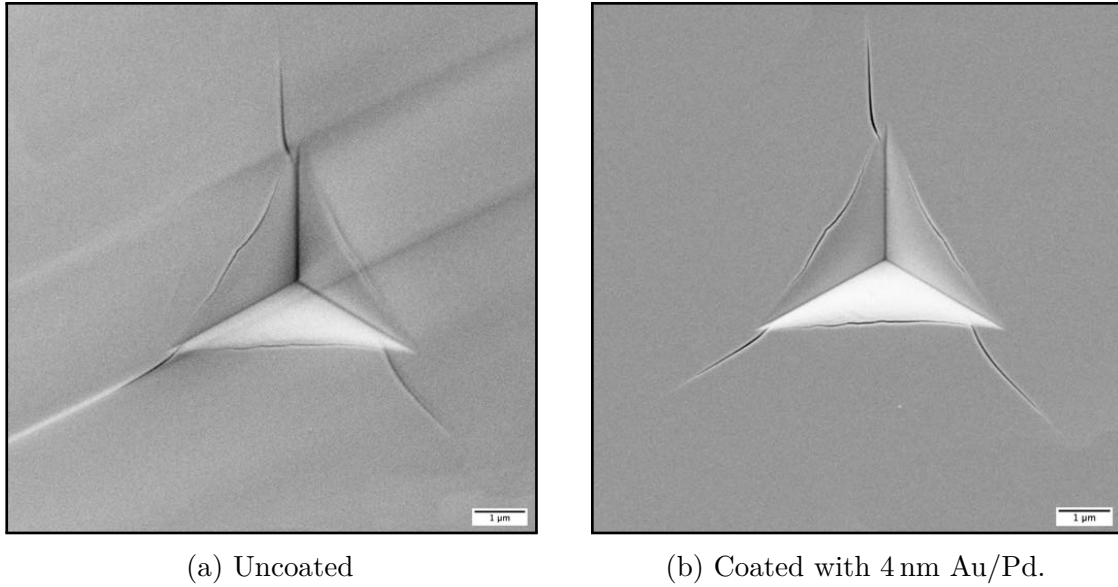
Figure 2.9: Coating influences on image quality exemplified for a 45.0°-indent in FS.
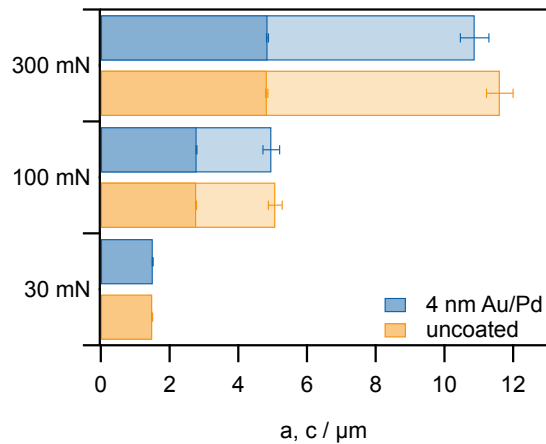
Figure 2.10: Comparison of measurements before (orange) and after (blue) a 4 nm Au/Pd coating for three different indentation loads. The indentation size a is displayed by the darker region, whereas the crack length c is displayed by lighter regions. The error bars describe one standard deviation for 10 indents.

Automated serial sectioning was performed using the Thermo Scientific Auto Slice and View 4 (AS&V4) software. The initial set up for the automation is displayed in Figure 2.11. Before preparing the sample for the serial sectioning, every indent was aligned so that one face was parallel to the cutting direction (see Figure 2.11a). In a

28

first step, a traveling fiducial for the e-beam as seen in Figure 2.11b is created. The traveling fiducial facilitates sectioning bigger indents, that are too large to use a digital beam shift. They can also be used in the subsequent three dimensional reconstruction, as it helps to align the individual slices in the Avizo software by ThermoFisher Scientific. Creating the traveling fiducial is described for a 25 µm x 25 µm big area of interest as follows: a 2 µm platinum (Pt) layer was deposited over the area of interest. Two micro trenches (100 nm wide and 1 µm deep) were cut into that platinum layer. The trenches were then filled with a 300 nm carbon layer, after which the entire area of interest was coated once more with a 2 µm platinum layer. The sequence platinum, carbon, platinum was chosen for maximum contrast between the sample and the protective Pt layer. Then trenches around the area of interest were milled. Those trenches allow for two things: the front trench reveals the subsurface of the site of interest and the side trenches act as areas for excess material re-deposition as the area of interest is milled. The depth of the trenches was chosen based on the crack length c around the indentation. Under the assumption of a perfect half-circular geometry of the crack, the trenches were cut at least as deep as c. As a final step, a static fiducial marker for the ion beam was prepared just above the area of interest, as shown in Figure 2.11a.

During the automated serial sectioning, 20–50 nm thick slices were milled, and after each milling process the new cutting face was imaged. The range in slice thickness results from the size difference of the indents that were analyzed. For run time purposes, it was chosen to acquire approximately 250 slices per indent; hence the slice thickness was adjusted accordingly.

Using the cross-sectional images that were taken during the automated serial sectioning, the crack morphology could then be reconstructed in all three spacial dimensions using state-of-the-art visualization and analysis techniques (Avizo). After the cross-sectional images were aligned using the traveling fiducial, the segmentation tool of the software allowed to trace the indentation itself and the individual cracks
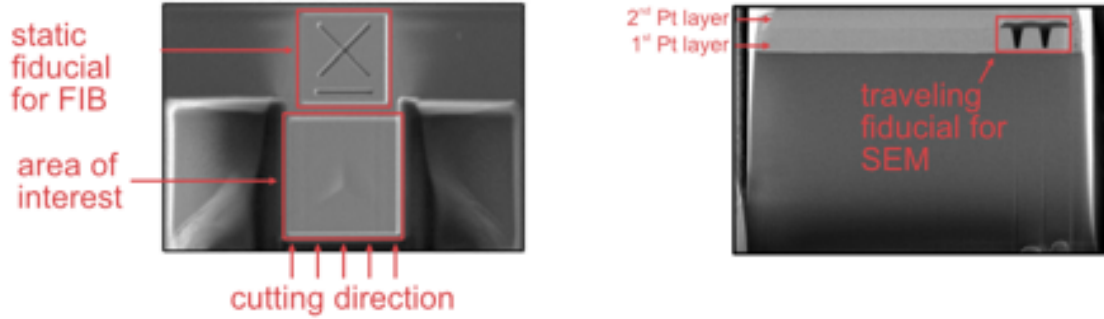
(a) FIB image of the prepared indentation. (b) Cross-sectional SEM view showing the traveling fiducial.

Figure 2.11: Overview of the initial set up to perform automated serial sectioning.

around it. The Avizo software also enabled visualization from the side as well as a top down view at different depths into the material based on interpolation of the initial images acquired during the serial sectioning. For improved image quality of the 3D visualization, the indentations and cracks were also traced in these two additional views.

2.5   Data Analysis

The micrographs acquired by the different imaging techniques were evaluated to determine the indentation sizes a and crack lengths c and l. These were then used to determine relevant aspects of the fracture process.

2.5.1   Indentation Size and Crack Length Measurements

As depicted in Figure 2.12a, a is measured from the center to the corner of the hardness impression. The difference in the crack lengths is that c is measured from the center of the hardness impression to the tip of the radial crack, whereas l is measured from the corner of the impression to the tip of the radial crack.

For statistical relevance, a significant number of images needed to be taken and analyzed. Commercially available software for image analysis is not capable of efficiently analyzing and storing the acquired results in a single file format. As a result, professional analysis software WaveMetrics Igor Pro 8 (Figure 2.12b) was used to develop a customized program to help facilitate the analysis. An easy to operate user interface

that provides clear instructions on the necessary steps for the analysis was included. Using Igor's project files, measurements are easily stored and could be reopened allowing all analysis steps to be retraced or adjusted if necessary.
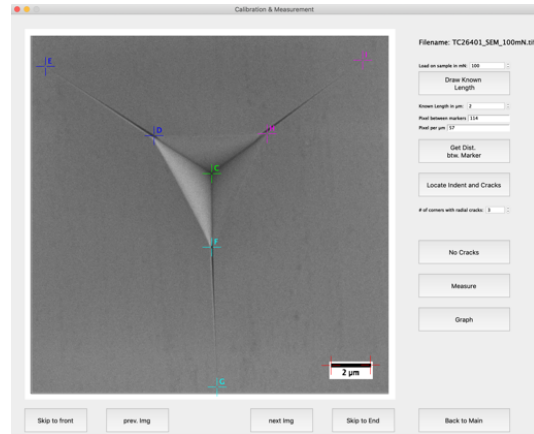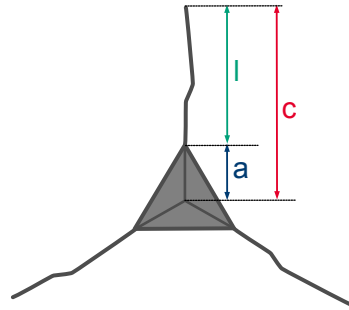
(a) Definition of the indentation size a and the crack lengths c and l.

(b) Customized analysis program built in Wave-Metrics Igor Pro 8.

Figure 2.12: Measurements of the important dimensions needed for analysis.

The Igor program allows one to load multiple images simultaneously. For each image, the indentation load in mN was entered in the user interface, and the scale factor in pixels per µm was determined using the image scale bar. Then, markers for the center of the indent (green C), corners of the indent (blue D , turquoise F and pink H), and tips of the cracks (blue E, turquoise G and pink I) were carefully placed in the image as shown in Figure 2.12b. Indentation size and crack lengths were computed as the length between the individual markers using Pythagorean theorem and the scale factor. The scale factor is needed because the distance between the markers is by default measured in pixels. For each indentation, all three indentation sizes and crack lengths were measured and averaged. The averages together with the stored loads were then used for continued analysis, likewise in Igor.

31

2.5.2 Cracking Threshold Determination

A cracking threshold P_c for each indenter geometry was initially determined optically based on the appearance of the first cracks. P_c in this work is defined as the load at which at least 50 % of the indentations show at minimum one crack. In a later stage, P_c was also determined using theoretical relations. For other aspects of analysis (e.g., determining the α-values, as seen in Figure 3.16 and Figure 3.30), α is a fitting parameter. The error of these α-values can be easily evaluated as the software used for data analysis (WaveMetrics Igor Pro 8) provides an error for the fitting parameter. Determining the error of P_c, however, is not straight forward. Therefore, the following method was used to establish the error. First, the c/a data was fitted using a linear fit of the logarithmic values. In doing so, the 95 % confidence bands were chosen to establish the error of the fit. The upper and lower confidence band were then approximated with a 5th degree polynomial fit. Multiple order fits were tested, but the 5th order fit described the behavior of the confidence bands most accurately. Lastly, the roots of the polynomial fits were calculated to find the upper and lower error of P_c. The individual steps of the method are shown in Figure 2.13.
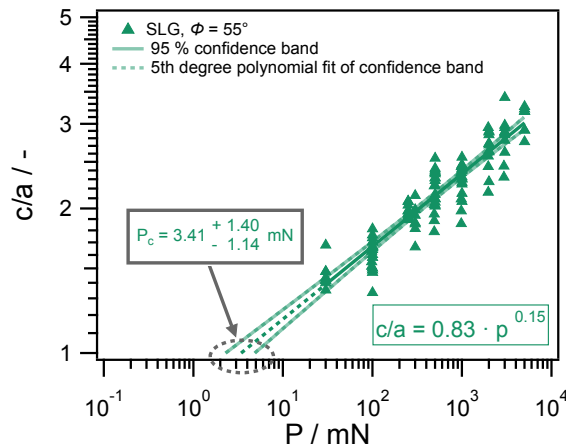
Figure 2.13: Method to determine the error for the cracking threshold P_c exemplified for soda-lime glass data using a 55.0° indenter.

3. RESULTS AND DISCUSSION

3.1   Crack Morphologies

Figure 3.1a shows an scanning electron microscopy (SEM) image of a cube corner indent in soda-lime glass (SLG) with a peak load of 100 mN. Radial cracks (red arrows in Figure 3.1a, b, and d) are observed at each indentation corner growing radially outward, which is a primary characteristic of the radial crack system.

This crack morphology can be observed at each peak load starting at 3 mN, before the material starts chipping at around 300 mN (Figure 3.3). When blunter indenters are used, the radial cracks initiate not exactly from the corners, but slightly offset along the edge of the indentation. Figure 3.1b shows an example of this behavior for indentation with a 45.0° indenter to a peak load of 10 mN in SLG. In some cases, there are additional cracks that also start offset from the indentation corner, or two cracks at each side of the corner with no crack emanating from the corner exactly. Shear faults, which have been discussed as initiation points for radial cracks [58], are a possible explanation for this kind of behavior. In the case of SLG, shear faults or any other obvious feature that could act as an initiation point for those radial cracks have not been observed in the surface image (e.g., Figure 3.1b) and might therefore not explain this atypical behavior. However, the discussed shear faults might be sub-resolution in size or apparent in the subsurface and could still act as crack starters.

In fused silica (FS), the lesser documented edge cracks (yellow arrows in Figure 3.1c and d) are also observed. For the given set of parameters ($\phi = 45.0°$ and $P = 65$ mN, see Figure 3.1c), edge cracks are already well developed, but they start at a low load of 3–10 mN. They typically begin in the center of the contact edge and grow outwards towards the corner, similar to observations in literature [15–17, 59]. When the load P is increased by 10 mN to 75 mN, Figure 3.1d shows that radial cracks start to initiate

(a) SLG, $\phi = 35.3°$, P $= 100\,\text{mN}$

(b) SLG, $\phi = 45.0°$, P $= 10\,\text{mN}$

(c) FS, $\phi = 45.0°$, P $= 65\,\text{mN}$

(d) FS, $\phi = 45.0°$, P $= 75\,\text{mN}$
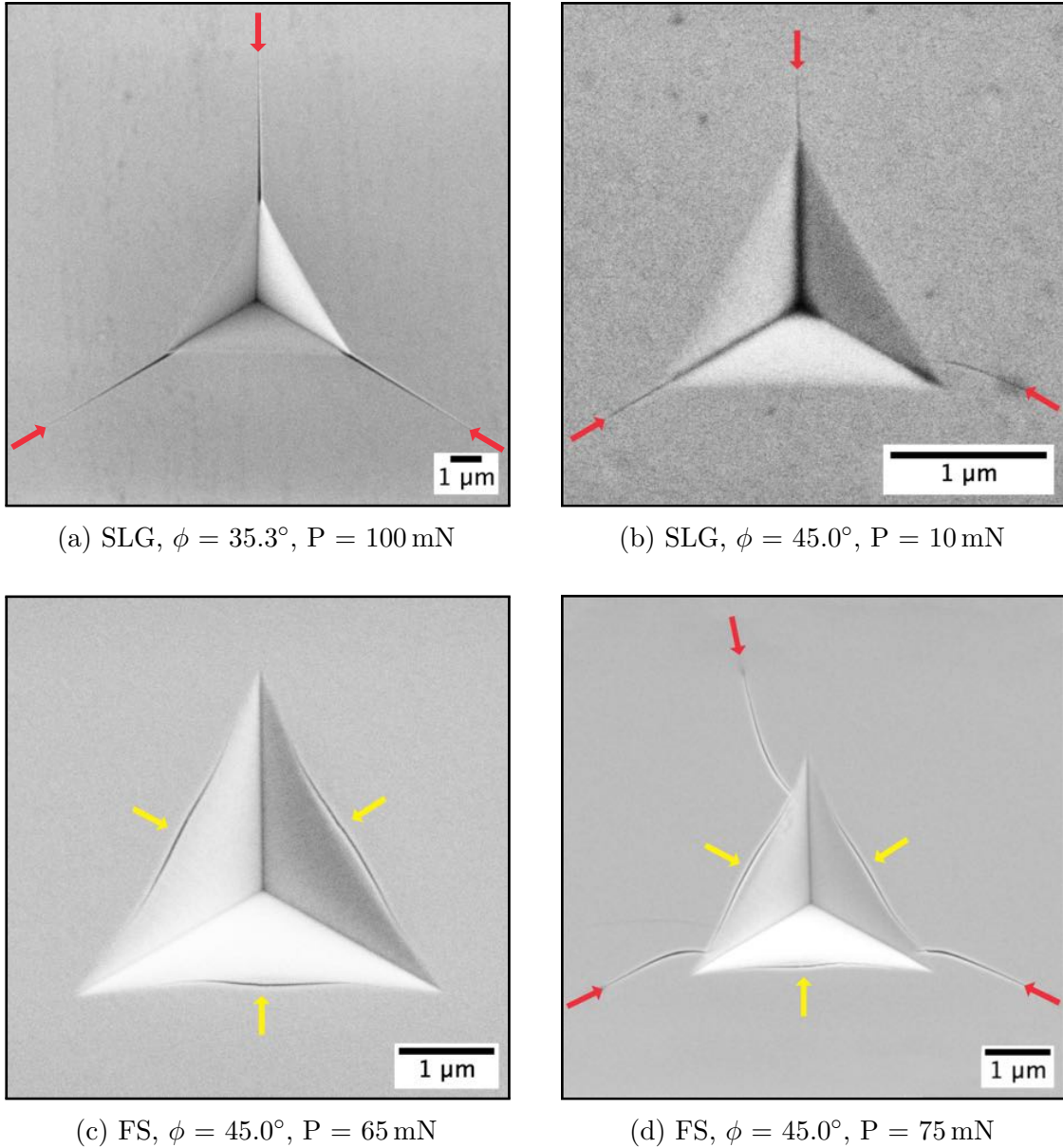
Figure 3.1: Scanning electron microscopy images revealing differences in crack morphology between soda-lime glass (a and b) and fused silica (c and d). Red and yellow arrows indicate radial and edge cracks, respectively.

and they seem to grow off of the edge cracks, which makes this sparsely documented crack system an important morphology in understanding the initiation of the radial crack system.

Figure 3.2 shows another example of the interaction between the edge and radial cracks as previously described. In Figure 3.2a a $P = 85\,\text{mN}$ indentation with a $\phi = 45.0°$

34
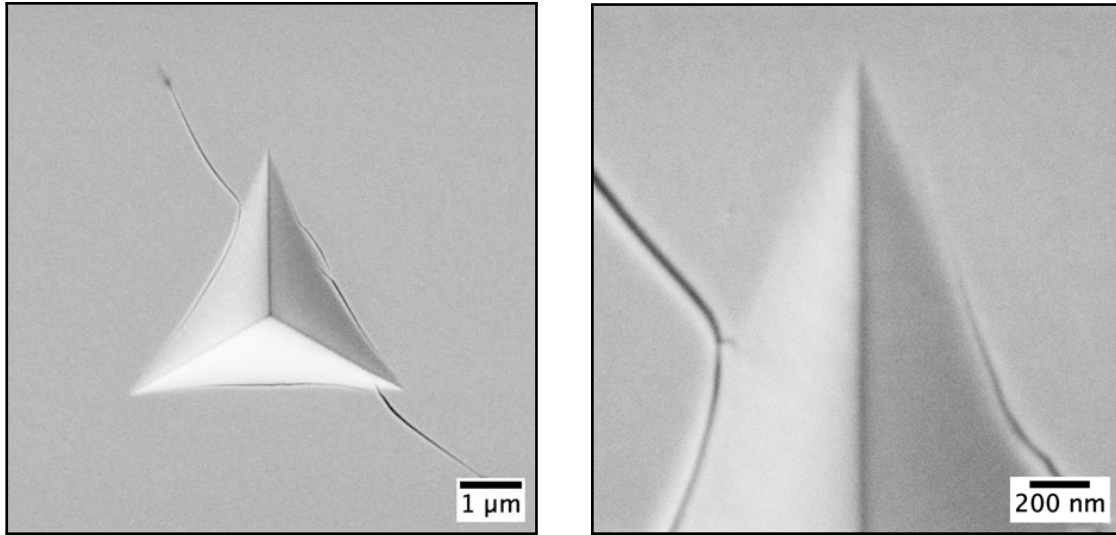
(a) Complete indent   (b) Detailed view of top corner.

Figure 3.2: SEM images showing the influence of edge cracks on the initiation of radial cracks for an 85 mN indent in FS using a 45.0° indenter.

indenter in fused silica is shown, and in Figure 3.2b a magnification of the top corner of the indentation is depicted showing clearly that the radial crack is emanating from the edge crack that has formed prior to the initiation of the radial crack. To verify this observation, subsurface analysis is necessary and of major importance to improve the understanding of the cracking behavior during nanoindentation, which will be discussed in section 3.5.

Figure 3.3 - 3.6 show an overview of the cracking behavior of SLG (Figure 3.3 and 3.4) and FS (Figure 3.5 and 3.6) for the four different angles and various discrete loads P = 3 mN - 5 N. The lowest load depicted is always the load just before which the first important crack morphology occurs. No further load increase was performed when severe chipping occurred around the indentation. The figures contain important cracking features for the two materials. However, here they present an overview of the cracking sequences and will not be discussed in detail, but will be referred to elsewhere.
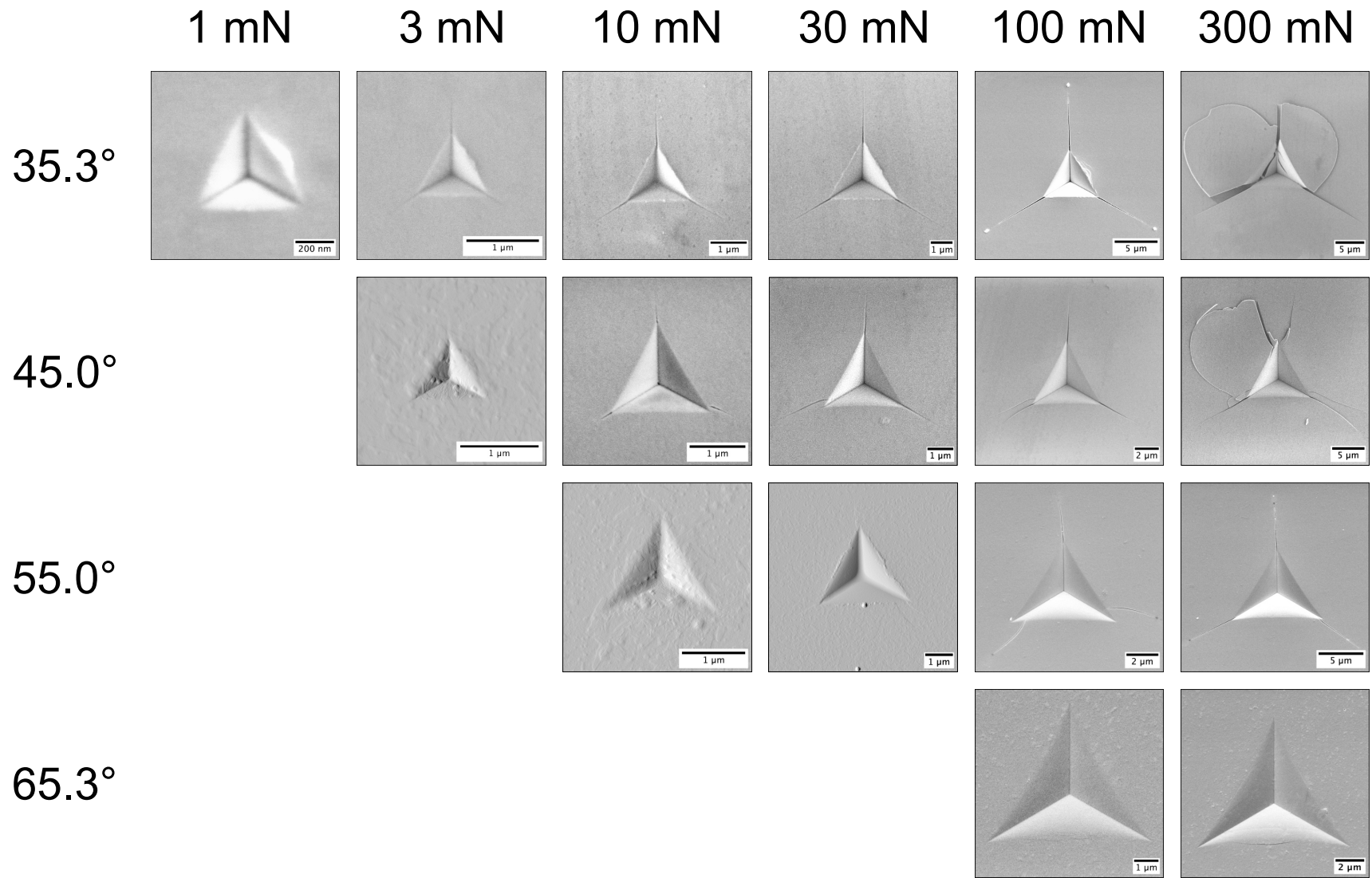
Figure 3.3: Influences of indenter angle and indentation load on the cracking behavior of soda-lime glass at low loads (1–300 mN).

500 mN   1 N   2 N   3 N   5 N

35.3°

45.0°

55.0°

65.3°
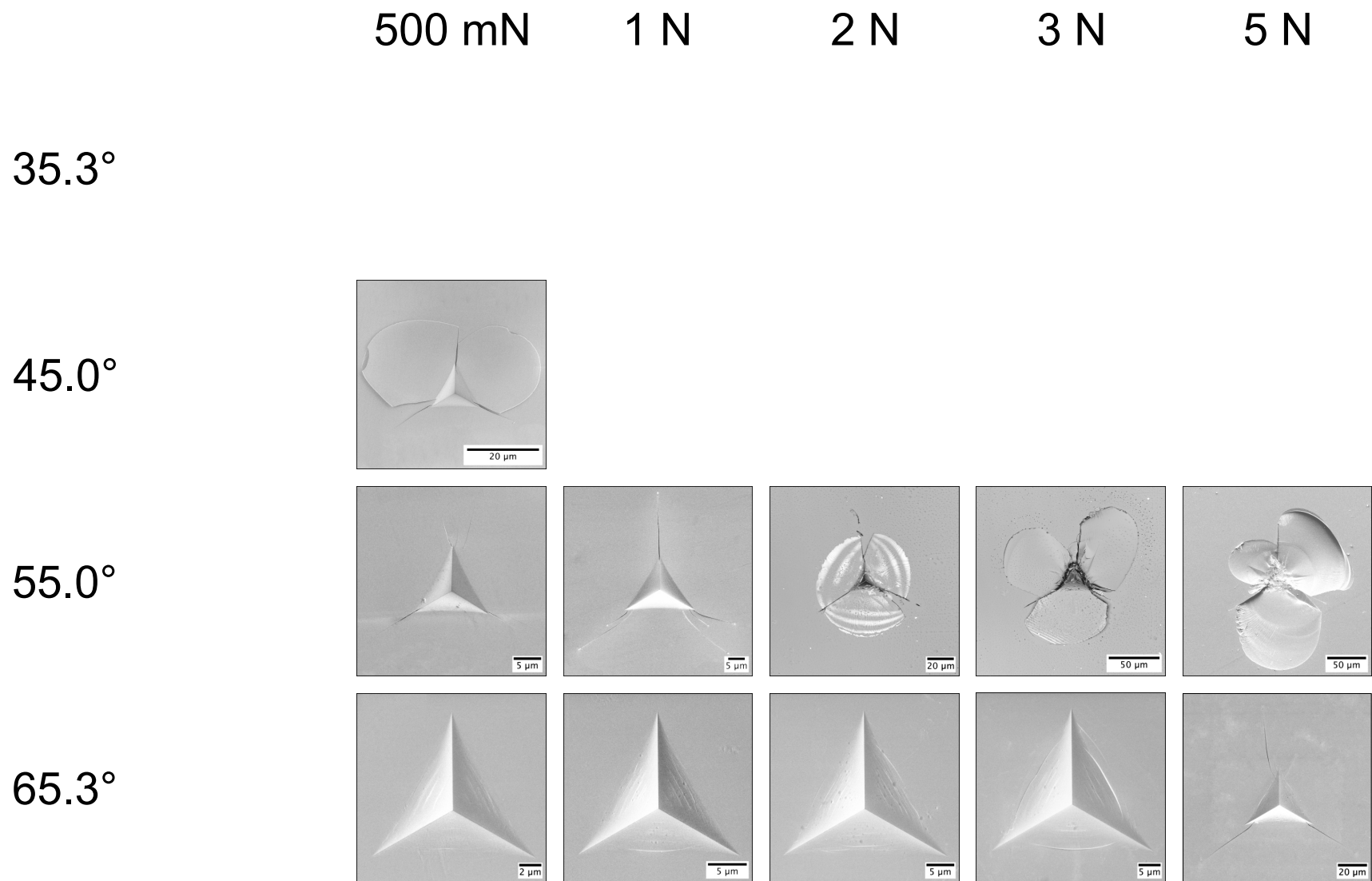
Figure 3.4: Influences of indenter angle and indentation load on the cracking behavior of soda-lime glass at high loads (500 mN - 5 N).

3 mN   10 mN   30 mN   100 mN   300 mN

35.3°

45.0°

55.0°

65.3°
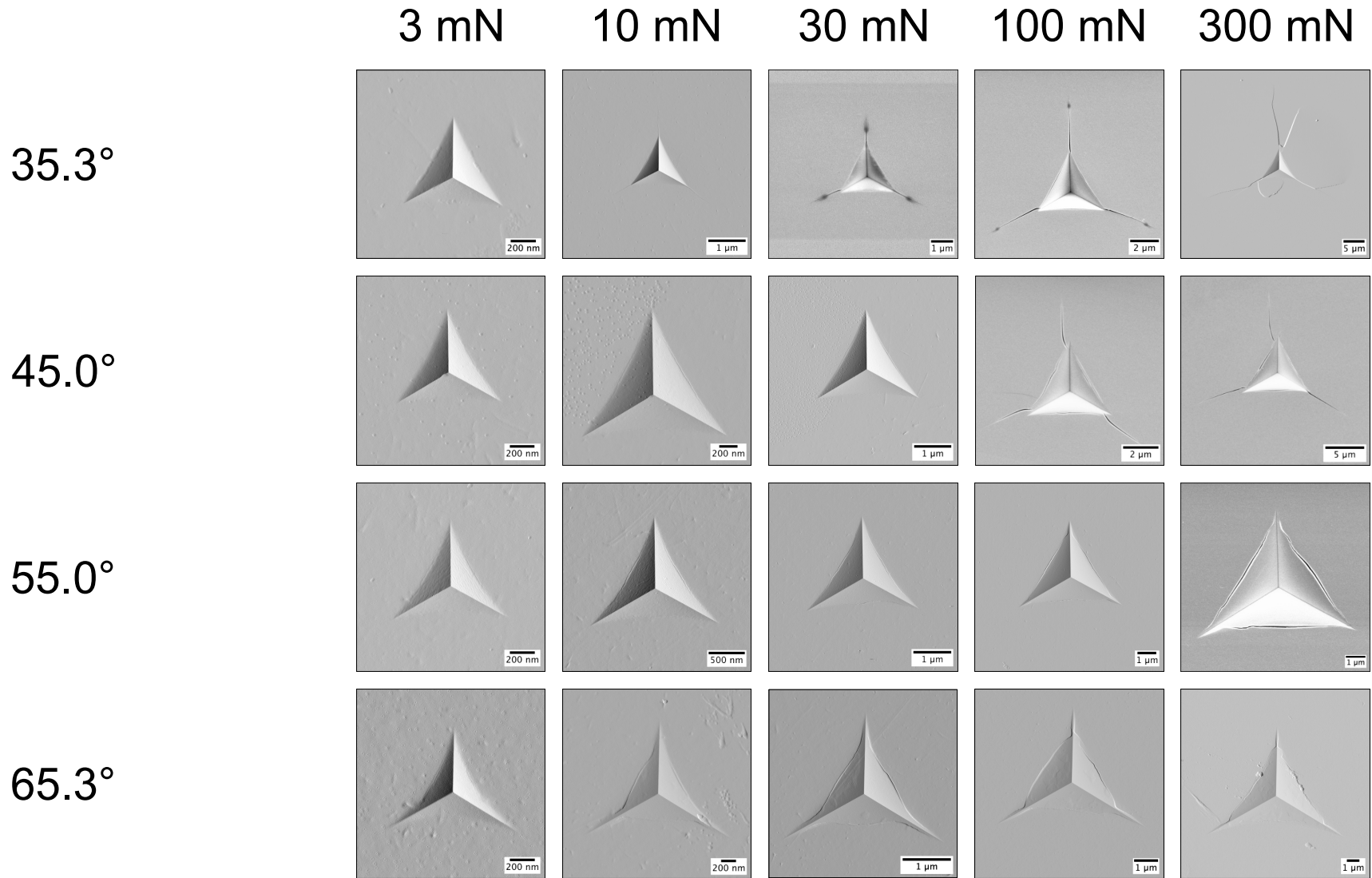
Figure 3.5: Influences of indenter angle and indentation load on the cracking behavior of fused silica at low loads (3–300 mN).

500 mN   1 N   2 N   3 N   5 N

35.3°

45.0°

55.0°

65.3°
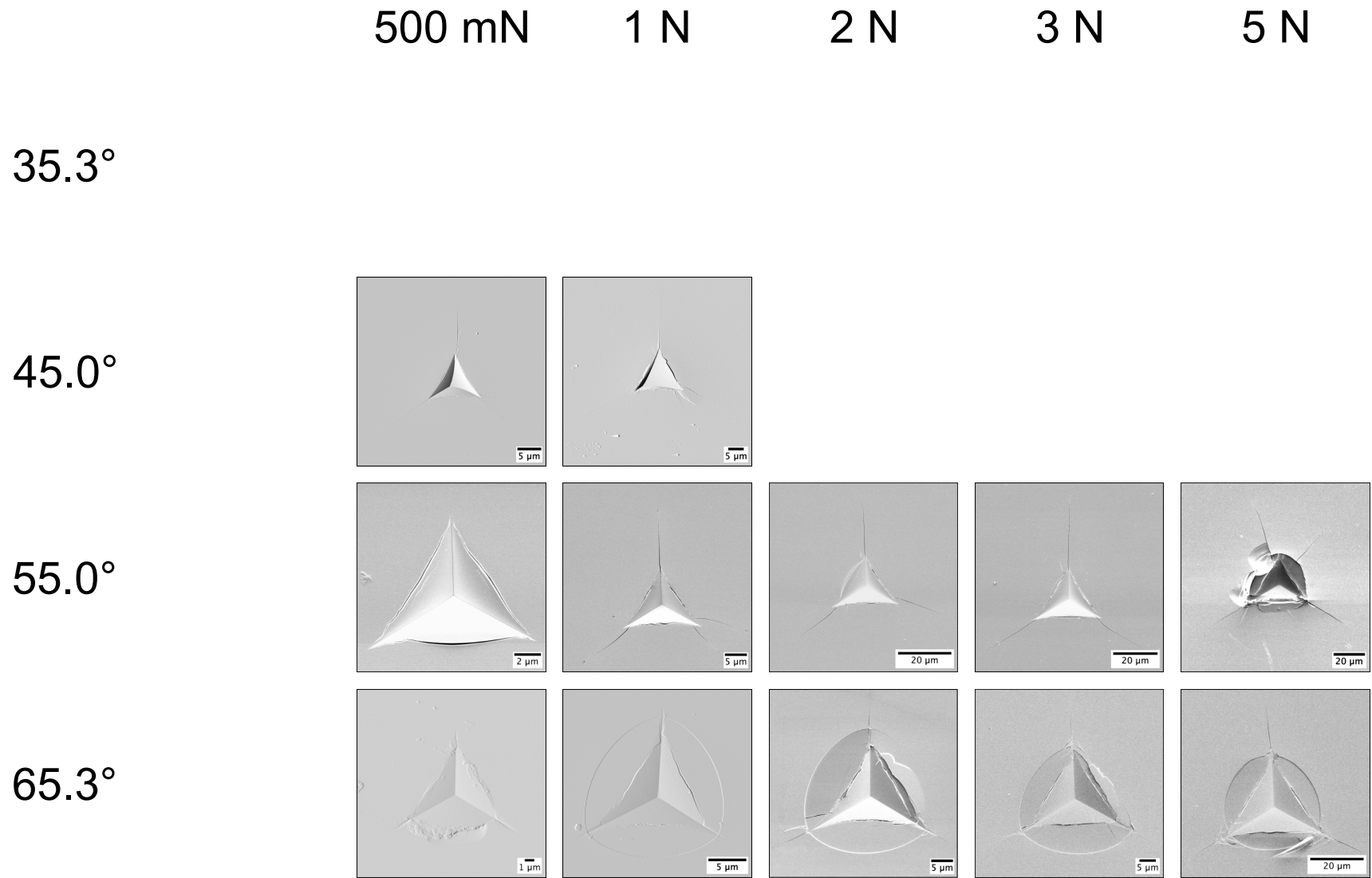
Figure 3.6: Influences of indenter angle and indentation load on the cracking behavior of fused silica at high loads (500 mN - 5 N).

3.2 Indentation Size and Crack Length

Indentation size a and crack length c are displayed on a double-logarithmic scale as a function of load P in Figure 3.7.

(a) Soda-lime glass (SLG)

(b) Soda-lime glass (SLG)

(c) Fused silica (FS)

(d) Fused silica (FS)
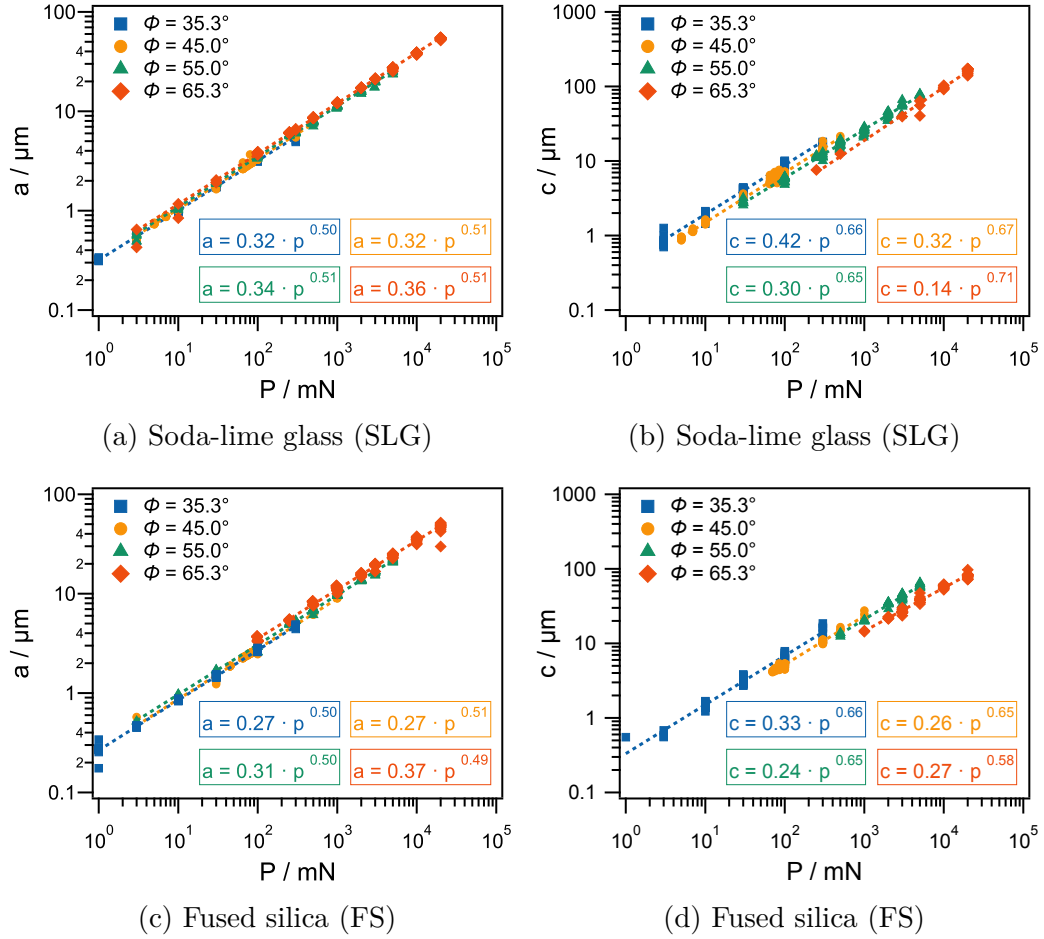
Figure 3.7: Indentation size a and crack length c as a function of load P for the studied materials.

In the tested loading range (1 mN-20 N), the indentation size a ranges from about 0.3–50 µm for SLG and FS in Figure 3.7a and c, respectively. For both materials tested the slope is close to the expected value of 1/2 for the indentation size. When the magnitude of the two different parameters is considered, it can be concluded that no

40

visible angular dependency is apparent for the indentation size, but there is one for the crack length. For blunter indenters, i.e. bigger ϕ, a lower crack length c is observed when compared at the same indentation load P (Figure 3.7b and Figure 3.7d). From the hardness equation, it follows that indentation size is proportional to $P^{1/2}$. The prefactor of the fitted relations is dependent on the hardness through

$$a = \left(\frac{4}{3\sqrt{3} \cdot H}\right)^{1/2} \cdot P^{1/2} \,. \tag{3.1}$$

Using the hardness values from Table 3.2, the prefactors for soda-lime glass (SLG) and fused silica (FS) are 0.33 and 0.29, respectively. This is in good agreement with the fitting parameters in Figure 3.7a and c. In Figure 3.7b and d, the crack length c increases with decreasing ϕ for both materials tested. Since there is an angular dependency for the crack length, a similar analysis to compare the prefactor to a theoretical value is not easily achievable. However, it is important to note that the expected relationship between c and P can be verified with a slope close to 2/3 for $\phi=$ 35.3–55.0°. For both materials, the relation for the Berkovich tip deviates from this theoretical value. It is slightly bigger for SLG (0.71) and slightly smaller for FS (0.58).

Figure 3.8a - d shows a direct comparison for the crack length c for the two tested silicate glasses, soda-lime glass (SLG) and fused silica (FS), at the four indenter angles tested. For all angles, the crack length for SLG is higher than for FS. The lower crack length for FS could come from the fact that FS as an anomalous material densifies during the indentation process. The densification reduces residual stresses around the indentation, which is a major driving force for crack propagation [62]. The shorter cracks resulting from the densification could also cause an overestimation of the fracture toughness [16].

Figure 3.8 also includes a comparison between the crack length measured in this work with experimental and FEA results from literature for the four different angles
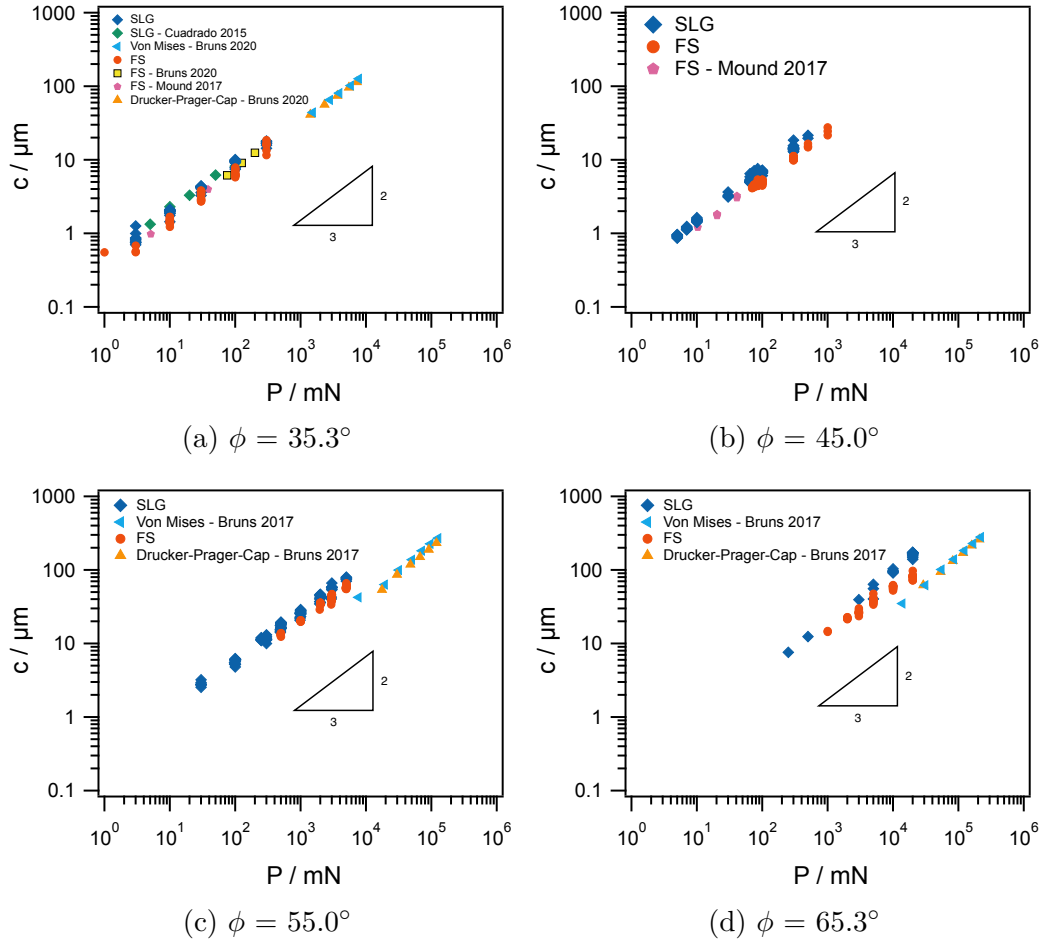
Figure 3.8: Crack length c measurements for different indenters in comparison with measurements reported in literature [38, 50, 60, 61].

tested [38, 50, 60, 61]. For the cube corner indenter ($\phi = 35.3°$ in Figure 3.8a) and the 45.0° indenter in Figure 3.8b, experimental results reported in literature [38, 60, 61] are similar to crack lengths measured here. Additionally, for the cube corner indenter, the FEA results of Bruns et al. [38] are in line with the current work, although calculated for higher loads. Typically, the von Mises criterion is used to describe normal deformation by shear flow, i.e. simulate SLG, whereas the Drucker-Prager-Cap model is used to include deformation by densification, as is the case for FS [9]. For the two other angles, FEA results are available, namely 55.0° in Figure 3.8c and 65.3° in Figure 3.8d, there exists an obvious offset to lower values from experimental to the FEA results. The offset

seems to yield a more severe angular dependcy of the crack length, but it could also just be a factor of the modeling parameters, since for the cube corner a true three-sided pyramid was used for the analysis [38], but an effective cone was used for $\phi = 55.0°$ and 65.3° [50]. The extra edges would introduce increased stresses in the edge area that would propagate cracks more easily. In addition, Yoshida et al. have shown that conical indentation produces more densification than pyramidal indentation, which would yield lower stresses around the indentation and ultimately shorter cracks [63].

3.3 Cracking Threshold

Analyzing all the images as exemplified in Figure 3.3 - Figure 3.6 for the different angles, loads, and materials, it can be concluded that it takes a specific condition for a crack to start, in particular, a certain load which is referred to as the cracking threshold P_c. The cracking thresholds for radial and edge cracks in soda-lime glass and fused silica are summarized in Table 3.1. P_c in this work is defined as the load at which a minimum

Table 3.1: Cracking Thresholds for edge and radial cracks based on surface observations.

ϕ / °	$P_{c,radial}$ / mN		$P_{c,edge}$ / mN	
	SLG	FS	SLG	FS
35.3	1 - 3	3 - 10	✗	3 - 10
45.0	3 - 5	65 - 75	✗	< 3
55.0	10 - 30	500 - 1000	✗	< 3
65.3	3000 - 5000	1000 - 2000	100 - 250	< 3

✗: No cracks observed in tested load range ($P = 1\,\mathrm{mN}$-20 N)

of half the indents analyzed show at least one crack. It should be noted that P_c is given as a range because only discrete loads were tested. The lower end of the range is the lowest tested load value that did not show any cracks, whereas the higher end of the

range represents the lowest tested load value for which cracks were observed. Hence, somewhere in this range the cracks initiated.

For radial cracks (left side of Table 3.1), it can be concluded that for both SLG and FS, the load necessary to initiate the crack increases with decreasing sharpness of the indenter, i.e, smaller center-line to face angles ϕ. Furthermore, when using the same indenter geometry, FS generally requires a higher load than SLG for ϕ smaller than $55.0°$. That is expected as FS is assumed to densify and the densifation is thought to reduce residual stresses around the indentation [8, 16, 31, 62–66]. For the Berkovich indenter ($\phi = 65.3°$), however, P_c is lower for FS. This observation is not a single occurrence in this work, but has also been documented by Harding [24].

On the right hand side of Table 3.1, the observations for edge cracks are summarized. While a significant angular dependency can not be determined, it should be noted that for sharper indenter tips ($\phi \leq 65.3°$), edge cracks initiate early on in FS (Figure 3.5), but there are no edge cracks in SLG(Figure 3.3 and Figure 3.4). Only with the comparatively blunt Berkovich tip, can edge cracks be initiated in SLG. In cases when edge cracks initiate they typically initiate prior to initiation of the radial crack (see Figure 3.3 - Figure 3.6 for detail). For $35.3° \leq \phi \leq 55.0°$ in SLG, the tested load is not high enough to initiate edge cracks, which is in accordance with observations by Yoshida et al. They concluded that a blunter tip has more bow-in and higher localized stresses yielding cracks that initiate at lower loads [16].

To determine if the surface observations for the cracking threshold P_c of radial cracks summarized in Table 3.1 can be described using theoretical relations, P_c is estimated using Harding's approach that the crack initiation occurs when the dimensions of the crack length c and indentation size a are identical (Figure 1.5c) [24]. If $c \ll a$, then the crack is subsumed in the hardness zone [22]. Compared to Figure 1.5c, where the intersection point is evaluated to determine P_c, c/a is shown as a function of load P in Figure 3.9. P_c can then be evaluated when the data is extrapolated to $c/a = 1$.

(a) Soda-lime glass   (b) Fused silica
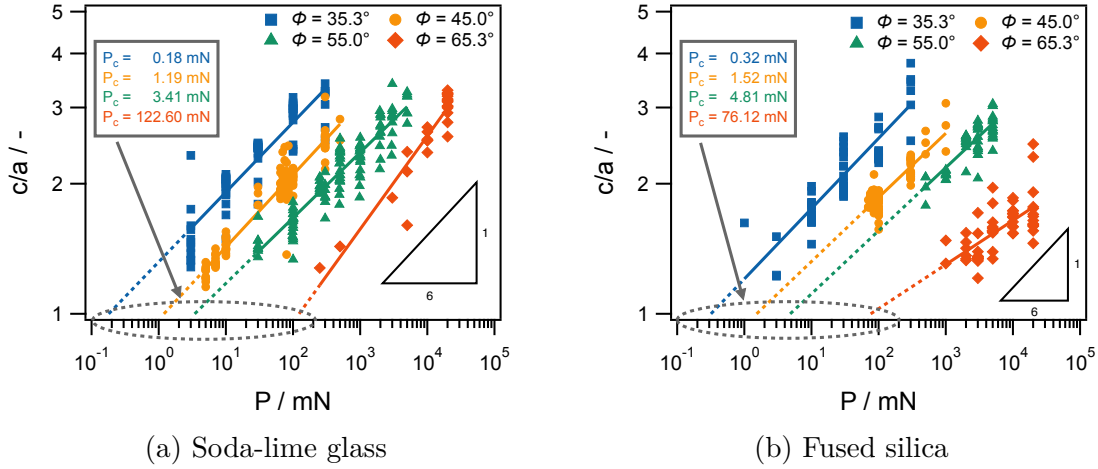
Figure 3.9: Determination of the cracking threshold based on Harding's Theory [24].

From theoretical derivations the dimension c/a is expected to increase with $P^{1/6}$ [34], which is in good agreement for both materials and angles up to $\phi = 55.0°$. This relationship breaks down for the Berkovich indenter ($\phi = 65.3°$). However, the deviation from the theoretical trend is different for the two tested materials. In SLG (Figure 3.9a) the slope is bigger than the expected value, whereas in FS (Figure 3.9b) it is smaller.

Figure 3.10: Cracking threshold P_c for radial cracks as a function of angle for soda-lime glass and fused silica. The error bars for the theoretical values are based of the 95 % confidence interval. For the observed values the data points are the averages of the provided loading ranges in Table 3.1, with the error being the minimum and maxium values of the range.

45

Similar to the conclusions from Table 3.1, Figure 3.9 shows a significant angular dependency of the cracking threshold. Different theoretical relations predict that the cracking threshold is proportional to $(\tan\phi)^{\kappa}$ [23, 24, 34]. Hence the different P_c determined by extrapolating the data for the tested angles is shown as a function of $(\tan\phi)$ in Figure 3.10. Given that the data is represented in a double logarithmic manner, it can be concluded that $P_c \propto (tan\phi)^{\kappa}$, and κ is represented by the slope of the log-log plot. The theory developed by Hagan [23] predicts a slope of 2/3, but none of the data follows that relationship. For the cracking threshold determined in Figure 3.9, both SLG and FS follow the angular dependency developed by Harding [24], as the slopes of the light blue diamonds and pink circles are close to 8/3. At least up to $\phi = 55.0°$. When the material is indented with a Berkovich indenter, the slope increases significantly to a value closer to 9. This drastic change in behavior can potentially be explained as follows: in the case of SLG, only radial cracks but no edge cracks are detected for angles up to $\phi = 55.0°$ (Figure 3.11a). For the Berkovich geometry in Figure 3.11b however, edge cracks initiate prior to the initiation of radial cracks (see also Figure 3.3 and Figure 3.3 and Figure 3.4), potentially already releasing stresses. Therefore, additional load is necessary to initiate the radial crack. For FS those edge cracks are present for every indenter geometry (e.g., Figure 3.5 and Figure 3.11c), but in the case of Berkovich indentation, an additional crack system is initiated prior to the initiation of the radial cracks, namely the so-called cone crack (Figure 3.11d). In summary, the introduction of an additional crack morphology influences the initiation of the radial cracks.

For the sharper angles, P_c of FS is higher than for SLG, but for the Berkovich geometry, P_c for SLG exceeds the one for FS.

While theoretical relations can be used to describe the angular dependency for P_c in SLG, another interesting value is the actual magnitude of the threshold load. Jang and Pharr [34] used an approach similar to Harding's [24] and determined P_c to be the point

(a) SLG, $\phi = 55.0°$, P = 250 mN

(b) SLG, $\phi = 65.3°$, P = 5 N

(c) FS, $\phi = 55.0°$, P = 1 N

(d) FS, $\phi = 65.3°$, P = 2 N
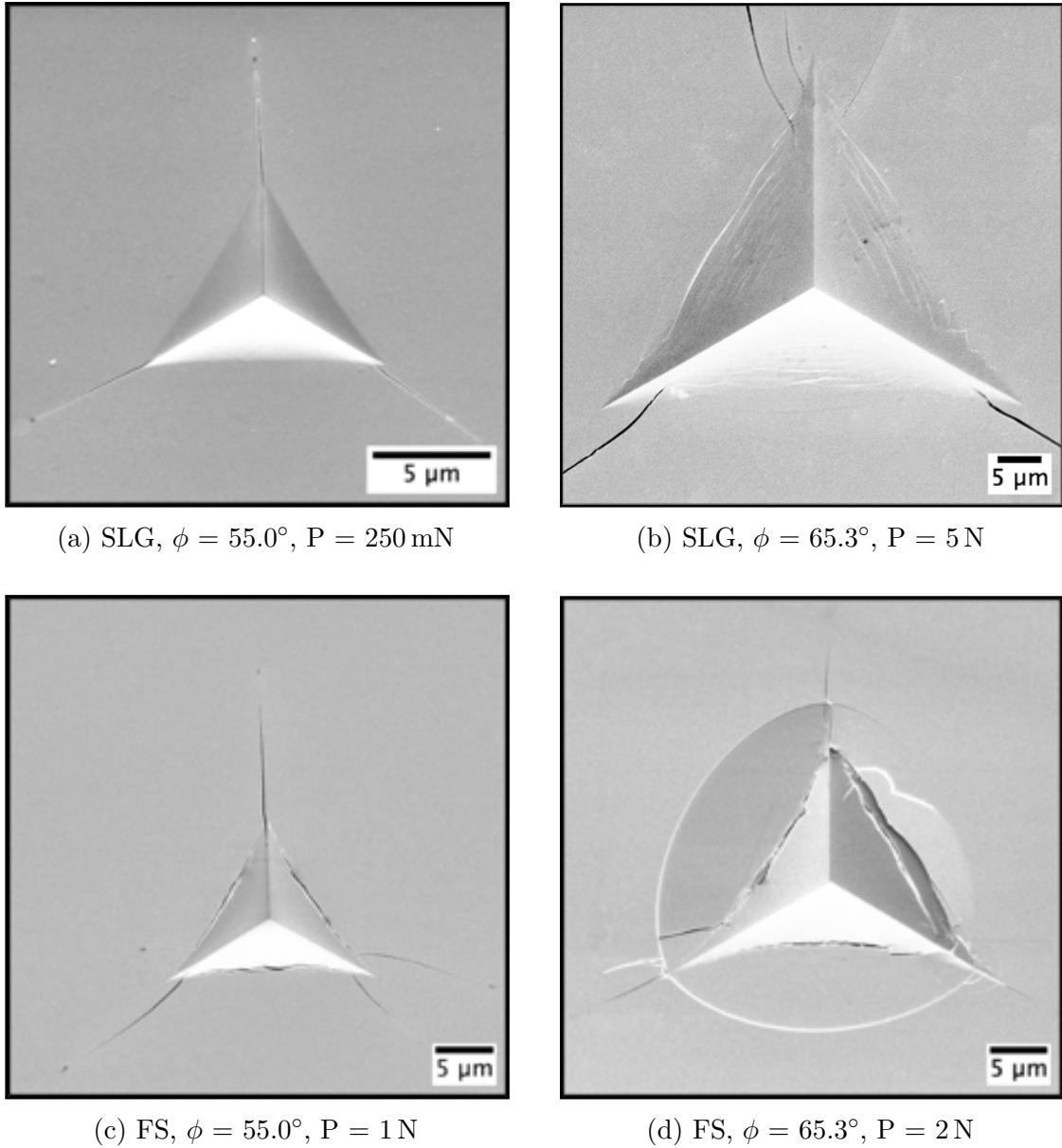
Figure 3.11: SEM images extracted from Figure 3.3 - 3.6 revealing differences in crack morphology between soda-lime glass (a and b) and fused silica (c and d).

at which the crack length c and indentation size a have the same length (Figure 1.5c), i.e., $c/a = 1$. The cracking threshold P_c determined in this way is represented by the light blue diamonds in Figure 3.10 for SLG. The magnitude predicted by the theory is lower than observed optically, suggesting that assuming $c/a = 1$ is not valid, and it should rather be about 1.4, even higher for the Berkovich indenter (see Figure 3.12).

Harding [24] likewise has determined, that c/a needs to be bigger than unity to be able to describe experimental values more accurately. He attributes this higher value to the fact that among other things the indentation corners are not perfectly sharp [24]. However, since the value is only slightly bigger than unity, it is valid to assume that the indentation itself can initiate the cracks and no preexisting flaws are needed [24].
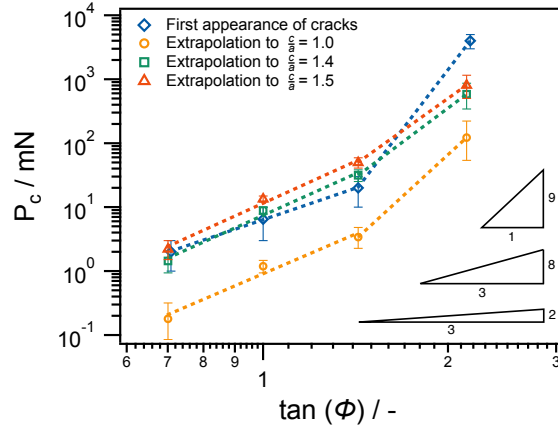
Figure 3.12: Cracking threshold P_c for radial cracks as a function of angle for soda-lime glass for different c/a ratios. The error bars for the theoretical values are based of the 95 % confidence interval. For the observed values the data points are the averages of the provided loading ranges in Table 3.1, with the error being the minimum and maxium values of the range.

Determining P_c by optically observing the first appearance of cracks for FS exhibits a significantly stronger dependency with ϕ, as the slope of the vermilion circles in Figure 3.10 is closer to 9. Mound and Pharr [21] have already reported this high deviation from theoretical relations. However, they did not explain its origin. Speculations on what could cause this discrepancy are three-fold. First, FS behaves anomalously as it densifies during indentation [31, 63, 64]. Densification reduces the crack driving residual stresses around the indentation, thus increasing P_c [8, 16, 31, 62, 65, 66]. Densification also reduces the number of shear faults on the subsurface. If shear faults can act as initiation sites for radial cracks, glasses with fewer shear faults should show higher crack

resistance [67]. Second, as shown in Table 3.1, edge cracks form in FS before radial cracks initiate. Potentially, edge cracks have already released the stresses that are built up, so the stresses need to build back up, requiring higher loads until a critical threshold is reached again. However, one could also argue that the edge cracks are pre-cursors to the radial cracks. If they form first, the radial cracking threshold would be reduced. Hence, whether edge cracks increase or decrease P_c remains inconclusive. Third, it could be possible that the underlying crack morphology in FS is not median-like, which could result in a different angular dependency. To verify the cracking morphology, subsurface analysis is required, as will be discussed in Section 3.5.
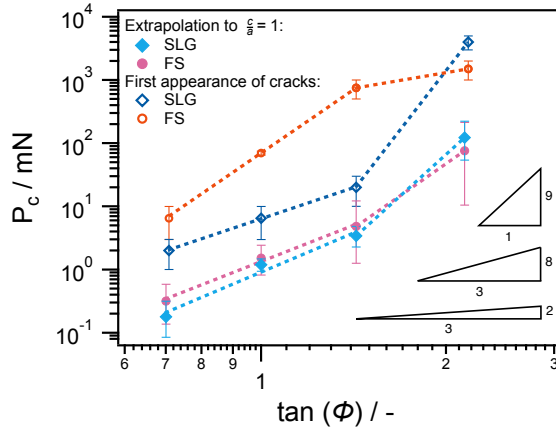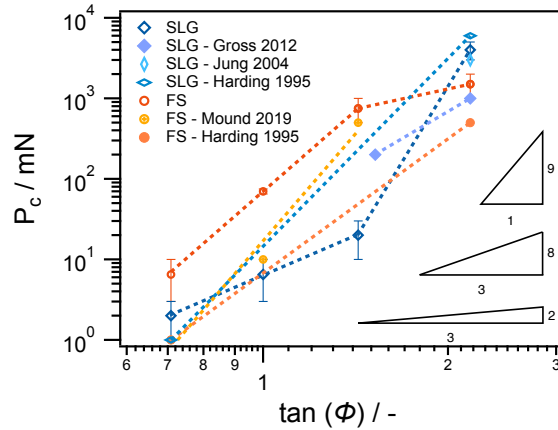

Figure 3.13: Cracking threshold P_c for radial cracks as a function of angle for soda-lime glass and fused silica in comparison with values reported in the literature [21, 24, 33, 68]. For the values observed in this work the data points are the averages of the provided loading ranges in Table 3.1, with the error being the minimum and maxium values of the range.

Figure 3.13 helps to put the P_c values from the present work into perspective with values reported in literature [21, 24, 33, 68]. Gross conducted experiments with two different four-sided pyramidal indenters, i.e., $\phi = 60.0°$ and $68.0°$ on SLG [33]. For the comparison in Figure 3.13, those two angles were converted to their three-sided equivalent using the assumption that the triangular pyramids need to yield similar

area-to-depth ratios as their four-sided counterparts [4]. His results do not agree well with the present work. One reason could be that although the angle was converted in terms of geometry, the cracking behavior is most likely different between three-sided and four-sided indenters. Using Harding's modification of the Ouchterlony approach to account for the difference in the number of corners and hence number of cracks around the indentation, the stress will be distributed amongst the number of cracks [24, 69]. Thus, the fracture toughness of a four-sided indenter should appear higher than the one for a three-sided indenter. Jang and Pharr developed a correlation between the cracking threshold and K_c, where P_c scales with K_c [34]. Therefore P_c should be lower for a three-sided indenter. Additionally, Vickers indentation shows a larger amount of densification than Berkovich indentation, which should likewise result in a higher P_c [63]. On the other hand, from this work it was determined that P_c and K_c do not necessarily scale with one another, as SLG exhibits a higher fracture toughness, but a lower P_c than FS.

Direct three-sided comparison can be done with work by Mound and Pharr [21], Harding [24], and Jung et al. [68]. Harding only performed tests with a cube corner and Berkovich tip [24], and Jung et al. only tested SLG with a Berkovich indenter. For SLG, Harding and Jung et al.'s results agree fairly well with values determined in the present work. However, the trend over the entire angular range has not been previously reported. The only work that considered the same angles is that of Mound and Pharr for FS [21]. For the 55.0°-indenter ($\approx \tan \phi = 1.4$), a similar value was observed, but for sharper angles Mound and Pharr observed smaller values for FS. Harding also reported P_c values for FS. However, once again just for the cube corner and Berkovich indenters. For both indenters, Harding reported P_c values that are about an order of magnitude lower than the ones determined in the present work. A potential reason for the difference could be the condition of tip, i.e., rounding of the tip and the edges, which is unknown for experiments conducted elsewhere in literature. Another reason

could be that imaging techniques have improved in the last 30 years, potentially making the measurements in the current work more accurate.

Using the Palmqvist theory and following similar ideas to Harding and Jang and Pharr [24, 34], the crack length l should be linearly proportional to the load P through

$$l = \left(\frac{\alpha_p \cdot \left(\frac{E}{H} \right)^{2/5}}{K_c} \right)^2 \cdot \frac{3\sqrt{3} \cdot H}{4} \cdot P \ . \tag{3.2}$$

This is in fact the case for both materials analyzed as shown in Figure 3.14. However, to determine the cracking threshold P_c in this way, one would have to determine the load at which $l = 0$. Since the relationship given in Equation (3.2) does not have a constant term, the load would always be zero using the aforementioned criterion. Therefore, this approach can not be used to determine a cracking threshold P_c.

(a) Soda-lime glass   (b) Fused silica
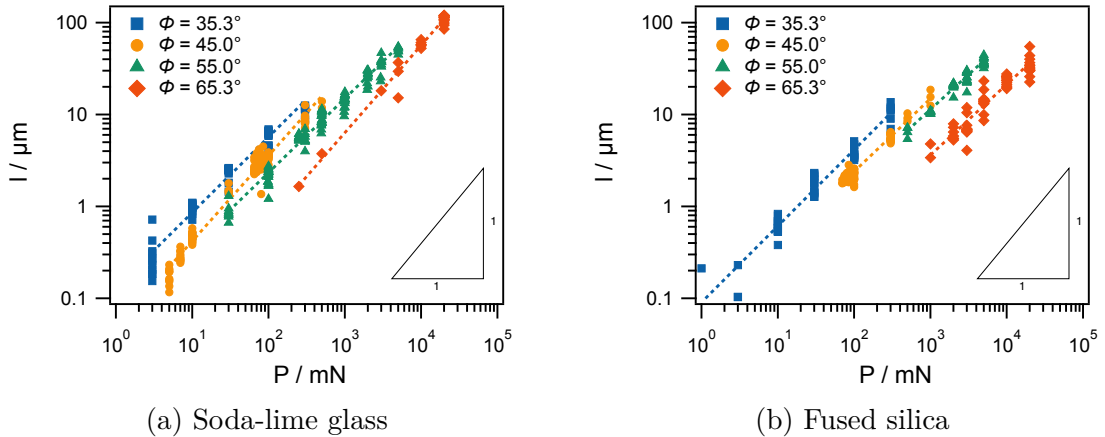
Figure 3.14: Crack length l as a function of load P for the studied materials.

Edge cracks as a rather new concept do not have an underlying theory yet to be compared to, and there also does not exist a significant angular dependency for the tested materials for the cases in which edge cracks are present (see Figure 3.3 - 3.6 and Table 3.1)pre. More important is the fact, that the edge cracks seem to play a significant role in the initiation of radial cracks.

3.4 Fracture Toughness

In addition to analyzing the crack initiation loads for soda-lime glass and fused silica, the crack propagation characteristics have also been investigated. In terms of fracture toughness measurements, typically two different crack morphologies are considered for the analysis. The different phyiscal mechanisms behind the crack systems result in different equations to use. Both approaches will be considered.

3.4.1 Median-Radial Cracks

Assuming the radial cracks around the indent are median-like, the relation developed by Jang and Pharr [34] to measure the fracture toughness is

$$K_c = \alpha_M \cdot \left(\frac{E}{H} \right)^{1/2} \cdot \frac{P}{c^{3/2}} \, , \tag{3.3}$$

where

$$\alpha_M = \frac{0.0352}{(1 - \nu)} \cdot (cot\,\phi)^{2/3} \tag{3.4}$$

The mechanical properties needed to compute K_c are summarized in Table 3.2. Values for Poisson's ratio ν are taken from literature, whereas modulus E and hardness H are determined from nanoindentation experiments with a Berkovich indenter using the Oliver-Pharr method [26].

Table 3.2: Mechanical properties for soda-lime glass (SLG) and fused silica (FS).

Material	ν / -	E / GPa	H / GPa
SLG	0.23	74.16	6.97
FS	0.188	70.02	9.22

To determine the prefactor α_M experimentally, Equation (3.3) can be rearranged to achieve a linear dependency between the normalized crack length and the load P

(Figure 3.15), with α_M being the proportionality constant. Due to having to display a loading range of multiple orders of magnitude, a logarithmic scaling was chosen. With the change to a logarithmic scale α_M can be determined from the y-intercept in Figure 3.15. For $\phi = 35.3\text{--}55.0°$ the linear dependency suggested by the theory describes the data well. In case of Berkovich indentations ($\phi = 65.3°$), a linear fit does not quite represent the data. The slope in case of SLG would need to be slightly bigger than unity, and in the case of FS slightly smaller than unity. This deviation comes from the fact that a perfect relation between the crack length c and the load P ($c \propto P^{2/3}$) is assumed to calculate the normalized crack length. As seen in Figure 3.7b and Figure 3.7d this assumption is not valid for the data conducted using a Berkovich indenter. In order to be able to use theoretical relations for comparison, the true linear fit will be maintained and α_M values will be reported as such (see insets in Figure 3.15a and Figure 3.15b).

(a) SLG   (b) FS
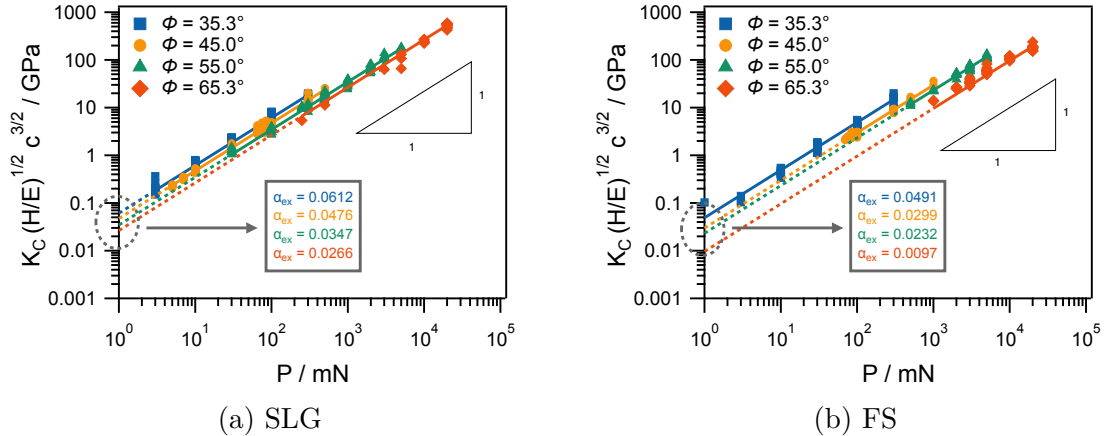
Figure 3.15: Normalized crack length following the median theory as function of load to determine experimental values for α_M. K_c was assumed to be $0.84\,\text{MPa} \cdot \text{m}^{1/2}$ and $0.69\,\text{MPa} \cdot \text{m}^{1/2}$ for SLG and FS, respectively [13, 24, 28, 31, 70–72].

The α_M-values determined in Figure 3.15 are summarized in Table 3.3. For both materials, SLG on the left and FS on the right of the table, one can observe that α_M decreases with increasing center-line to face angle ϕ. That behavior is reasonable,

since α_M is needed as a calibration constant in the fracture toughness equation (Equation (3.3)). From observations in Figure 3.7b and Figure 3.7d follows that a blunter indenter results in a shorter crack when compared at the same load. A smaller crack length c results in a higher value for $P/c^{2/3}$ and therefore a lower α_M is needed to result in the same fracture toughness for one material.

Table 3.3: Summary of α-values for median crack configuration. Theoretical values are computed using Equation (3.4).

$\phi \ / \ °$	SLG ($\nu = 0.23$)			FS ($\nu = 0.188$)		
	α_{ex}	α_{th}	% diff	α_{ex}	α_{th}	% diff
35.3	0.0612	0.0580	5.4	0.0491	0.0550	11.3
45.0	0.0476	0.0457	4.1	0.0299	0.0433	36.6
55.0	0.0347	0.0360	3.7	0.0232	0.0342	38.3
65.3	0.0266	0.0275	3.3	0.0097	0.0261	91.6

Comparing the values for the two materials shows that at each angle α_M is lower for FS than for SLG. Again, carefully looking at Equation (3.3) gives an explanation for that difference. Similar to the angular dependency described previously, FS exhibits a shorter crack. In addition, FS has a lower K_c than SLG [13, 24, 28, 31, 70–72]. Although FS exhibits a slightly smaller H/E value than SLG the significantly lower fracture toughness and crack length could explain that α_M is smaller for FS than for SLG. For comparison, Harding [24] determined 0.0371, 0.0183 and 0.0421, 0.0076 for cube-corner and Berkovich indentations in SLG and FS, respectively. That means, that for the Berkovich indenter the same trend is observed (SLG > FS), but for cube corner an opposite trend is reported.

Finally, Table 3.3 also includes α_M-values computed using Equation (3.4). Like the α_M-values determined experimentally, these values decrease with increasing angle and they are larger for SLG than for FS. However, a direct comparison of the magnitude yields a significant higher deviation between experiment and theory for FS (11–92 %)

than for SLG (3–6 %). In addition the % difference decreases slightly with angle for SLG and increases significantly with angle for FS. This might be a good indication, that the median crack theory can be used to describe the cracking behavior of SLG, but not so much the one of FS.

Similar to the cracking threshold in Section 3.3, the prefactor for the median crack theory α_M is dependent on the center-line to face angle ϕ. Theory predicts a proportionality of α_M with $\cot\phi$ (see Equation (3.4)). Hence α_M is plotted as a function of $\cot\phi$ in Figure 3.16 to determine if the angular dependency can be described by theoretical approaches.
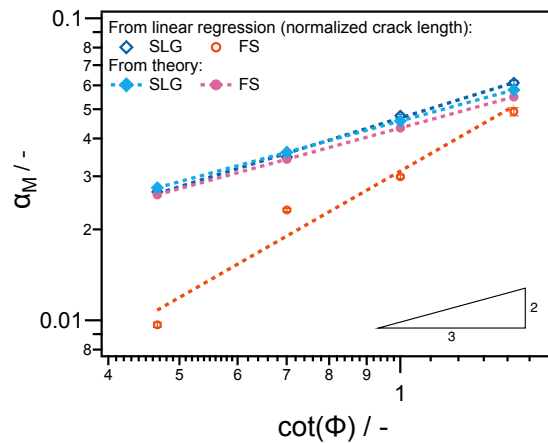
Figure 3.16: Comparison of α-values for median crack configuration. Theoretical values are computed using Equation (1.6).

SLG (blue diamonds) is well described by the theory, both regarding the angular dependency as well as the magnitude of α_M. The difference between experiment (dark blue diamonds) and theory (light blue diamonds) for SLG is relatively low and on average at around 5 %. In FS (red circles) the error increases significantly with increasing angle, resulting in a significantly higher slope than the predicted 2/3. This might be an indication that SLG behaves median-like and FS does not.

Figure 3.17 compares the toughness measured for each angle at which cracks could

be introduced in the material. The gray range represents the range of K_c determined with conventional methods for the two materials [13, 24, 28, 31, 70–72].

(a) Soda-lime glass   (b) Fused silica
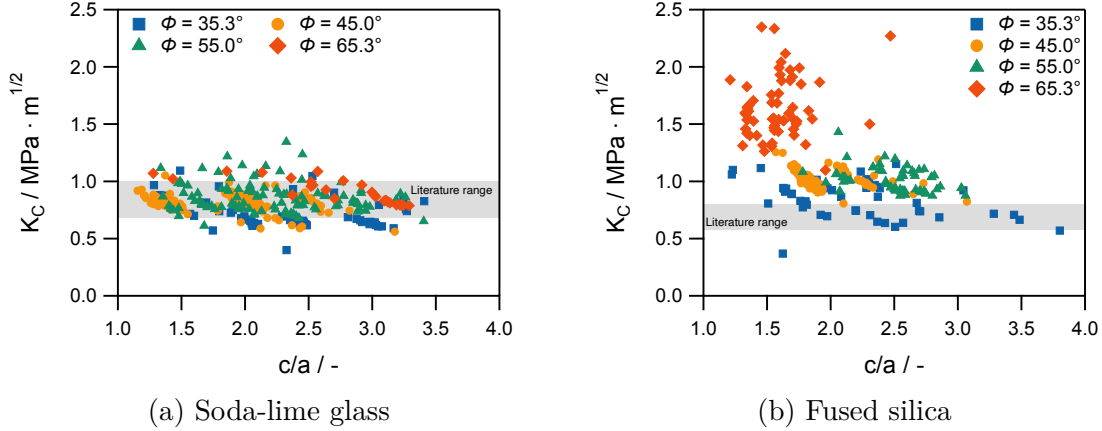
Figure 3.17: Fracture toughness K_c calculated using Equation (3.3). The gray area represents the range of literature values for K_c measured with traditional techniques.

When comparing the results determined here with values found in literature, it should be noted that Equation (3.3) can generally be used to calculate the fracture toughness of SLG, even at $c/a < 2.5$. When the relation is used for FS, however, the calculated fracture toughness is not constant over the c/a-range but rather increases as c/a decreases. Since this behavior is similar to the behavior for tungsten carbide in Figure 1.14a when a median-radial crack assumption is used, it could be suggested that the material shows Palmqvist-like behavior in those scenarios. Once again, subsurface analysis is of significant importance here to confirm or deny this suspicion. Although the fracture toughness is not constant over the c/a-range for FS, the theoretical value for α_M accounts appropriately for the angular dependency and K_c is similar irrespective of angle, with the exception of the Berkovich data red diamonds. In that case the fracture toughness is overestimated by theoretical relations.

In recent years Jang and Pharr's approach to determine the value for α_M has been

criticized by Hyun et al. [73]. They claim that the logarithmic approach is not valid, since a c/a dependency is not considered properly in the analysis by Jang and Pharr. Hence, to achieve accurate α_M-values, they argue it is necessary to use data in the linear plot [73]. This actually is the same approach that Anstis et al. used in the early 1980s to determine an α-value for the four-sided Vickers indenter for a variety of materials [36]. Based on Hyun et al.'s criticism, the linear approach is considered in Figure 3.18 and compared to the logarithmic approach in Table 3.4.

(a) Soda-lime glass

(b) Fused silica
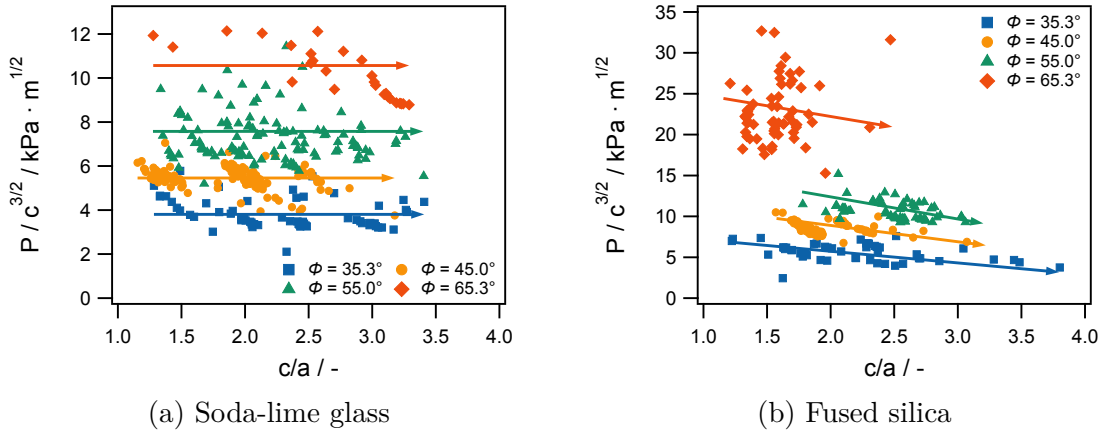
Figure 3.18: Indentation fracture parameter $P/c^{3/2}$ vs c/a for the median crack morphology. Arrows are guides for the eye closely following true fits through the data.

Figure 3.18 shows the indentation load normalized by the crack length for both materials, SLG in Figure 3.18a and FS in Figure 3.18b, for the different indenter angles. For both materials, $P/c^{3/2}$ increases with increasing center-line to face angle ϕ. The FS data is slightly higher than for SLG for $35.3° \leq \phi \leq 55.0°$. For the Berkovich indenter, the FS data lies well above the SLG data by a factor of about 2 higher at approximately $23\,\text{kPa}\,\text{m}^{1/2}$. Angular and material differences are expected, as the crack lengths depend on those parameters (see Figure 3.7).

As a first approximation, $P/c^{3/2}$ is assumed to be invariant with respect to c/a.

This assumption is more valid for SLG than for FS, since as shown by the arrows in Figure 3.18b, $P/c^{3/2}$ decreases with increasing c/a. If assuming a perfect invariance, the mean through the data for each angle can be computed. These average values can be used in Equation (3.3) to calculate the α_M-values. They are summarized in Table 3.4, which shows that the two appropaches yield similar results.

Table 3.4: Comparison of experimentally determined α-values for the median crack configuration using a log-log approach according to [34] and a linear approach according to [73].

ϕ / °	SLG			FS		
	$\alpha_{ex,log-log}$	$\alpha_{ex,lin}$	% diff	$\alpha_{ex,log-log}$	$\alpha_{ex,lin}$	% diff
35.3	0.0612	0.0676	9.9	0.0491	0.0448	9.2
45.0	0.0476	0.0472	0.8	0.0299	0.0294	1.7
55.0	0.0347	0.0354	2.0	0.0232	0.0235	1.3
65.3	0.0266	0.0244	8.6	0.0097	0.0109	1.2

3.4.2 Palmqvist Cracks

Niihara [74] has performed a corresponding analysis to the LEM theory [27] based on fracture mechanics principles for Palmqvist cracks. However, the derivation assumes four-sided indenters, so it would be necessary to establish relations for three-sided indenters. The derivation for three-sided indenters to determine a respective prefactor for the Palmqvist crack theory α_P will be discussed in detail below.

Palmqvist Crack Derivation

To determine the fracture toughness of a material using a four-sided Vickers tip, Niihara [42, 74] suggested a relation based on the Palmqvist crack configuration:

$$K_c = \alpha_P \left(\frac{E}{H} \right)^{2/5} \cdot \frac{P}{a\sqrt{l}}, \tag{3.5}$$

58

where α_P is a calibration constant for the Palmqvist crack theory, E and H are the material's modulus and hardness, respectively, while P, a, and l describe the load, indentation size, and crack length, respectively. For indentation with a Vickers indenter, experimental and theoretical analysis lead to an α_P-value of 0.009 [42, 74]. The following derivation should allow one to determine a similar relationship for triagonal pyramidal indenters using similar fracture mechanics principles.

Similar to Niihara [74], it will be considered that the Palmqvist crack system can be represented by a semi-elliptical surface geometry as shown in Figure 3.19. The stress intensity factor K for this system is

$$K = k_0\sqrt{2\pi}\sigma \cdot \left(\frac{m^2}{l}\right)^{1/2}, \tag{3.6}$$

where l and m are defined in Figure 3.19, k_0 is the free-surface correction factor typically approximated with $k_0 = 1.12$ [75], and σ is the stress around the indentation. However, when carefully deriving the equation for the stress intensity factor from Broek [75], the factor $\sqrt{2}$ in this work is in the numerator, whereas in Niihara's work it was in the denominator.
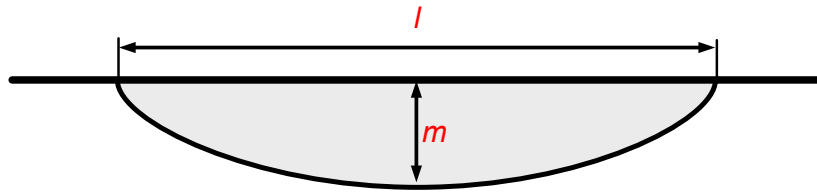
Figure 3.19: Semi-elliptical representation of the Palmqvist crack (modified from [74]).

To describe the stress around the indentation, Niihara utilizes a relation for the maximum residual stress developed by Perrott [76], that is a major contributor of crack

propagation and has the form

$$\sigma_r \approx \frac{H}{\sqrt{3}\tau_c} ln\left(\frac{E\tau_c \tan\phi_{eff,ex}}{H}\right),$$ (3.7)

where τ_c represents the Tabor constraint factor and $\phi_{eff,ex}$ the excluded effective cone angle (see Figure 3.20a) for the pyramidal indenter geometry depicted in Figure 3.20b [76]. Modulus and hardness are described by E and H, respectively.

(a) Effective Cone Indenter   (b) Trigonal Pyramidal Indenter
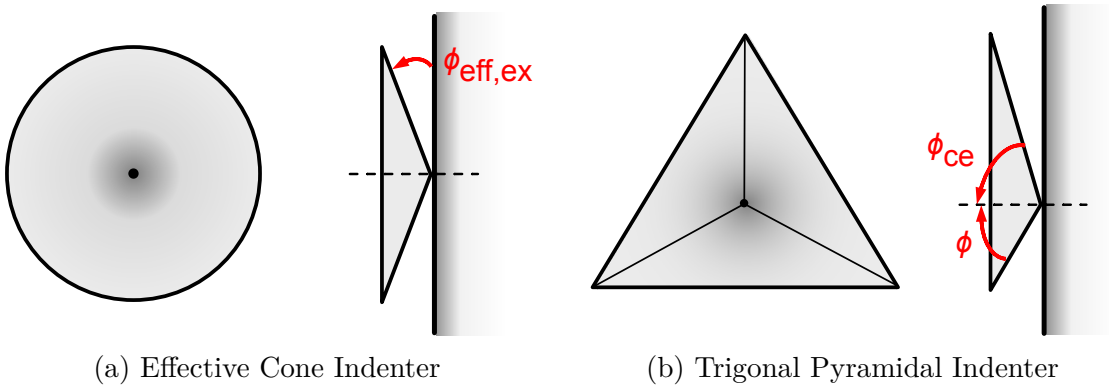
Figure 3.20: Definition of the various angles used in the derivation. Like it has been done by Niihara [74], the external angle ($\phi_{eff,ex}$) was used for the effective cone and the internal angle (ϕ_{ce}) was used for the pyramid. At the end of the analysis in this work, all angles will be converted to the commonly used center-line to face angle ϕ.

Niihara [74] states that Figure 3.21 allows to approximate

$$ln\left(\frac{E\tau_c \tan\phi_{eff,ex}}{H}\right) \approx 0.63\left(\frac{E\tau_c \tan\phi_{eff,ex}}{H}\right)^{2/5}.$$ (3.8)

However, careful investigation of Figure 3.21 shows that Equation (3.8) is flawed and rather needs to be approximated using a prefactor of 0.9 (Figure 3.22). Furthermore, it needs to be considered, that for the materials investigated in this work, namely fused silica and soda-lime glass, τ_c should be on the order of 1.3–1.6 instead of 3 [77–79]. Keeping that in mind and following the idea in Figure 3.21 for an angular dependency
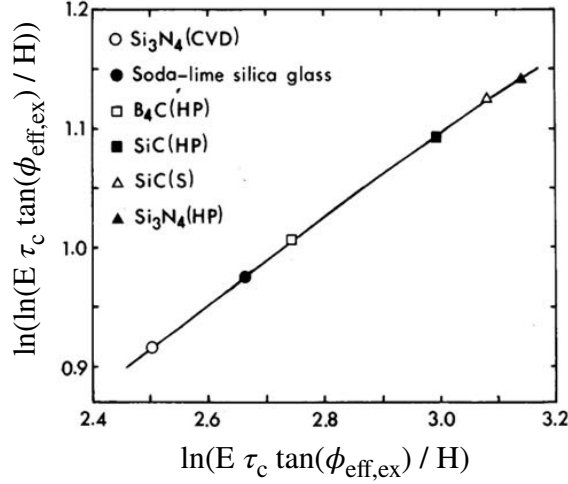
Figure 3.21: Relationship used to simplify the logarithmic term in Equation (3.7) according to Niihara (reprinted with permission from [74]).
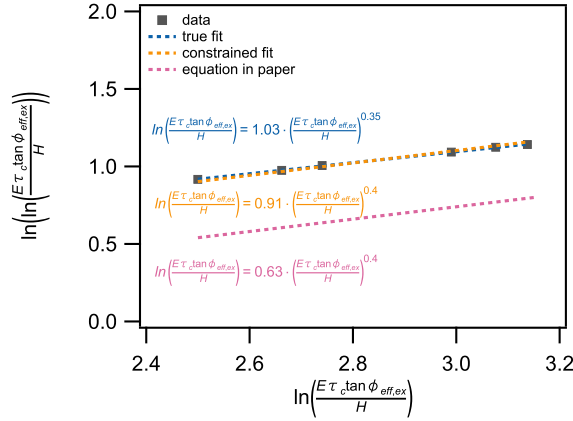
Figure 3.22: Digitized version of Figure 3.21.

(Figure 3.23), rather than a material dependency, Equation (3.8) would need to be rewritten to

$$ln\left(\frac{E\tau_c \tan\phi_{eff,ex}}{H(1-\nu^2)}\right) \approx 0.7\left(\frac{E\tau_c \tan\phi_{eff,ex}}{H(1-\nu^2)}\right)^{1/2}, \tag{3.9}$$

where τ_c is assumed to be 1.6. Although only slightly contributing to the relation, the dependency through Poisson's ratio ν is included for completeness, while it was neglected by Niihara [74].

(a) $\tau_c = 1.6$ (b) $\tau_c = 3$
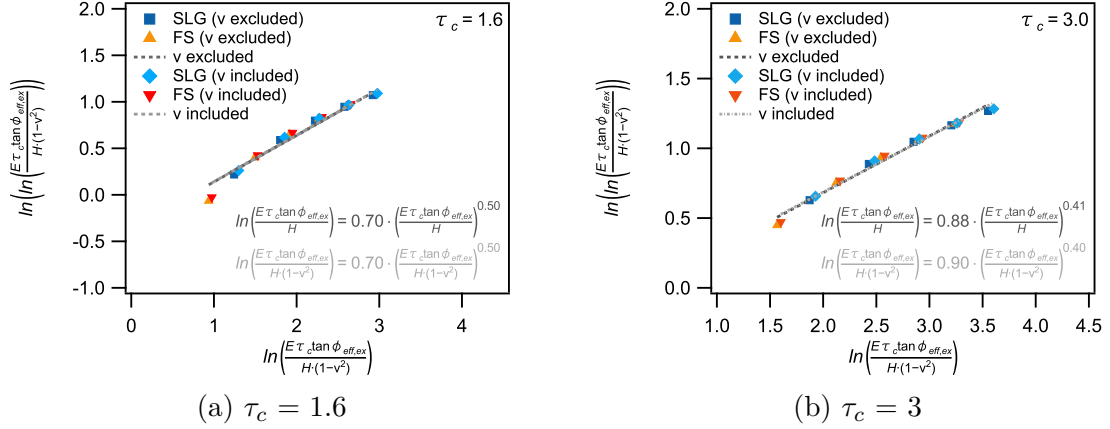
Figure 3.23: Influence of τ_c and ν when simplifying the logarithmic term in Equation (3.7).

Finite Element Analysis (FEA) has shown that it is not valid to use just one Tabor constraint factor τ_c when considering the angular dependency while simplifying Equation (3.7) [80, 81]. Using FEA for conical indenters, Shim et al. determined τ_c for the different angles used in this work, namely $\phi = 35.3°$, $45.0°$, $55.0°$, and $65.3°$ for single-crystalline silicon carbide [81]. For ceramic materials (low E/σ_y), τ_c can also depend significantly on E/σ_y [80, 82]. Based on Shim et al.'s analysis, silicon carbide typically has a E/σ_y of 30. Likewise using FEA, Bolshakov and Pharr calculated $E/\sigma_y = 28.1$ for SLG [82]. Since the values for SLG and silicon carbide are very similar, it will be assumed here that the Tabor constraint factors determined by Shim et al. can also be used for SLG. In a first approximation, it will be assumed that the same values can also be used for FS.

Shim et al. [81] also include friction influences in their analysis. However, in the remainder of the analysis friction is not considered, also because hardness is constant as a function of indenter angle for the materials tested (Figure 3.7a and Figure 3.7c) and an angle invariant hardness in silicon carbide is only achieved when the coefficient of friction is $\mu = 0.0$.

62
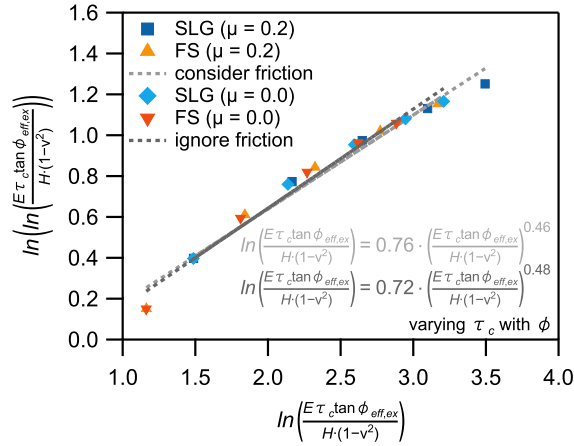
Figure 3.24: Influence of frictional effects while determining a simplification for Equation (3.7).

Shim et al. [81] do provide a Tabor constraint factor for an indenter with a center-line to face angle $\phi = 75.0°$, and at first it was included in the analysis and derivation (Figure 3.25). However, no radial cracks could be introduced using this indenter geometry in the tested loading range. Because of that and since the inclusion of the 75.0° indenter changes the necessary relations quite a bit, it will be excluded in the further analysis.
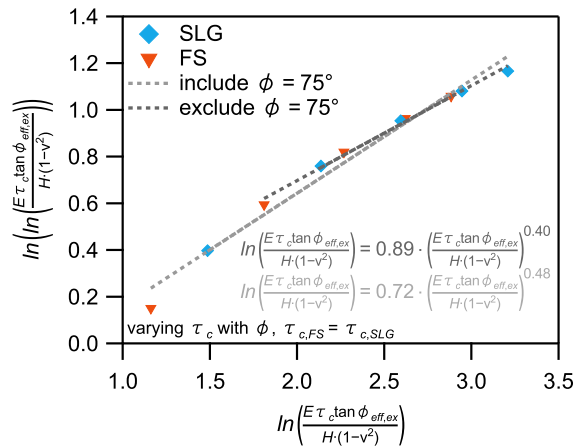
Figure 3.25: Influence of the bluntest indenter angle ($\phi = 75.0°$) on the simplification of Equation (3.7).

The Tabor constraint factors for fused silica (FS) can not be assumed to be the same values as the ones for SLG or silicon carbide respectively given FS has a significant different value for E/σ_y. Different groups have determined a yield stress of about 5.5 GPa [83–85]. Using $E = 70$ GPa (table 3.2) yields $E/\sigma_y = 12.7$, which is less than half the values of those for soda-lime glass or silicon carbide. For FEA with a conical indenter and included effective cone angle $(\phi_{eff}) = 68.0°$, Cheng and Cheng show the material dependency of the Tabor constraint factor [80]. For their case, τ_c is 2.28 and 1.87 for SLG and FS, respectively. Assuming that the difference between these values does not change as a function of angle, the values for FS in this work will be assumed to be 82 % of the values provided by Shim et al. [81].
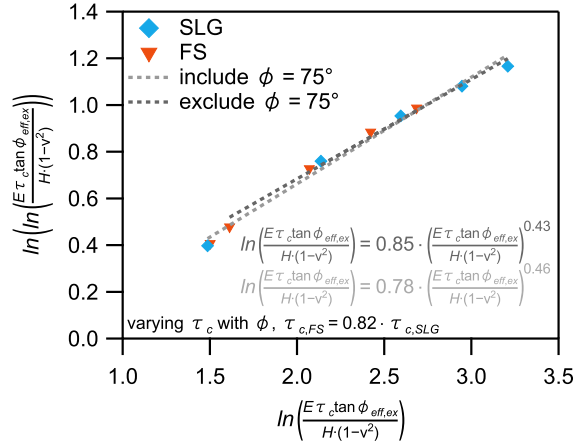
Figure 3.26: Adjustment of the Tabor constraint factor for FS and its effects on the simplification of Equation (3.7).

Including the adjustments in Figure 3.26, namely accounting for the material and angular dependency of the Tabor constraint factor τ_c and excluding the bluntest indenter angle, Equation (3.8) finally becomes

$$ln\left(\frac{E\tau_c \tan\phi_{eff,ex}}{H(1-\nu^2)}\right) \approx 0.9\left(\frac{E\tau_c \tan\phi_{eff,ex}}{H(1-\nu^2)}\right)^{2/5},\tag{3.10}$$

where τ_c itself is dependent on the indenter angle. Note that the prefactor of 0.9 was also achieved when refitting the data provided by Niihara [74] (Figure 3.22), showing that material and angular dependency give rise to similar relationships.

Since the Palmqvist crack was observed to be approximately as deep as the indentation d_{ind} itself [86], the crack depth m can be directly related to the indentation size a through

$$m \approx \frac{k_1 a}{\tan \phi_{ce}}, \tag{3.11}$$

where k_1 is a geometry constant and ϕ_{ce} is the center-line to edge angle of the pyramidal indenter (Figure 3.20b). Experimental observations of Vickers (Figure 3.27) and Berkovich (Figure 3.28) indentation in FS support the experimental observations by Ogilvy et al. [86]. The average value for the depth of the three Palmqvist cracks around a Berkovich indentation is $m_{avg} = 3.39\,\mu\text{m} = 1.63\cdot d_{ind}$ and the average value for the depth of the four different Palmqvist cracks around a Vickers indent is $m_{avg} = 2.72\,\mu\text{m} = 1.67\cdot d_{ind}$, which makes $k_1 = 1$ a reasonable assumption moving forward.

If Equation (3.7) (Equation (3.10) for approximation of ln-term) and Equation (3.11) are used for σ and m, the stress intensity factor becomes

$$K = \frac{0.9 k_0 k_1 \sqrt{2\pi}}{\tau_c^{3/5}(1-\nu^2)^{2/5}} \cdot \frac{\tan \phi_{eff,ex}^{1/2}}{\tan \phi_{ce}} \cdot \left(\frac{E}{H}\right)^{2/5} \cdot \frac{aH}{\sqrt{l}} \tag{3.12}$$

Using the hardness equation for the three-sided pyramidal geometry (Equation (3.1)) and converting the given angles to the commonly used center-line to face angle ϕ as defined in Figure 3.20b yields

$$K = \frac{0.453 k_0 k_1}{\tau_c^{3/5}(1-\nu^2)^{2/5}} \cot \phi^{7/5} \cdot \left(\frac{E}{H}\right)^{2/5} \cdot \frac{P}{a\sqrt{l}} \tag{3.13}$$

Using Ouchterlony [69] to account for the fact that n radial cracks open up around the indentation modifies the stress intensity factor to

65
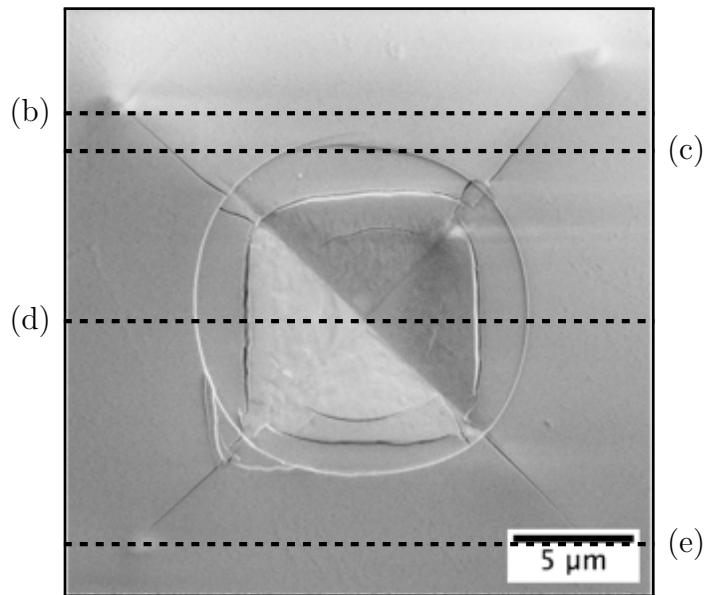
(a) Surface view.
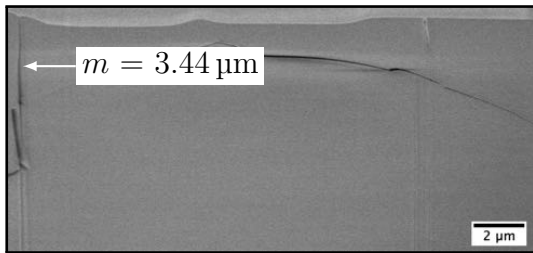
(b) Cross-section of top-left crack.
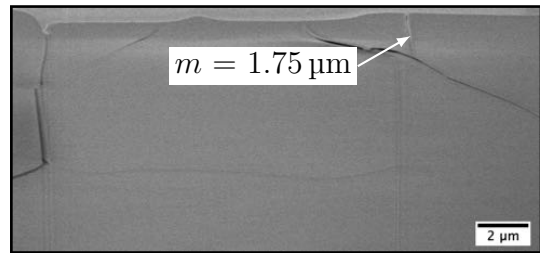
(c) Cross-section of top-right crack.
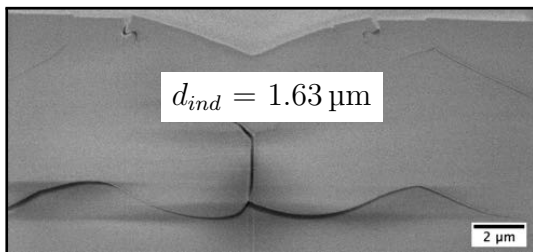
(d) Cross-section of indent at apex.
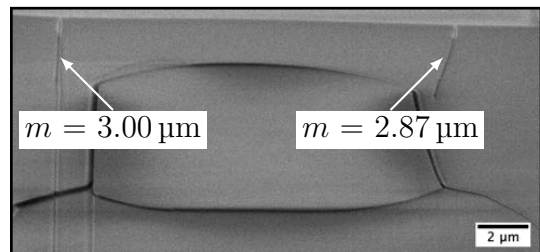
(e) Cross-section of bottom cracks.

Figure 3.27: Measuring indent and Palmqvist crack depths for a 1 N Vickers indent in fused silica. The depicted cross-sections are at maximum depth for the respective dimensions.

(a) Surface view.

$m = 2.64\,\mu\text{m}$
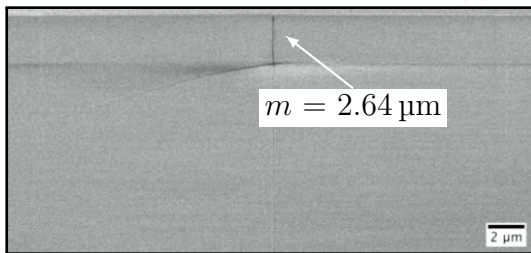
(b) Cross-section of top crack.

$d_{ind} = 2.08\,\mu\text{m}$
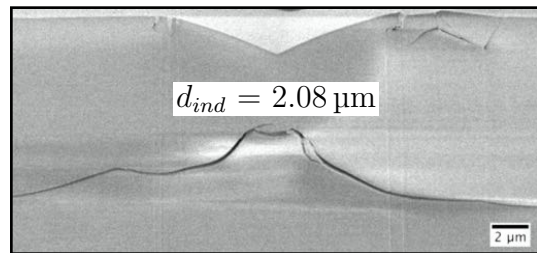
(c) Cross-section of indent at apex.

$m = 4.31\,\mu\text{m}$
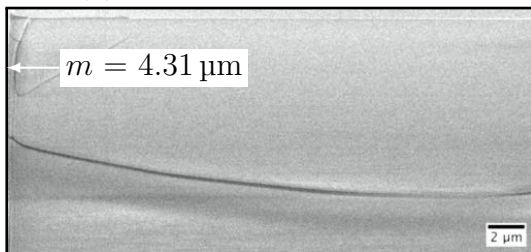
(d) Cross-section of bottom-left cracks.

$m = 3.22\,\mu\text{m}$
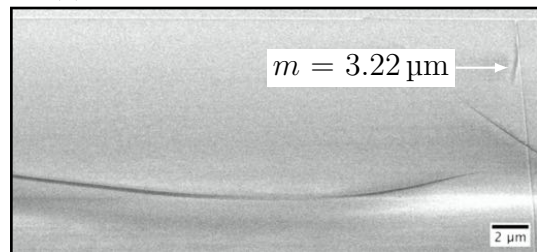
(e) Cross-section of bottom-right crack.

Figure 3.28: Measuring indent and Palmqvist crack depths for a 2 N Berkovich indent in fused silica. The depicted cross-sections are at maximum depth for the respective dimensions.

$$K = \frac{1}{n} \sqrt{\frac{\frac{n}{2}}{1 + \frac{n}{2\pi} \sin \frac{2\pi}{n}}} \cdot \frac{0.453 k_0 k_1}{\tau_c^{3/5} (1 - \nu^2)^{2/5}} \cot \phi^{7/5} \cdot \left(\frac{E}{H}\right)^{2/5} \cdot \frac{P}{a\sqrt{l}} \tag{3.14}$$

Note the additional $1/n$ factor to divide the point expansion pressure into n forces acting radially between each crack as introduced by Harding [24]. With each additional crack the stress intensity needs to decrease, and that only occurs if the extra term is included. Around a threes-sided indentation $n = 3$, so

$$K = \frac{0.156 k_0 k_1}{\tau_c^{3/5} (1 - \nu^2)^{2/5}} \cot \phi^{7/5} \cdot \left(\frac{E}{H}\right)^{2/5} \cdot \frac{P}{a\sqrt{l}} \tag{3.15}$$

Assuming $k_0 = 1.12$ and $k_1 = 1$ yields

$$K = \frac{0.175}{\tau_c^{3/5} (1 - \nu^2)^{2/5}} \cot \phi^{7/5} \cdot \left(\frac{E}{H}\right)^{2/5} \cdot \frac{P}{a\sqrt{l}} \tag{3.16}$$

Finally, comparing Equation (3.16) to Equation (3.5) yields

$$\alpha_P = \frac{0.175}{\tau_c^{3/5} (1 - \nu^2)^{2/5}} \cot \phi^{7/5} \tag{3.17}$$

Equation (3.17) indicates that there exists an angular dependency through the centerline to face angle ϕ as well as a material dependency through the Poisson's ratio ν. An additional geometry and material dependency comes in through the Tabor constraint factor τ_c.

Palmqvist Crack Analysis

When rearranging the general equation for the Palmqvist crack configuration (Equation (3.5)), theory suggests a linear increase of the normalized crack length with increasing indentation load. This is indicated by a slope of one in Figure 3.29.

The data was fitted with a linear regression and it shows that the linear dependency works well for $\phi = 35.3$–$55.0°$, but the slope deviates slightly from unity for the Berkovich indenter ($\phi = 65.3°$). Similar to the median crack approach, this discrepancy
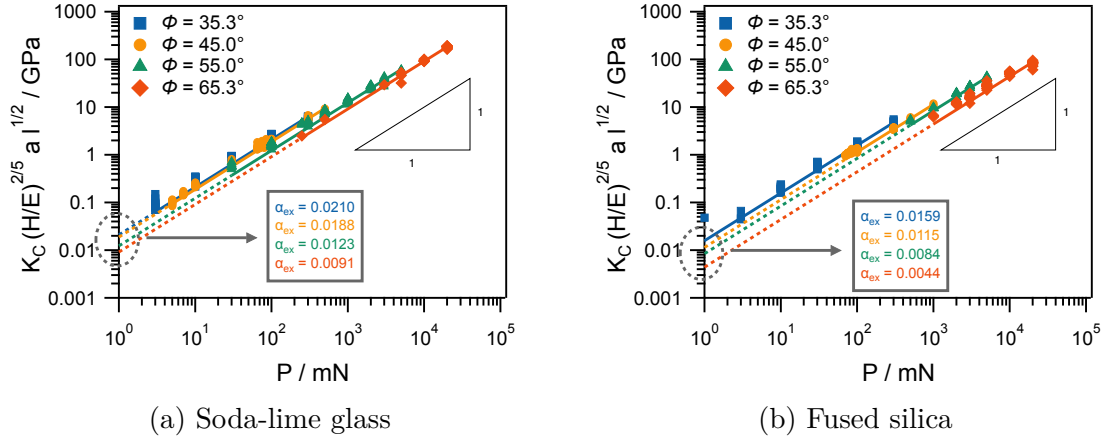
Figure 3.29: Normalized crack length following the Palmqvist Theory as function of load to determine experimental values for α_P.

can be explained by the fact that in calculating the normalized crack length a perfect relation between crack length and load is used. However, Figure 3.14 shows that this relationship is not quite fulfilled for the Berkovich indenter. Again, the linear fit will be used nonetheless to determine the values of the α_P and they are summarized in Table 3.5. Similar to the α_M-values in Table 3.3, the α_P-values with increasing center-line to face angle ϕ and the values for SLG are higher than the ones for FS.

Table 3.5: Summary of α-values for Palmqvist crack configuration. Theoretical values are computed using Equation (3.17).

ϕ /°	SLG ($\nu = 0.23$)			FS ($\nu = 0.188$)		
	α_{ex}	α_{th}	% diff	α_{ex}	α_{th}	% diff
35.3	0.0210	0.1880	160	0.0159	0.2158	173
45	0.0188	0.1116	142	0.0115	0.1248	166
55	0.0123	0.0675	138	0.0084	0.0755	160
65.3	0.0091	0.0391	124	0.0044	0.0437	163

In comparison to the α_M values determined in Section 3.4.1, however, a significant difference of more than $100\,\%$ between the experimentally determined and computed

values is noticeable. There are several possible explanations for the difference in magnitude. One is that Ouchterlony's star-shape crack relations could be used to account for multiple cracks around the indentation [69]. However, a translation from one to three cracks is necessary in the derivation and Ouchterlony is only valid for two and more cracks. Therefore, using Ouchterlony as done in section 3.4.2 might not be valid. Second, the assumption for the crack depth in relation to the indentation depth has been adapted from Niihara's derivation [74] and was only validated with two subsurface investigations of a Vickers and a Berkovich indentation, since those indents show Median and Palmqvist cracks that are clearly distinguishable. Lastly, Niihara [74] uses the far-field maximum residual stress around the indentation to describe the stress necessary for the Palmqvist crack to grow. The true stress field around the indentation is much more complex, but might scale with the stress used for the derivation.

The analysis in section 3.4.2 suggests that α_P is likewise assumed to increase with $\cot\phi$ (Equation (3.17)). In the case of the Palmqvist crack morphology, however, the exponent in the given relation should be 7/5 compared to the 2/3 for the median crack morphology. In the double-logarithmic plot (Figure 3.30), this exponent can be represented by the slope. For both materials tested α_P increases with decreasing angle. The angular dependency of FS can be described by theoretical relations, as the slope of the red circles is very close to the predicted value of 7/5. The slope for SLG on the other hand is slightly lower than assumed by the Palmqvist theory. This once again might allow the conclusion that FS can be better described using the Palmqvist theory.

Although the angular dependency of α_P can be described properly with theoretical relations, the magnitude of α_P is overestimated by about a factor of 10. Potential reasons for this discrepancy have been discussed above.

Using the theoretical values for α_P, the fracture toughness is calculated and depicted as a function of c/a in Figure 3.31. Since it has already been discussed that α_P is overestimated, K_c is overestimated, as well. However, it was possible to account for the

70
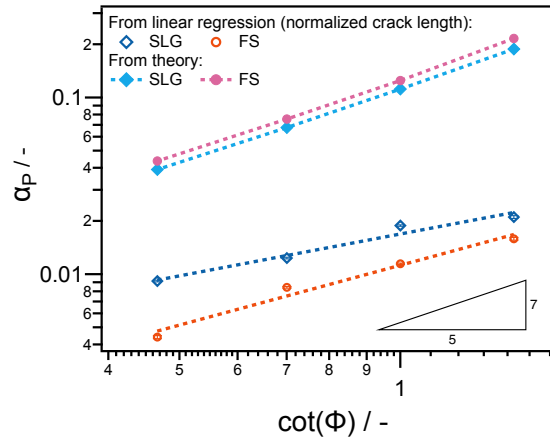
Figure 3.30: Comparison of α-values for Palmqvist crack configuration. Theoretical values are computed using Equation (3.17).

(a) Soda-lime glass

(b) Fused silica
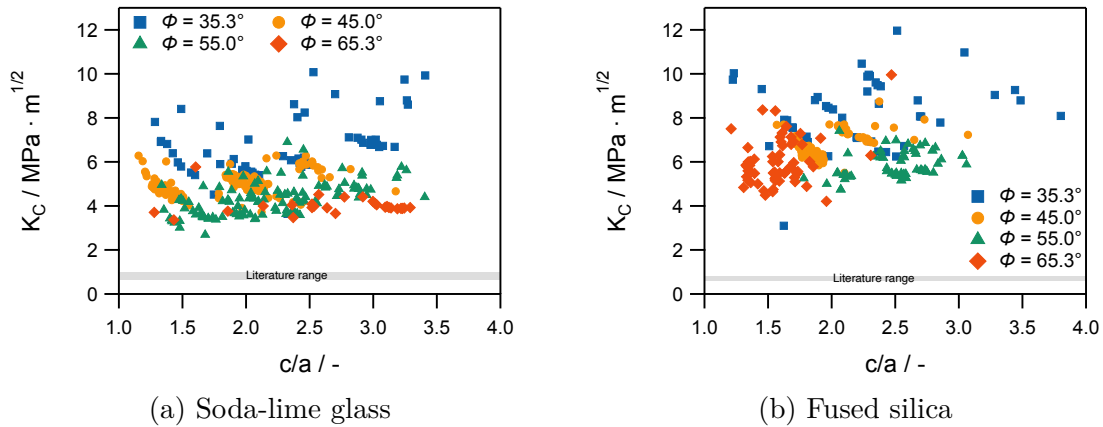
Figure 3.31: Fracture Toughness using theoretical values for α_P according to Equation (3.17).

angular dependency in FS, so that K_c can be calculated to a similar value irrespective of the angle used for indentation. Furthermore, it should be noted that now the fracture toughness is constant over the tested c/a- range for FS. K_c for SLG increases slightly with increasing c/a. This could indicate once again that SLG shows median crack features, whereas FS can be described using the Palmqvist approach.

When using the experimental values for α_P as determined in Figure 3.29, the fracture toughness for the two materials is shown in Figure 3.32. In this case the calculated

71

K_c using nanoindentation agrees fairly well with values reported in literature and it is independent of c/a and ϕ for FS. Since Figure 3.32 is technically a circular analysis to the one performed using fitting in Figure 3.29, it is expected that K_c agrees with literature values. However, if the assumption of a Palmqvist crack morphology can be made, the α_P-values that were determined during the fitting in Figure 3.29 should yield K_c-values that are constant over the tested c/a range. This is true for FS in Figure 3.32b. For SLG in Figure 3.32a however, although the majority of the data points are close to the literature range, there is an overall increasing trend of K_c with increasing c/a, which is slightly more prominent than in Figure 3.31a. This behavior is similar than the one for another material that should crack median-like (Si_3N_4 in Figure 1.14b when analyzed using the Palmqvist approach. Hence SLG is assumed to crack median-like and FS Palmqvist-like.
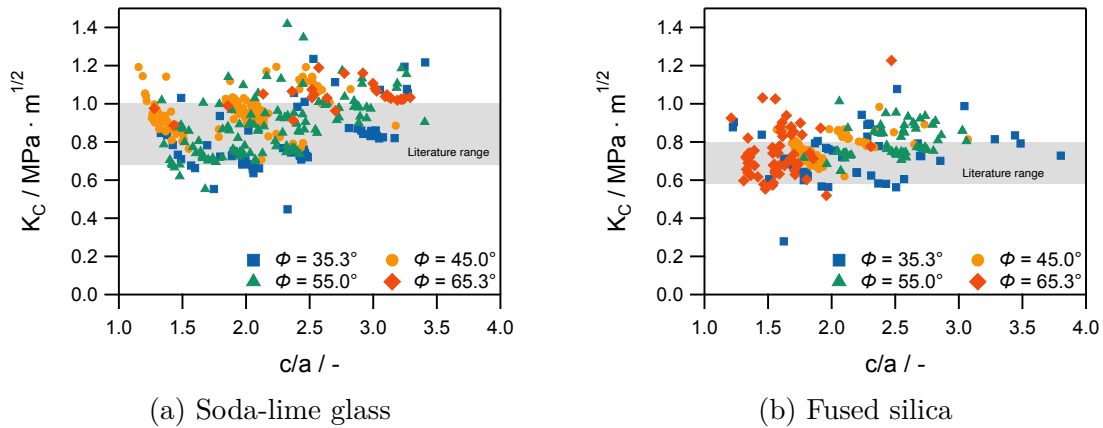
Figure 3.32: Fracture Toughness using experimental values for α_P.

Due to the criticism of the Jang and Pharr analysis to determine an α value as expressed by [73] and as discussed above, a linear analysis to determine the α_P value was performed for completeness. For the Palmqvist morphology, the indentation fracture parameter to consider as a function of c/a becomes $P/a \cdot l^{1/2}$, as shown in Figure 3.33.

Similar to the median crack analysis, this parameter increases with increasing ϕ and is slightly higher for FS than for SLG for $\phi = 35.3$–$55.0°$ and significantly higher for $\phi = 65.3°$. However, a notable difference is that the indentation fracture parameter now increases with increasing c/a for SLG in Figure 3.33a, but remains rather flat for FS in Figure 3.33b, providing another indication for change in crack morphology from median to Palmqvist for FS compared to SLG.

(a) Soda-lime glass   (b) Fused silica
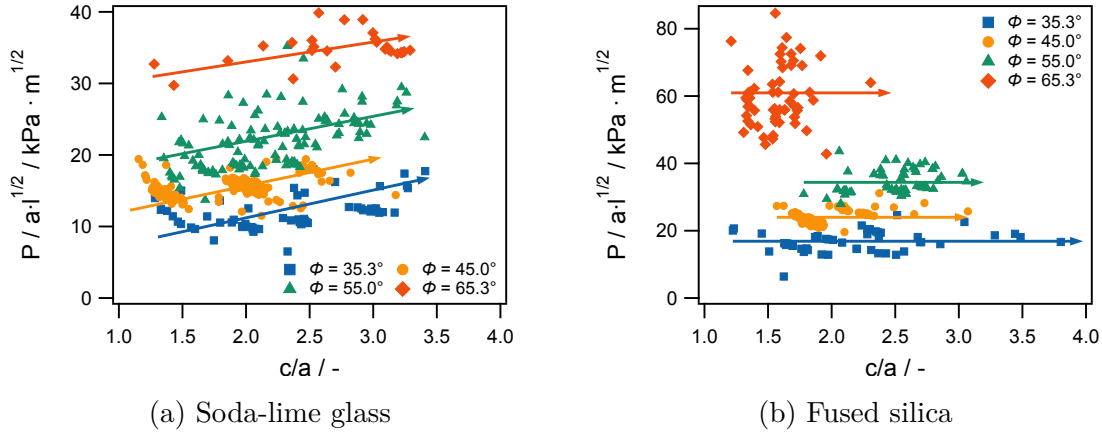
Figure 3.33: Indentation fracture parameter $P/a \cdot l^{1/2}$ vs c/a for the Palmqvist crack morphology. Arrows are guides for the eye closely following true fits through the data.

If assuming, nonetheless, that the indentation fracture parameter is constant over the tested c/a range, determining the averages of $P/a \cdot l^{1/2}$ for each indenter angle in Figure 3.33, and utilizing Equation (3.5), yields α_P values for the linear approach that are summarized in Table 3.6.

Comparing the logarithmic approach with the linear approach shows again that the values are fairly similar; however the % difference between the approaches is on average a factor 3 higher for the Palmqvist approach than for the median approach in Section 3.4.1. Hence, the Palmqvist approach is seemingly more sensitive to the change of the indentation fracture parameter with changing c/a.

Table 3.6: Comparison of experimentally determined α-values for the Palmqvist crack configuration using a log-log approach according to [34] and a linear approach according to [73].

ϕ / $^\circ$	SLG			FS		
	$\alpha_{ex,log-log}$	$\alpha_{ex,lin}$	% diff	$\alpha_{ex,log-log}$	$\alpha_{ex,lin}$	% diff
35.3	0.0210	0.0274	26.4	0.0159	0.0182	13.5
45	0.0188	0.0209	10.6	0.0115	0.0128	10.5
55	0.0123	0.0149	19.1	0.0084	0.0089	5.8
65.3	0.0091	0.0092	1.1	0.0044	0.0050	12.8

3.5 Subsurface Analysis

After surface analysis of the individual indents, subsurface analysis was also performed for some selected indents to reveal subsurface features of the crack morphologies and their influencing parameters using FIB serial sectioning and subsequent 3D reconstruction. The reconstructed indents for soda-lime glass are one 100 mN indent using a cube corner indenter (Figure 3.34) and two indents with a 45.0° indenter ($P = 75$ mN in Figure 3.35 and 100 mN in Figure 3.36).

In Figure 3.34, the 3D reconstruction of a 100 mN cube corner ($\phi = 35.3°$) indent in SLG is shown. The surface image of the indent is inset in the top right corner for navigation. Similar to the surface observation, three radial cracks (pink, orange, and yellow) emanate radially from the three corners of the blue trilateral indentation. However, in the subsurface it can be observed that those cracks terminate at what is assumed to be the elastic-plastic boundary, which will be discussed in detail in Section 3.5.1. Inside the plastic zone the high compressive stresses are assumed to either hinder crack growth or close existing cracks as the zone increases in size [29, 87–89]. In addition, there is another crack system that can only be observed in the subsurface at this load of 100 mN and not on the surface. These are the shallow-lateral cracks shown in green and light blue.

Figure 3.34: Subsurface cracking observations for a 100 mN indentation in SLG using a 35.3° indenter.
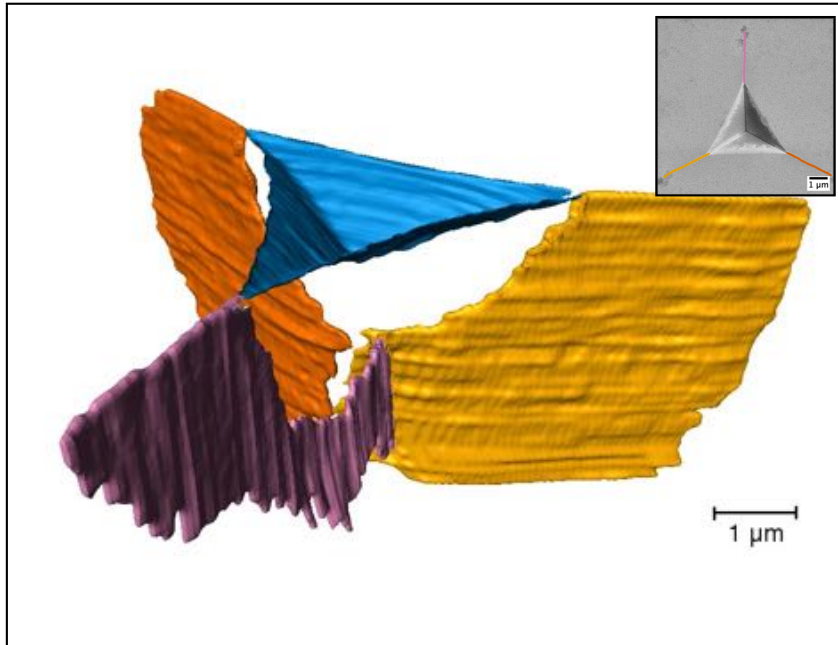
Figure 3.35: Subsurface cracking observations for a 75 mN indentation in SLG using a 45.0° indenter.

For indentation in SLG using a 45.0° indenter and a load of 75 mN as shown in Figure 3.35, similar observations can be made. The three radial cracks grow outward and terminate at the elastic-plastic boundary, but no shallow-lateral cracks are observed at these indentation parameters.
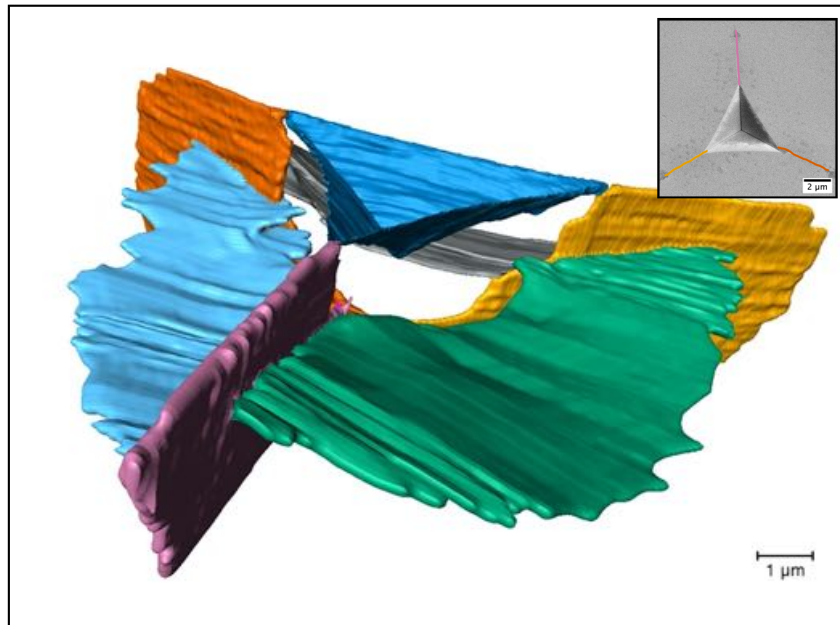
Figure 3.36: Subsurface cracking observations for a 100 mN indentation in SLG using a 45.0° indenter.

Comparing Figure 3.35 and Figure 3.36 shows that the shallow-lateral crack system also shows a cracking threshold. The shallow-lateral cracks (green, light blue, and gray) can be observed at 100 mN (Figure 3.36), but not at 75 mN (Figure 3.35). Hence they form at a higher load (75–100 mN) than the radial cracks (3–5 mN). This order has also been reported by Cuadrado et al. [61]. These lateral cracks are assumed to grow towards the surface at high enough loads and create "elephant ear" looking cracks at the surface when viewed in plan view (Figure 3.37b and Figure 3.37c). Similar behavior can also be observed for the cube corner indenter in Figure 3.3 and Figure 3.5 and the 55.0° indenter in Figure 3.4.

(a) P = 100 mN	(b) P = 300 mN	(c) P = 500 mN
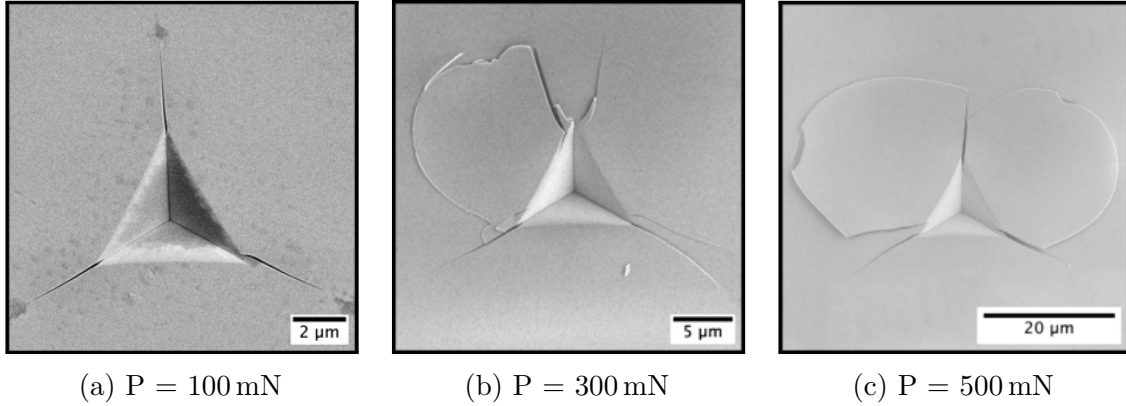
Figure 3.37: SEM micrographs of indentations at different loads with a 45.0° indenter in SLG as extracted from Figure 3.3 and Figure 3.4.

For fused silica, five indents were reconstructed: two each with a cube corner indenter ($P = 30\,\text{mN}$ in Figure 3.38 and $100\,\text{mN}$ in Figure 3.39) and a 45.0° indenter ($P = 75\,\text{mN}$ in Figure 3.43 and $100\,\text{mN}$ in Figure 3.44), as well as one $2\,\text{N}$ indent using a Berkovich indenter (Figure 3.45). For cube corner indentation in FS, the general crack observation are in agreement with observations for SLG. The difference is that FS shows edge cracks in addition to the radial cracks (green crack in Figure 3.38 and Figure 3.39). The surface images show edge cracks on each edge of the indentation, but only the crack along the left edge of the indentation could be reconstructed in three dimensions. The other two might have been too shallow to see in the cross section images. However, when comparing different loads for this geometry, then it can be observed that the edge crack starts in the center of the edge (Figure 3.38) and grows along the edge towards the corners (Figure 3.39). Furthermore, the edge cracks can be described as surface features, since they do not grow deep into the material (Figure 3.40). Depending on the geometry of the indenter, i.e. the center-line to face angle ϕ, the shape of the edge crack is different. For $\phi = 45.0°$ the edge cracks are extremely shallow and straight as shown Figure 3.40a, whereas for $\phi = 65.3°$ they are almost as deep as the indentation itself and show multiple wiggles as seen in Figure 3.40b.
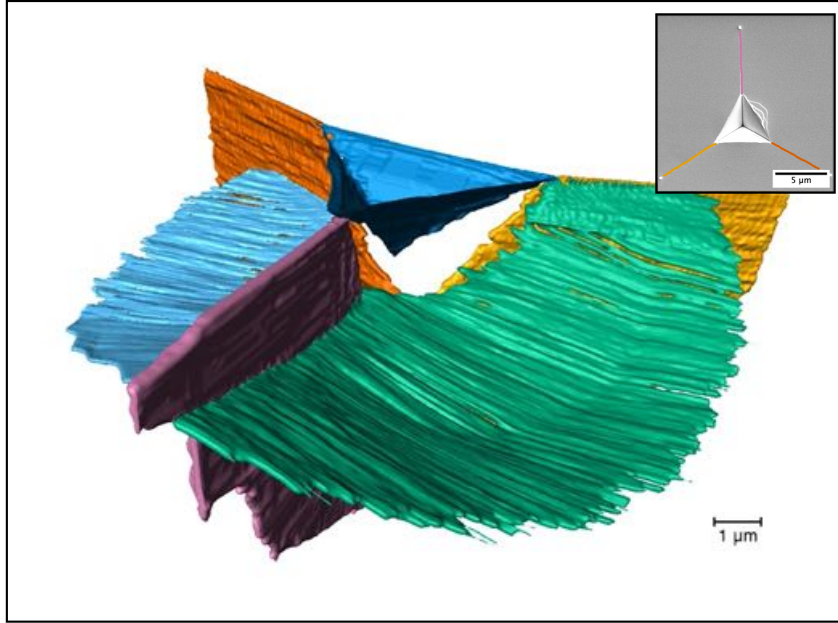
Figure 3.38: Subsurface cracking observations for a 30 mN indentation in FS using a 35.3° indenter.
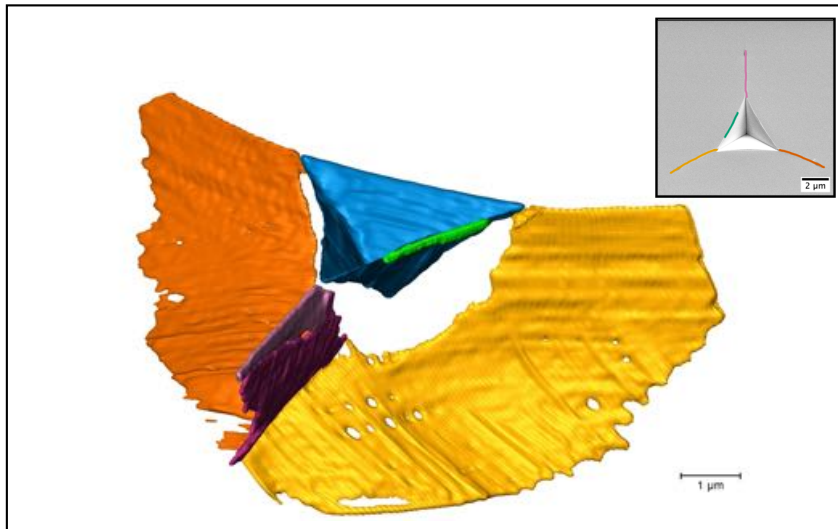
Figure 3.39: Subsurface cracking observations for a 100 mN indentation in FS using a 35.3° indenter.

Increasing the load also results in growth of the radial cracks, but they appear to grow down into the material and then turn the corner underneath the indent. This might be an indication that the cracks started on the surface, which is a characteristic of Palmqvist cracks. Another aspect that should be noted in Figure 3.39 is, that the front pink crack is depicted in two different shades of pink. In the individual cross sectional

slices there was a discontinuation of the crack as exemplified in Figure 3.41, that shows a break between the light pink Palmqvist crack and the magenta median crack. It is assumed that for this material Palmqvist-like cracks exist. It might be, that in this case (ϕ=35.3° and P=100 mN) both the Palmqvist and median crack systems are initiated. One counterargument is the fact that the previously described discontinuation could not be observed for the smaller 30 mN indent in Figure 3.38. However, since this is a relatively small indent, image quality issues could be a reason for not being able to detect the discontinuation. Schiffmann likewise showed FIB tomography for a 32 mN cube-corner indent in FS. They concluded that the cracks around the indentation are not perfectly semi-circular but rather of elliptical character, indicating that the crack morphology might be rather Palmqvist-like [90]. In addition to the discontinuation between the Palmqvist and the median crack, it can also be observed that the radial cracks are rather curvy in the subsurface. Those cracks are indicated by magenta and yellow arrows in Figure 3.41, although the crack indicated by the yellow is rather faint, since it is the back end of the crack that initiated at the bottom right corner in the inset surface image in Figure 3.39. A direct comparison of the shape of the radial crack in the subsurface can be seen in Figure 3.42, where the radial crack in SLG (center crack in Figure 3.42a) is almost perpendicular to the sample surface and the two radial cracks in FS (Figure 3.42b) curve outward away from the indentation.

Figure 3.42a also shows some pile-up just outside the hardness impression in SLG, whereas in FS (Figure 3.42b) the sample surface around the indentation remains flat. This difference in appearance might be one indication for the different deformation mechanisms. SLG typically deforms through shear processes, whereas FS typically deforms by densification [8–10]. Also, pile-up is dependent on the material properties, in particualar E/H. Pile-up typically occurs when E/H is high. Since E/H is higher for SLG then for FS, although only slightly (Table 3.2), it is not surprising that SLG shows pile-up and FS does not. SLG is densely packed with network modifiers content,
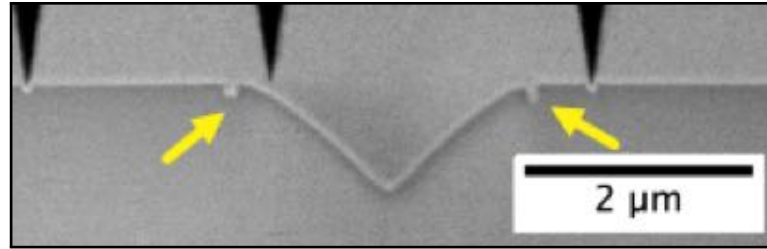
(a) $\phi = 45.0°$, $P = 75\,\mathrm{mN}$
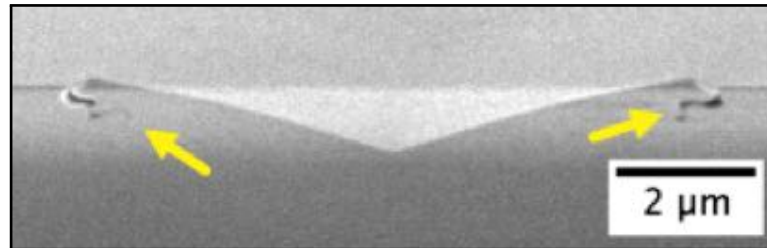
(b) $\phi = 65.3°$, $P = 1\,\mathrm{N}$

Figure 3.40: Edge crack morphology (highlighted by yellow arrows) for different indenter geometries in FS.

whereas FS has high free volume. Under high indentation compressive stress, SLG is easy to deform, leading to a larger pile-up height than FS [64, 91–94].
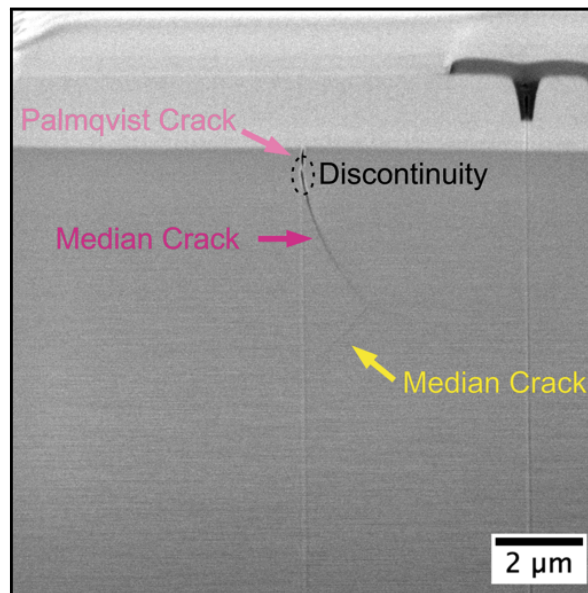
Figure 3.41: Cross sectional view along the pink radial crack in Figure 3.39.
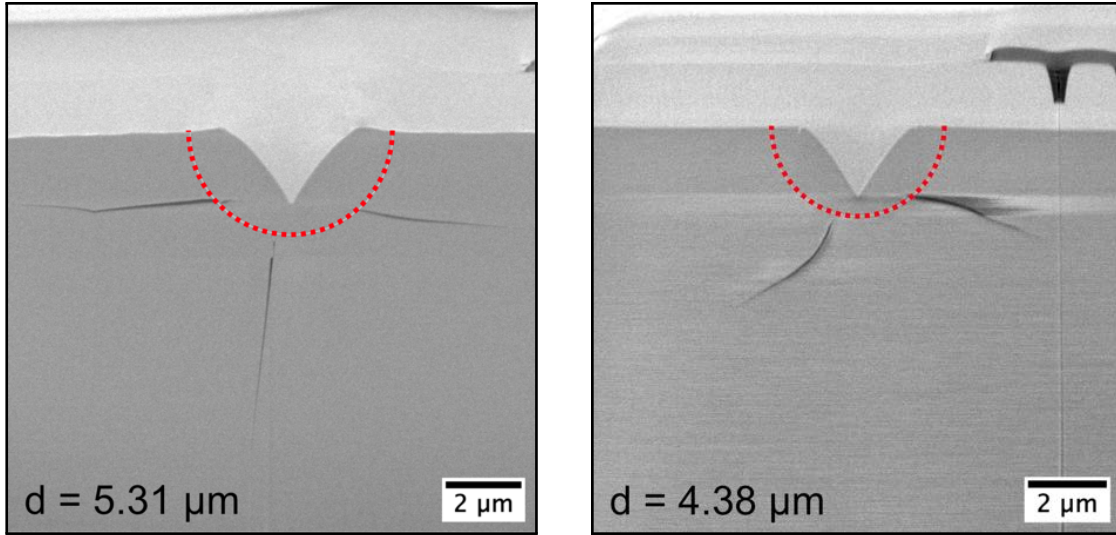
(a) Soda-lime glass   (b) Fused silica

Figure 3.42: Difference in shape of the radial crack for a $100\,\text{mN}$ indent using a cube corner indenter. Plastic zones (red dashed lines) and their sizes are also depicted.

When indenting with a slightly blunter $45.0°$ indenter at a load of $75\,\text{mN}$ (Figure 3.43), the radial cracks do not start at the corners of the indentation, but slightly offset along the edge of the indentation. It can also be observed that the radial cracks are connected to the edge cracks underneath the surface. The green edge crack connects to the pink and yellow radial crack, and the light blue edge crack connects to the orange radial crack. The front part of the pink radial crack again is of semi-elliptical shape, which is a characteristic of the Palmqvist crack morphology. Increasing the load by $25\,\text{mN}$ to $100\,\text{mN}$ (Figure 3.44) results in the pink Palmqvist radial growing down into the surface and filling into the median crack. The yellow radial crack grows down some amount as well and then turns the corner underneath the indent. The crack then grows almost parallel to the sample surface. That part of the crack could potentially also be a deep lateral crack that initiated from the radial crack.

The discontinuation as described before and shown in Figure 3.41 can also be observed during indentation with a Berkovich indenter (Figure 3.45). At a load of $2\,\text{N}$ radial cracks are initiated, but not until the additional cone crack has already initiated
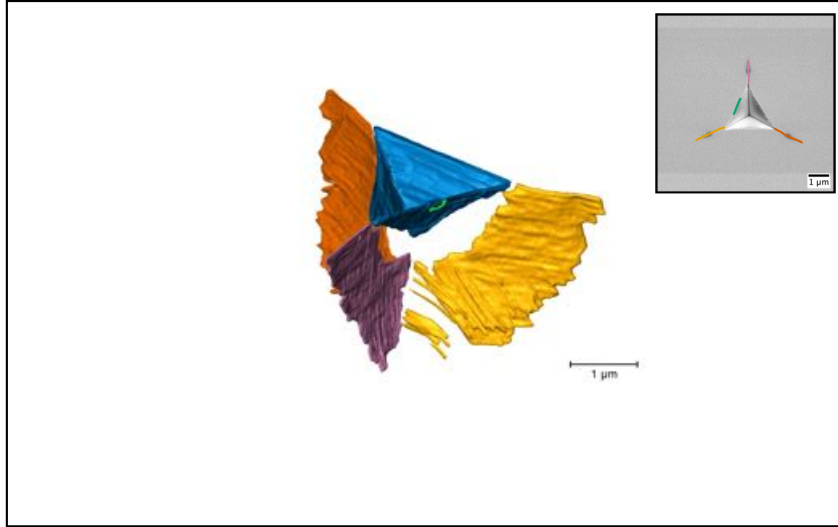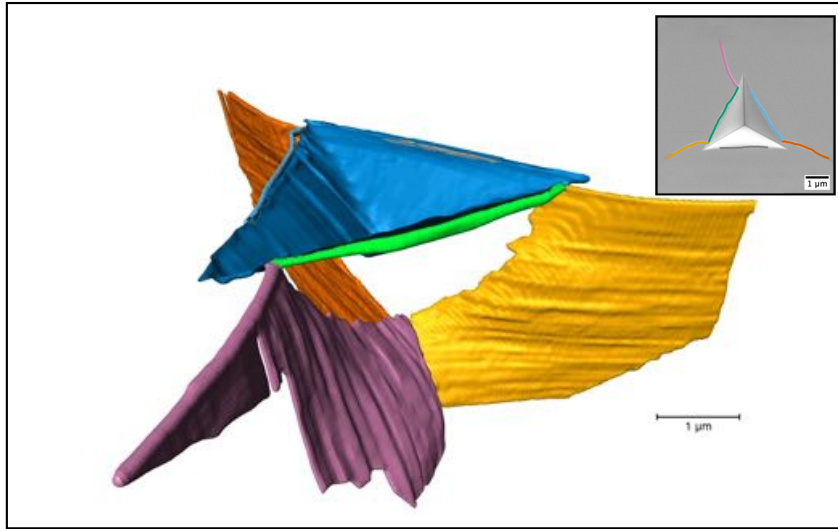
Figure 3.43: Subsurface cracking observations for a 75 mN indentation in FS using a 45.0° indenter.
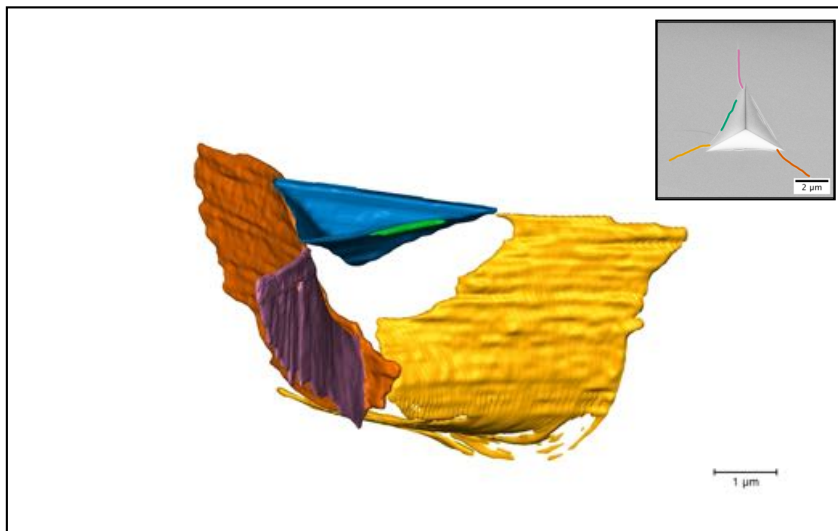
Figure 3.44: Subsurface cracking observations for a 100 mN indentation in FS using a 45.0° indenter.

at a lower load of 1 N (see Figure 3.6). This cone crack allows us to distinguish the Palmqvist- from the median-radial crack, as it acts as an arrest point for both. This discontinuation of radial cracks in Figure 3.45 was also observed by Li et al. [59] for the four-sided Vickers indenter. They attribute this discontinuation to the fact that cone cracks form first and then act as arrest points for radial cracks that form in a later
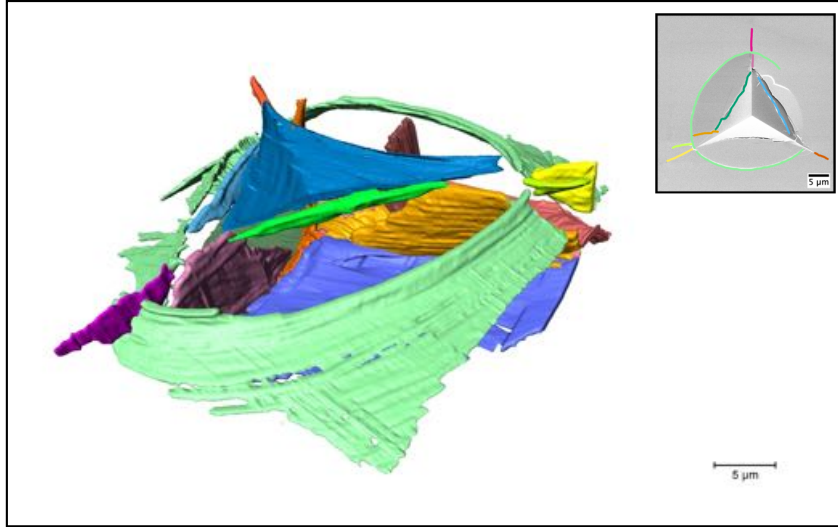
Figure 3.45: Subsurface cracking observations for a 2 N indentation in FS using a 65.3° indenter.

stage of the loading-unloading cycle. Similar observations are reported elsewhere in literature [6, 13, 95, 96]. Ishikawa and Shinkai [13] clearly state that Palmqvist-radial and median-radial cracks in fused silica grow independently and are separated by the cone crack, as seen in this work for Berkovich and Vickers indentations. Figure 3.45 also shows that, just at the cracking threshold for Berkovich indentation in FS, an abundance of cracks are initiated around the indentation, most of which have likely started prior to the surface radial cracks. This makes it questionable if the comparatively blunt Berkovich indenter is appropriate to use when trying to measure the fracture toughness. This observation is in agreement with experiments performed by Bruns et al. [38]. They show that multiple crack systems are activated during Berkovich indentation of FS.

3.5.1 Plastic Zone Sizes

When deriving equations necessary for the cracking threshold and the fracture toughness, an important parameter is the shape and size of the plastic zone. Figure 3.42 shows a comparison of the plastic zones for soda-lime glass (Figure 3.42a) and fused silica (Figure 3.42b). In both cases the depicted SEM image is the cross-sectional

view right underneath the apex of the indentation made by a cube corner indenter at $P = 100\,\mathrm{mN}$. The plastic zone is assumed to be hemispherical and to be maximal right underneath the indentation. No cracks are visible inside the elastic-plastic boundary, and therefore it is assumed that the cracks are initiated at the boundary, which agrees well with findings in literature [21, 61, 97]. Alternatively, it could be that cracks which have initiated previously are closed up by the growing plastic zone, which contains high compressive stresses. The location and size of the plastic zone at the end of indentation loading is estimated based on where the cracks terminate inside the material. The diameter of $5.31\,\mathrm{\mu m}$ for the plastic zone of SLG in Figure 3.42 is bigger than for FS, which is $4.38\,\mathrm{\mu m}$ in diameter. Li et al. showed that densification does affect the size and shape of the plastic zone. However, in their work the zone is larger when densification is considered in the FEA [98].

For a more accurate measurement of the plastic zone for the SLG indentation in Figure 3.46a, the side view in cross-section (Figure 3.46c) was considered in addition to the raw image of the bottom view (Figure 3.46b). Here the plastic zone once again was deduced from the termination of the cracks. The measured diameter is $5.24\,\mathrm{\mu m}$ and therefore very close to the value measured from the bottom cross sectional view in Figure 3.46b. These results confirm that the assumption of a nearly hemispherical plastic zone is valid.

Using the measurement from Figure 3.46 and overlaying it on the surface view of the indentation (Figure 3.47a) shows that the plastic zone is slightly smaller than the hardness impression. This, of course, is based on the assumption of a perfect half sphere for the plastic zone. Under the assumption of cracks growing from the elastic-plastic boundary, this observation is supported by the lateral subsurface view of the indentation and the cracks around it (Figure 3.47b). It is observed that the plastic zone beneath the surface does not extent all the way to the indentation corner. While the cracks on the surface do extent to the indentation corners (Figure 3.47a), there is a small region of

(c)

(a) Surface view.

(b) Cross-section from bottom.

(c) Cross-section from right.
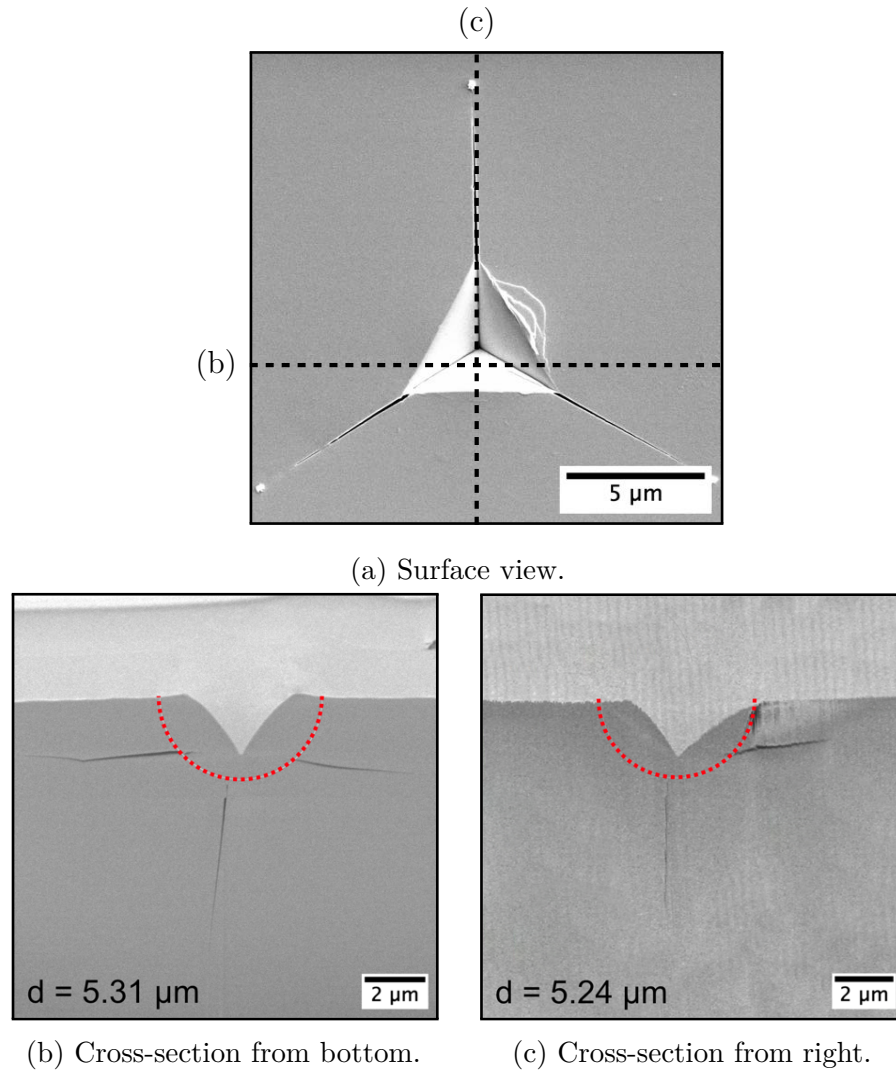
Figure 3.46: Measuring the plastic zone for a 100 mN cube-corner indent in SLG.

the yellow and orange cracks that touches the edge of the indentation in the subsurface and then grows along the elastic-plastic boundary. The horizontal distance between the points where the front left (yellow) and front right (orange) radial crack meet the indentation edge is 4.74 μm in Figure 3.47a and 5.55 μm in Figure 3.47b. Cuadrado et al. also observed that the plastic zone does not fully extent to the indentation corners [61].

An angular and load dependence of the plastic zone size is shown in the subsurface in Figure 3.48 and in the surface in Figure 3.49. For each case, the plastic zone can assumed to be hemispherical in shape as the red dotted semi-circles contact the cracks
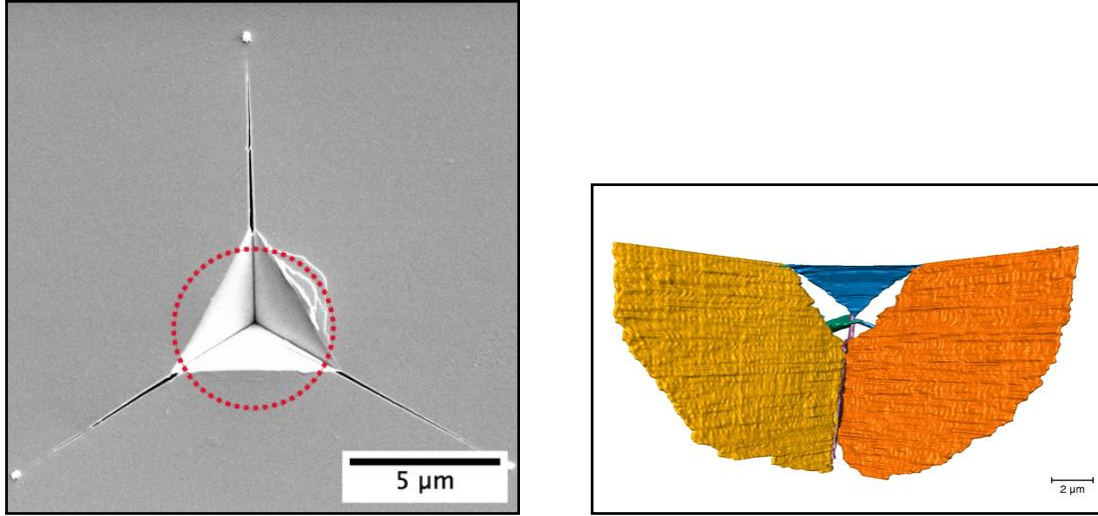
(a) Surface view including plastic zone.

(b) Subsurface lateral view.

Figure 3.47: Plastic zone size for a $100\,\text{mN}$ indent in SLG using a cube corner indenter. The plastic zone depicted is the zone measured in Figure 3.46 and the center of the circle is chosen to be the center of the indentation.

almost perfectly. Comparing different indenter angles ($\phi = 35.3°$ and $45.0°$ in Figure 3.48a and Figure 3.48b, respectively) at the same indentation load of $100\,\text{mN}$ shows that the plastic zone is bigger for the sharper indenter. The plastic zone also increases with increasing load, as shown in Figure 3.48b - d. Overlaying the measured plastic zone sizes in the surface micrographs (Figure 3.49) shows that for all investigated indentation parameters, the plastic zone is smaller than the indentation dimension a. When comparing Figure 3.49a and Figure 3.49b for different center-line to face angles at the same load, the relative plastic zone size $r_{plastic\,zone}/a$ is smaller for the blunter angle. Also, the relative plastic zone size increases with increasing load (Figure 3.49b - d).

An analysis equivalent to the one in Figure 3.46 for SLG was also performed for an indent in FS with the same indentation parameters, i.e., $P = 100\,\text{mN}$ and $\phi = 35.3°$. Similar to the results reported for SLG, the plastic zone size measured from the cross-sectional view of the raw image of the bottom view (Figure 3.50b) yields a value close to the measurement of the cross-sectional side view (Figure 3.50c). The diameter of the plastic zone size in Figure 3.50b and Figure 3.50c is $4.38\,\mu\text{m}$ and $4.57\,\mu\text{m}$, respectively.

(a) $\phi = 35.3°$, $P = 100\,\mathrm{mN}$

(b) $\phi = 45°$, $P = 100\,\mathrm{mN}$

(c) $\phi = 45°$, $P = 75\,\mathrm{mN}$

(d) $\phi = 45°$, $P = 80\,\mathrm{mN}$
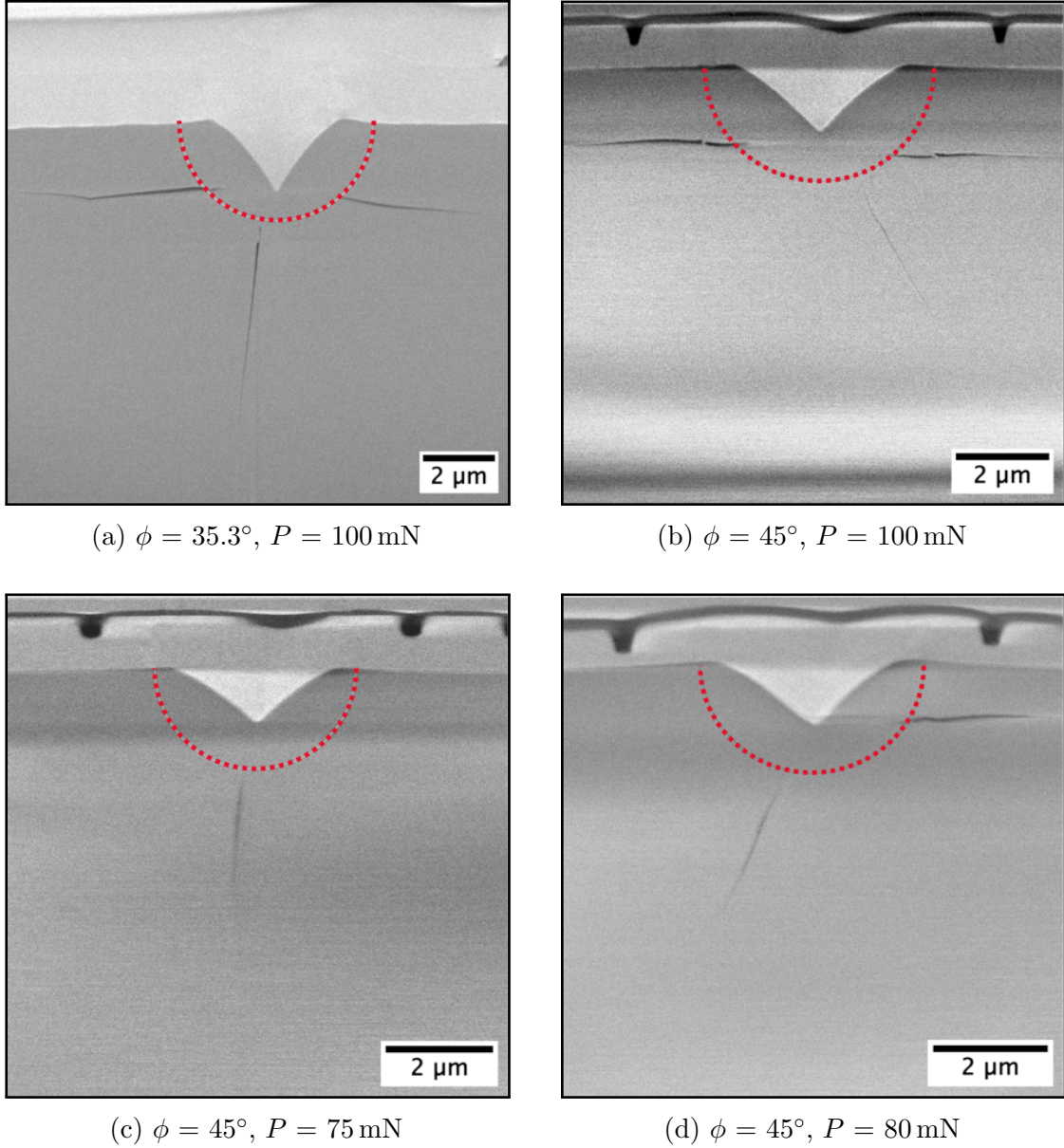
Figure 3.48: Subsurface view including plastic zones for different indents in SLG.

The plastic zone diameter $d_{plastic\,zone}$ and relative plastic zone size $r_{plastic\,zone}/a$ were also determined for nine different indents in FS in Figure 3.51 and Figure 3.52, respectively. Similar to the observations in SLG, a smaller load and a blunter center-line to face angle ϕ when compared at the same load yield a smaller plastic zone diameter. The plastic zone diameter for a cube corner indenter in Figure 3.51b is bigger than $d_{plastic\,zone}$ for a 45.0°-indenter in Figure 3.51c. For three different indenter

geometries, two three-sided tips with $\phi = 35.3°$ (Figure 3.51a and b) and $\phi = 45.0°$ (Figure 3.51c - f) and a four-sided Vickers tip with $\phi = 68.0°$ (Figure 3.51h and i), the plastic zone diameter increases with increasing load. However, the relative plastic zone size decreases with increasing load only for the cube corner indenter (Figure 3.52a and b), whereas $r_{plastic\,zone}/a$ increases with load for both the $\phi = 45.0°$ (Figure 3.52c - f) and $\phi = 68.0°$ (Figure 3.52h and i).

(a) $\phi = 35.3°$, $P = 100\,\text{mN}$

(b) $\phi = 45°$, $P = 100\,\text{mN}$

(c) $\phi = 45°$, $P = 75\,\text{mN}$

(d) $\phi = 45°$, $P = 80\,\text{mN}$
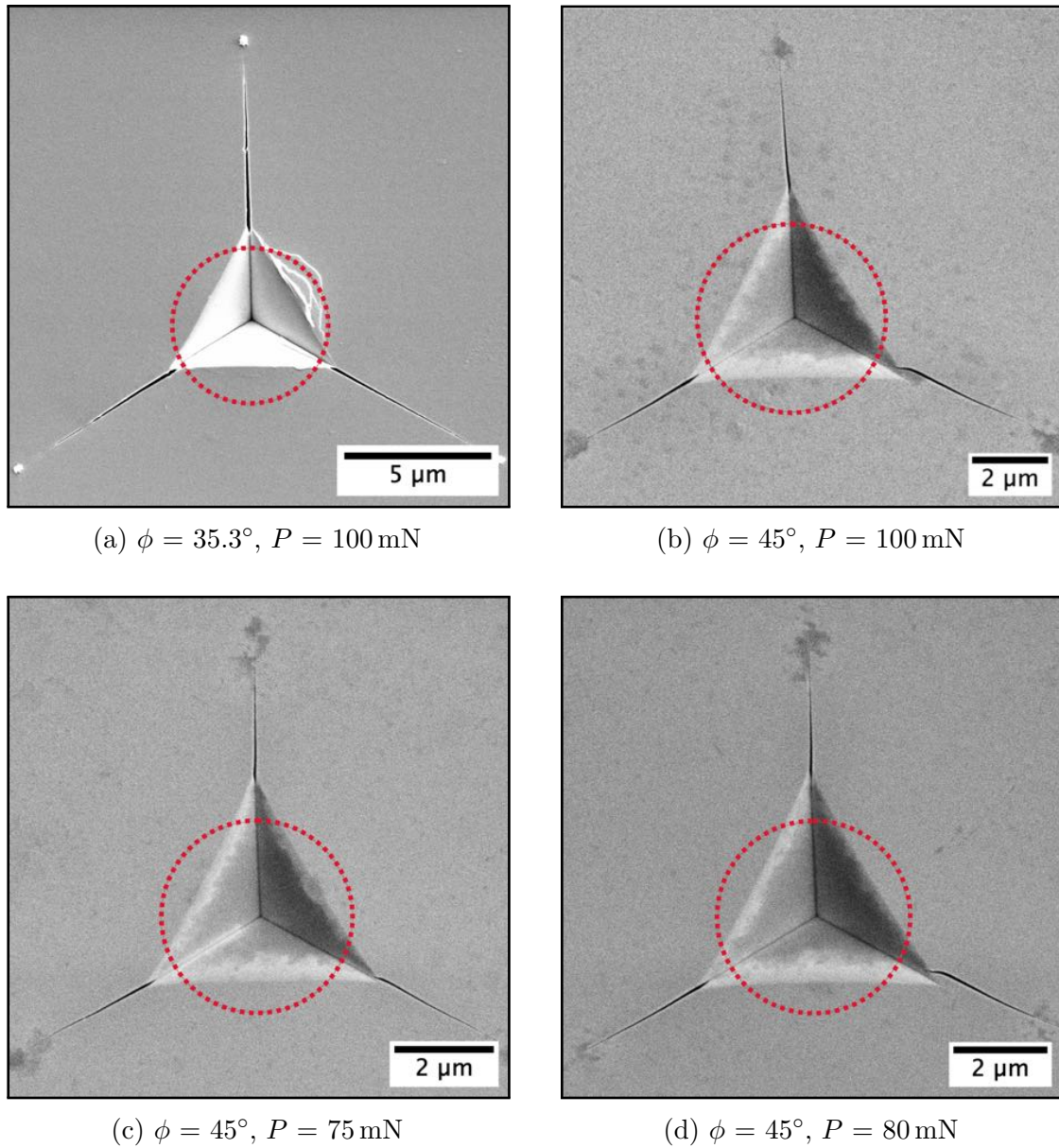
Figure 3.49: Surface view including plastic zones for different indents in SLG.

The material, load, and angular dependencies of the plastic zone diameter $d_{plastic\,zone}$ and the relative plastic zone size $r_{plastic\,zone}/a$ are summarized in Figure 3.53a and Figure 3.53b, respectively.

(a) Surface view.

(b) Cross-section from bottom.

(c) Cross-section from right.
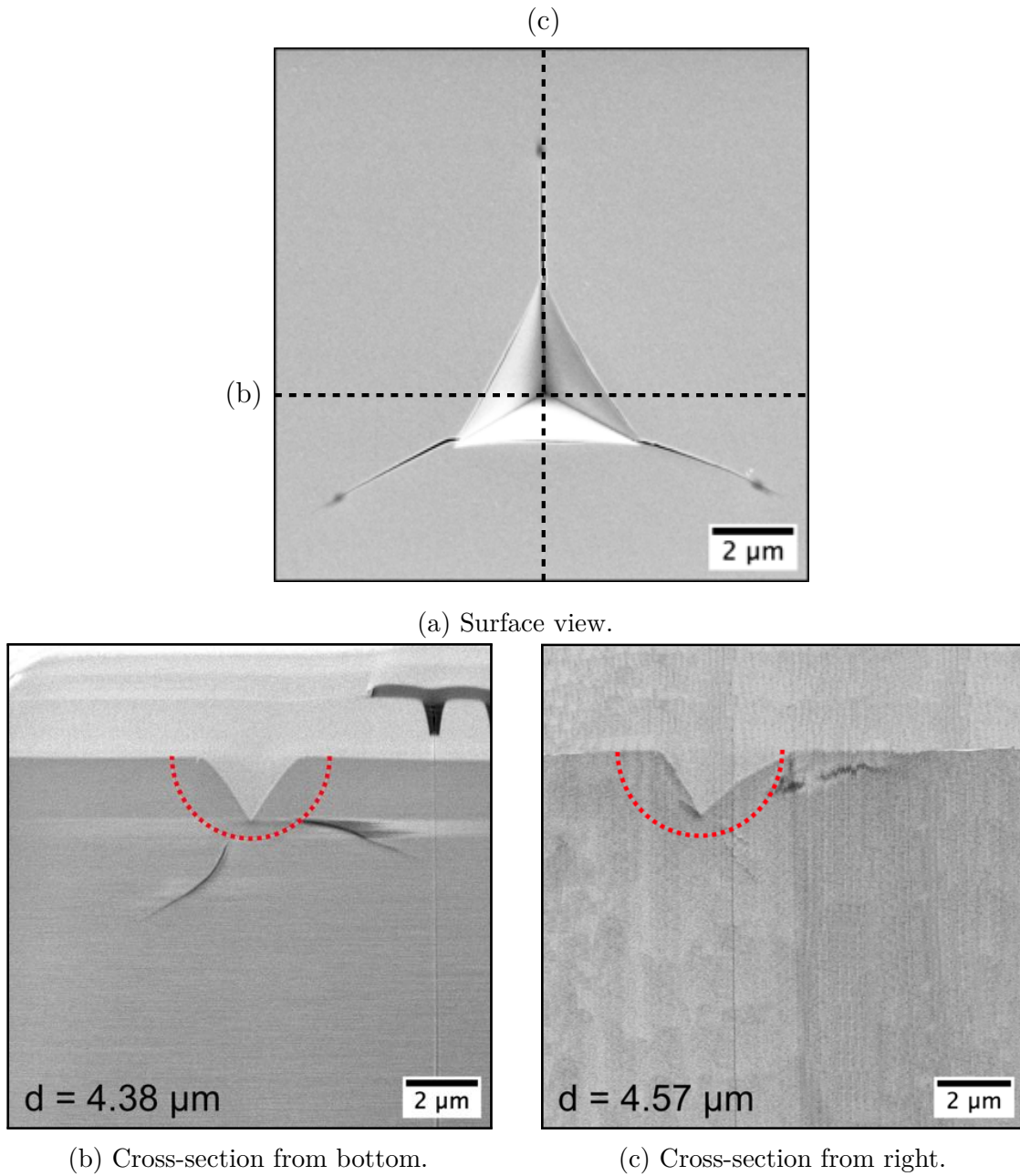
Figure 3.50: Measuring the plastic zone for a 100 mN cube-corner indent in FS.
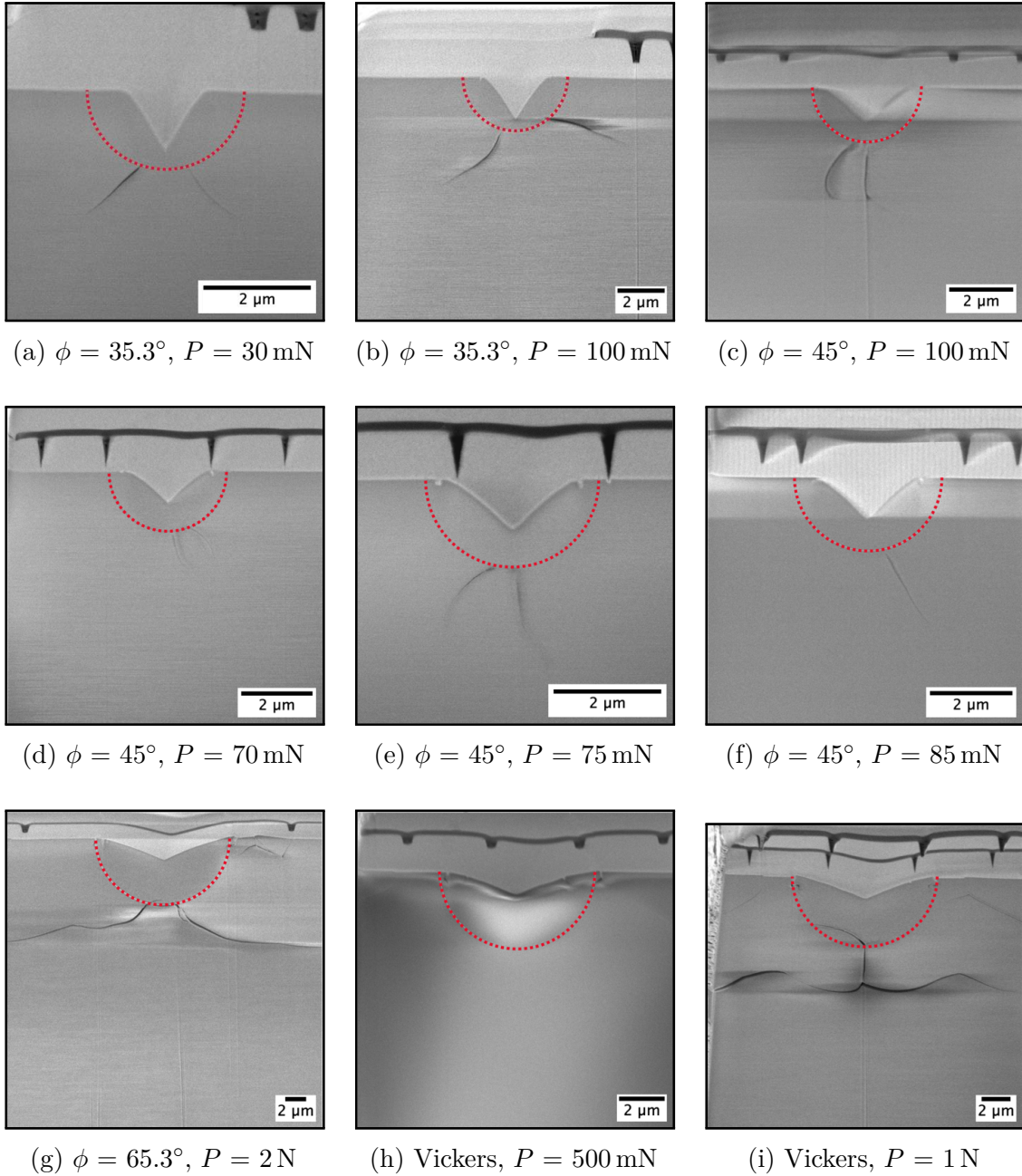
(a) $\phi = 35.3°$, $P = 30\,\text{mN}$ (b) $\phi = 35.3°$, $P = 100\,\text{mN}$ (c) $\phi = 45°$, $P = 100\,\text{mN}$

(d) $\phi = 45°$, $P = 70\,\text{mN}$ (e) $\phi = 45°$, $P = 75\,\text{mN}$ (f) $\phi = 45°$, $P = 85\,\text{mN}$

(g) $\phi = 65.3°$, $P = 2\,\text{N}$ (h) Vickers, $P = 500\,\text{mN}$ (i) Vickers, $P = 1\,\text{N}$

Figure 3.51: Suburface view including plastic zones for different indents in FS.

(a) $\phi = 35.3°$, $P = 30\,\text{mN}$ (b) $\phi = 35.3°$, $P = 100\,\text{mN}$ (c) $\phi = 45°$, $P = 100\,\text{mN}$

(d) $\phi = 45°$, $P = 70\,\text{mN}$ (e) $\phi = 45°$, $P = 75\,\text{mN}$ (f) $\phi = 45°$, $P = 85\,\text{mN}$

(g) $\phi = 65.3°$, $P = 2\,\text{N}$ (h) Vickers, $P = 500\,\text{mN}$ (i) Vickers, $P = 1\,\text{N}$
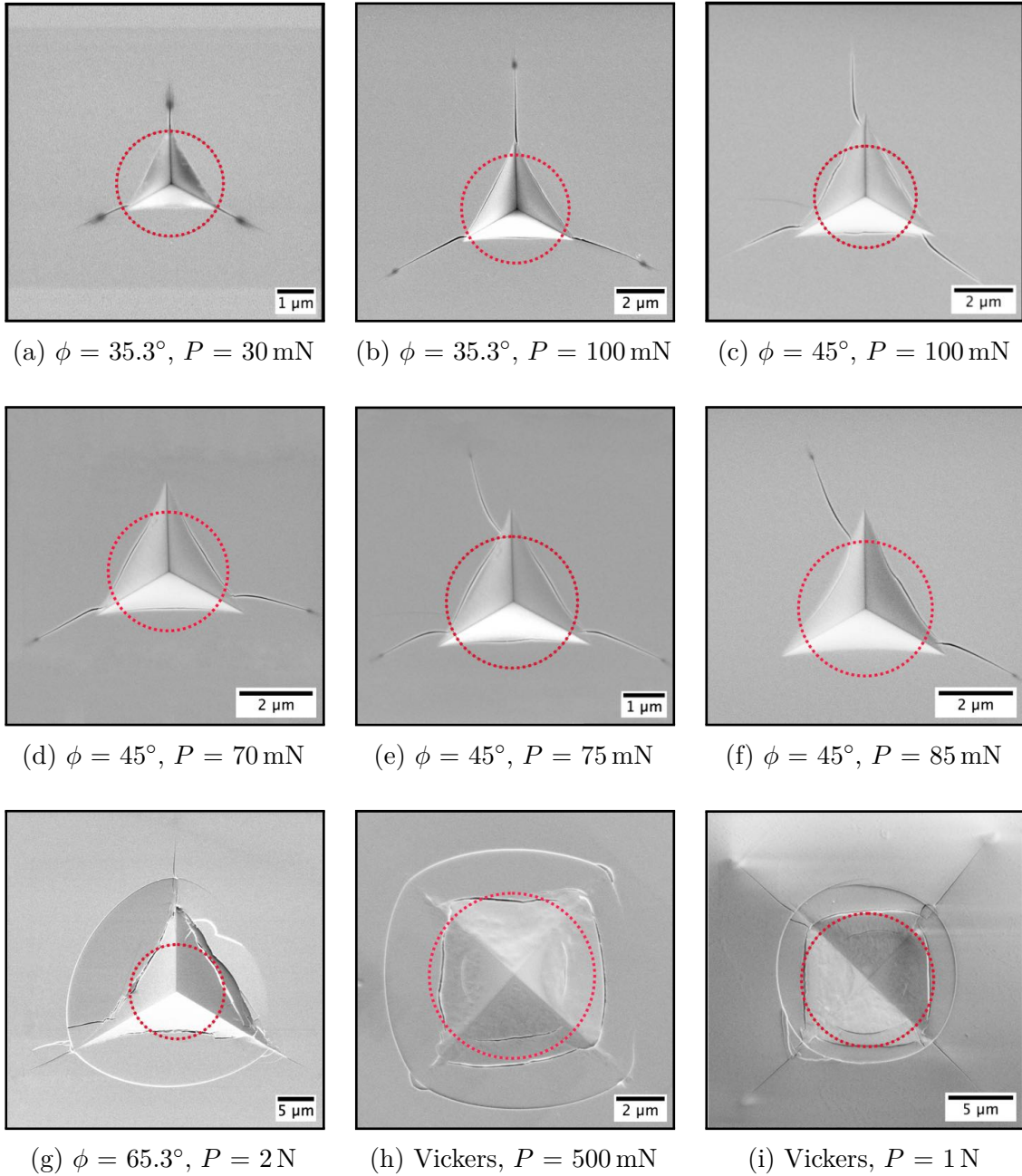
Figure 3.52: Surface view including plastic zones for different indents in fused silica.

(a) Plastic zone diameter   (b) Relative plastic zone size
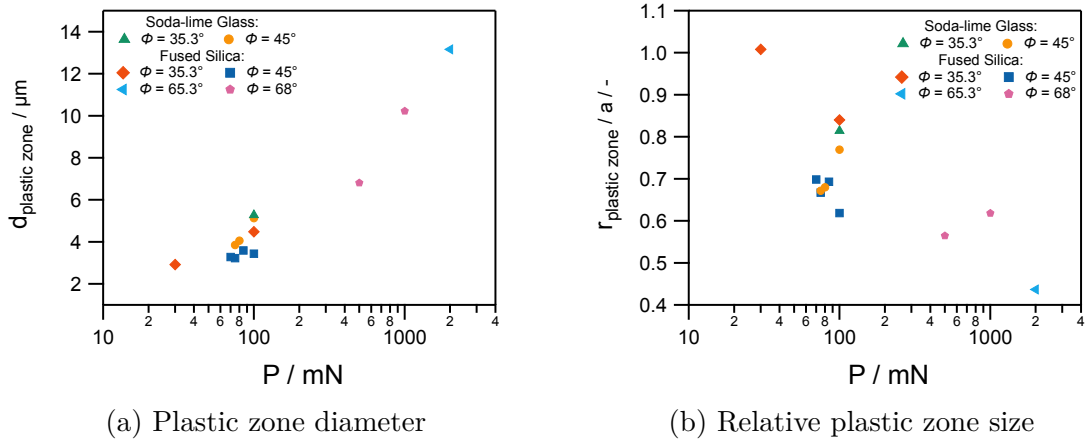
Figure 3.53: Angular, material, and load dependency of the plastic zone.

When comparing the two materials at $P = 100\,\mathrm{mN}$, for both angles ($\phi = 35.3°$ and $\phi = 45.0°$) SLG shows a higher plastic zone diameter than FS. The relative plastic zone size of SLG is higher than FS for the 45.0°- indenter, but lower for the cube corner indenter. The overall trend across all four angles and the two materials is increasing with load for the plastic zone diameter (Figure 3.53a) and decreasing with load for the relative plastic zone size (Figure 3.53b). Cuadrado et al. observed that when SLG is indented using a cube corner indenter, the relative plastic zone decreases as load increases and cracks propagate, which is in agreement with results in this work [61]. Utilizing Hill's expanding cavity solution, Jang and Pharr reported a relation for the relative plastic zone size, which shows a dependency on ϕ and E/H [34]. As ϕ increases, their model results in a relative plastic zone size decrease, and higher E/H results in higher relative plastic zone sizes [34]. These dependencies are in agreement with the measurements in Figure 3.53b. Also, using the relation reported by Jang and Pharr [34] to compute the magnitude of the relative plastic zone size yields values close to unity for the sharp cube corner indenter and lower values at around 0.6 for the Berkovich indenter, which is fairly consistent with the measurements here.

4. SUMMARY AND CONCLUSIONS

The objective of this work was to further the understanding of the cracking behavior of silicate glasses. Hence, nanoindentation and subsequent high resolution imaging was performed on two silicate glasses, soda-lime glass (SLG) and fused silica (FS) as representative for normal and anomalous glasses, respectively. In addition to the material dependency, an angular dependency as well as a loading dependency were investigated. For each material, four trigonal indenters with different center-line to face angles ϕ and about 20 discrete indentation loads P were tested. Important cracking parameters are summarized in Table 4.1. In all cases, the experimentally determined values are reported here, since not all of them could be validated using fracture mechanics theories.

Table 4.1: Overview of important fracture parameters determined in this work.

	ϕ / °	35.3	45.0	55.0	65.3
SLG	$P_{c,radial}$ / mN	1–3	3–5	10–30	3000–5000
	$P_{c,edge}$ / mN	✗	✗	✗	100–250
	α_M / - *	0.0612	0.0476	0.0347	0.0266
	α_P / - *	0.0210	0.0188	0.0123	0.0091
FS	$P_{c,radial}$ / mN	3–10	65–75	500–1000	1000–2000
	$P_{c,edge}$ / mN	3–10	< 3	< 3	< 3
	α_M / - *	0.0491	0.0299	0.0232	0.0097
	α_P / - *	0.0159	0.0115	0.0084	0.0044

* Values are reported according to the log-log approach [34].
✗: No cracks are observed in tested load range ($P = 1\,\text{mN-20\,N}$).

In conclusion, the following key findings can be reported.

- There are distinct thresholds for radial and edge cracks in SLG and FS, which depend sensitively on the indenter angle and the indented material. Radial cracks typically occur at lower indenter loads for sharper indenter angles and at

lower loads in SLG than in FS. The only exception is the Berkovich indenter, for which the cracking threshold P_c is lower for FS than for SLG. No distinct angular dependency could be determined for the edge cracks. However, edge cracks occur earlier in FS than in SLG. In SLG, only the comparatively blunt Berkovich can introduce edge cracks around the indentation impression, but for scenarios in which edge cracks do occur, they initiate prior to the radial cracks. Additionally, shallow lateral cracks have been observed in SLG, which initiate in a later stage than the radial cracks. Likewise in FS an additional crack morphology is introduced when the Berkovich indenter is used, the cone crack, which initiates after the edge crack, but prior to the radial crack.

- The Harding model [24] adequately describes the angular dependency of the radial cracking threshold for soda lime glass as $P_{c,radial}$ follows $(\tan \phi)^{8/3}$, but not for fused silica, where the exponent is significantly higher at close to about 9. However, for SLG the model can only be used for center-line to face angles between 35.3° and 55.0°, and breaks down for the Berkovich tip. While the angular dependency for SLG is described by the model, the magnitude of $P_{c,radial}$ is underestimated when it is assumed that cracks start at $c/a = 1$. Using c/a closer to 1.4 seems more appropriate to determine the magnitude of $P_{c,radial}$.

- It is critical to know the crack morphology to measure the fracture toughness K_c adequately. SLG seems to crack median-like, whereas FS seems to have Palmqvist-like cracking characteristics. Utilizing theoretical relations for the correct crack morphology, the relations can be used to estimate the fracture toughness, even for $\frac{c}{a} < 2.5$. Relations for the median crack system developed by Jang and Pharr [34] estimate K_c for SLG quite accurately. Relations based on Niihara's work developed in this work overestimate K_c significantly, but present a good starting point to mitigate the strong deviation with c/a for FS [74].

- From subsurface investigation it is concluded that edge cracks do not extend very far into the material, but may influence the initiation of radial cracks. Furthermore, radial cracks are only visible in the subsurface, when they can also be observed on the surface. This is an important observation, because this allows one to conduct the simpler surface investigation. Lastly, radial cracks appear to terminate at what can be assumed to be the elastic-plastic boundary, which is at most as big as the indentation. However, as load increases the size of plastic zone relative to the hardness impression decreases.

REFERENCES

[1] J. H. Lee, Y. F. Gao, K. E. Johanns, and G. M. Pharr. "Cohesive interface simulations of indentation cracking as a fracture toughness measurement method for brittle materials". *Acta Materialia* 60.15 (2012), pp. 5448–5467.

[2] B. R. Lawn and A. G. Evans. "A model for crack initiation in elastic/plastic indentation fields". *Journal of Materials Science* 12.11 (1977), pp. 2195–2199.

[3] Micro Star Technologies. *NANO INDENTERS*. Micro Star Technologies, 2009.

[4] J. J. Kang, A. A. Becker, and W. Sun. "Determining elastic–plastic properties from indentation data obtained from finite element simulations and experimental results". *International Journal of Mechanical Sciences* 62.1 (2012), pp. 34–46.

[5] J. E. Shelby. *Introduction to Glass Science and Technology*. 2nd ed. The Royal Society of Chemistry, 2006.

[6] A. Arora, D. B. Marshall, B. R. Lawn, and M. V. Swain. "Indentation deformation/fracture of normal and anomalous glasses". *Journal of Non-Crystalline Solids* 31.3 (1979), pp. 415–428.

[7] S. Yoshida. "Indentation deformation and cracking in oxide glass –toward understanding of crack nucleation". *Journal of Non-Crystalline Solids: X* 1 (2019), p. 100009.

[8] Y. Kato, H. Yamazaki, S. Yoshida, and J. Matsuoka. "Effect of densification on crack initiation under Vickers indentation test". *Journal of Non-Crystalline Solids* 356.35-36 (2010), pp. 1768–1773.

[9] W. Wang, Z. Li, P. Yao, J. Li, F. Chen, and Y. Liu. "Sink-in/pile-up formation and crack nucleation mechanisms of high purity fused silica and soda-lime silica

glass during nanoindentation experiments". *Ceramics International* 46.15 (2020), pp. 24698–24709.

[10]   S. Yoshida, J.-C. Sanglebœuf, and T. Rouxel. "Indentation-induced densification of soda-lime silicate glass". *International Journal of Materials Research* 98.5 (2007), pp. 360–364.

[11]   K. Asai, S. Yoshida, A. Yamada, J. Matsuoka, A. Errapart, and C. R. Kurkjian. "Micro-Photoelastic Evaluation of Indentation-Induced Stress in Glass". *Materials Transactions* 60.8 (2019), pp. 1423–1427.

[12]   S. Yoshida, S. Iwata, T. Sugawara, Y. Miura, J. Matsuoka, A. Errapart, and C. R. Kurkjian. "Elastic and residual stresses around ball indentations on glasses using a micro-photoelastic technique". *Journal of Non-Crystalline Solids* 358.24 (2012), pp. 3465–3472.

[13]   H. Ishikawa and N. Shinkai. "Critical Load for Median Crack Initiation in Vickers Indentation of Glasses". *Journal of the American Ceramic Society* 65.8 (1982), pp. C-124–C-127.

[14]   R. F. Cook. "Fracture sequences during elastic–plastic indentation of brittle materials". *Journal of Materials Research* 34.10 (2019), pp. 1633–1644.

[15]   S. Yoshida, M. Kato, A. Yokota, S. Sasaki, A. Yamada, J. Matsuoka, N. Soga, and C. R. Kurkjian. "Direct observation of indentation deformation and cracking of silicate glasses". *Journal of Materials Research* 30.15 (2015), pp. 2291–2299.

[16]   S. Yoshida, K. Wada, T. Fujimura, A. Yamada, M. Kato, J. Matsuoka, and N. Soga. "Evaluation of Sinking-In and Cracking Behavior of Soda-Lime Glass under Varying Angle of Trigonal Pyramid Indenter". *Frontiers in Materials* 3 (2016), pp. 415–9.

[17] A. P. Buang, R. Liu, X. J. Wu, and M. X. Yao. "Cracking analysis of HVOF coatings under Vickers indentation". *Journal of Coatings Technology and Research* 5.4 (2008), pp. 513–534.

[18] F. Lofaj and D. Németh. "Multiple cohesive cracking during nanoindentation in a hard W-C coating/steel substrate system by FEM". *Journal of the European Ceramic Society* 37.14 (2017), pp. 4379–4388.

[19] P. Yao, W. Wang, C. Z. Huang, J. Wang, H. T. Zhu, and T. Kuriyagawa. "Indentation Crack Initiation and Ductile to Brittle Transition Behavior of Fused Silica". *Advanced Materials Research* 797 (2013), pp. 667–672.

[20] J. Chen. "Indentation-based methods to assess fracture toughness for thin coatings". *Journal of Physics D: Applied Physics* 45.20 (2012), pp. 203001–15.

[21] B. A. Mound and G. M. Pharr. "Nanoindentation of Fused Quartz at Loads Near the Cracking Threshold". *Exp. Mech.* 10.6 (2019), pp. 1049–14.

[22] B. R. Lawn and D. B. Marshall. "Hardness, Toughness, and Brittleness: An Indentation Analysis". *Journal of the American Ceramic Society* 62.7-8 (1979), pp. 347–350.

[23] J. T. Hagan. "Micromechanics of crack nucleation during indentations". *Journal of Materials Science* 14.12 (1979), pp. 2975–2980.

[24] D. S. Harding. "Cracking in Brittle Materials During Low-Load Indentation and its Relation to Fracture Toughness". *Rice University, Houston, TX* (1995).

[25] A. N. Stroh. "A Theory of the Fracture of Metals". *Advances in Physics* 6.24 (1957), pp. 418–465.

[26] W. C. Oliver and G. M. Pharr. "An improved technique for determining hardness and elastic modulus using load and displacement sensing indentation experiments". *Journal of Materials Research* 7.6 (1992), pp. 1564–1583.

[27] B. R. Lawn, A. G. Evans, and D. B. Marshall. "Elastic/Plastic Indentation Damage in Ceramics: The Median/Radial Crack System". *Journal of American Ceramic Society* 63.9-10 (1980), pp. 574–581.

[28] P. Sellappan, T. Rouxel, F. Celarie, E. Becker, P. Houizot, and R. Conradt. "Composition dependence of indentation deformation and indentation cracking in glass". *Acta Materialia* 61.16 (2013), pp. 5949–5965.

[29] S. S. Chiang, D. B. Marshall, and A. G. Evans. "The response of solids to elastic/plastic indentation. II. Fracture initiation". *Journal of Applied Physics* 53.1 (1982), pp. 312–317.

[30] J. P. Guin, T. Rouxel, J.-C. Sanglebœuf, I. Melscoët, and J. Lucas. "Hardness, Toughness, and Scratchability of Germanium–Selenium Chalcogenide Glasses". *Journal of the American Ceramic Society* 85.6 (2002), pp. 1545–1552.

[31] T. Rouxel and S. Yoshida. "The fracture toughness of inorganic glasses". *Journal of the American Ceramic Society* 100.10 (2017), pp. 4374–4396.

[32] G. Scannell, D. Laille, F. Celarie, L. Huang, and T. Rouxel. "Interaction between Deformation and Crack Initiation under Vickers Indentation in Na2O–TiO2–SiO2 Glasses". *Frontiers in Materials* 4 (2017), pp. 175–10.

[33] T. M. Gross. "Deformation and cracking behavior of glasses indented with diamond tips of various sharpness". *Journal of Non-Crystalline Solids* 358.24 (2012), pp. 3445–3452.

[34] J.-i. Jang and G. M. Pharr. "Influence of indenter angle on cracking in Si and Ge during nanoindentation". *Acta Materialia* 56.16 (2008), pp. 4458–4469.

[35] D. B. Marshall, R. F. Cook, N. P. Padture, M. L. Oyen, A. Pajares, J. E. Bradby, I. E. Reimanis, R. Tandon, T. F. Page, G. M. Pharr, and B. R. Lawn. "The Compelling Case for Indentation as a Functional Exploratory and Characterization Tool". *Journal of the American Ceramic Society* 98.9 (2015), pp. 2671–2680.

[36] G. R. Anstis, P. Chantikul, B. R. Lawn, and D. B. Marshall. "A Critical Evaluation of Indentation Techniques for Measuring Fracture Toughness: I, Direct Crack Measurements". *Journal of American Ceramic Society* 64.9 (1981), pp. 533–538.

[37] J. Gong, Y. Chen, and C. Li. "Statistical analysis of fracture toughness of soda-lime glass determined by indentation". *Journal of Non-Crystalline Solids* 279.2-3 (2001), pp. 219–223.

[38] S. Bruns, L. Petho, C. Minnert, J. Michler, and K. Durst. "Fracture toughness determination of fused silica by cube corner indentation cracking and pillar splitting". *JMADE* 186 (2020), p. 108311.

[39] S. Palmqvist. "Rissbildungsarbeit bei Vickers-Eindrücken als Maß für die Zähigkeit von Hartmetallen". *Archiv für das Eisenhüttenwesen* 9 (1962), pp. 629–634.

[40] R. F. Cook and G. M. Pharr. "Direct Observation and Analysis of Indentation Cracking in Glasses and Ceramics". *Journal of the American Ceramic Society* 73.4 (1990), pp. 787–817.

[41] M. Kang, W. Li, A. F. T. Leong, M. Guan, K. Fezzaa, J. T. Harris, K. T. Ramesh, and T. C. Hufnagel. "Crack nucleation and growth during dynamic indentation of chemically-strengthened glass". *Extreme Mechanics Letters* 38 (2020), p. 100754.

[42] K. Niihara, R. Morena, and D. P. H. Hasselman. "Evaluation of K_{Ic} of brittle solids by the indentation method with low crack-to-indent ratios". *Journal of Materials Science Letters* 1.1 (1982), pp. 13–16.

[43] M. Sakai and R. C. Bradt. "Fracture toughness testing of brittle materials". *International Materials Reviews* 38 (1993), pp. 53–78.

[44] K. E. Johanns, J. H. Lee, Y. F. Gao, and G. M. Pharr. "An evaluation of the advantages and limitations in simulating indentation cracking with cohesive zone finite elements". *Modelling and Simulation in Materials Science and Engineering* 22.1 (2014), pp. 015011–22.

[45] G. M. Pharr, D. S. Harding, and W. C. Oliver. "Measurement of Fracture Toughness in Thin Films and Small Volumes Using Nanoindentation Methods". *Mechanical Properties and Deformation Behavior of Materials Having Ultra-Fine Microstructures.* Dordrecht: Springer Netherlands, 1993, pp. 449–461.

[46] D. J. Morris and R. F. Cook. "In Situ Cube-Corner Indentation of Soda-Lime Glass and Fused Silica". *Journal of the American Ceramic Society* 87 (2004), pp. 1494–1501.

[47] D. J. Morris, A. M. Vodnick, and R. F. Cook. "Radial Fracture During Indentation by Acute Probes: II, Experimental Observations of Cube-corner and Vickers Indentation". *International Journal of Fracture* 136 (2005), pp. 265–284.

[48] T. W. Scharf, H. Deng, and J. A. Barnard. "Mechanical and fracture toughness studies of amorphous SiC–N hard coatings using nanoindentation". *Journal of Vacuum Science & Technology A: Vacuum, Surfaces, and Films* 15.3 (1998), p. 963.

[49] T. Scholz, G. A. Schneider, J. Muñoz-Saldaña, and M. V. Swain. "Fracture toughness from submicron derived indentation cracks". *Applied Physics Letters* 84.16 (2004), pp. 3055–3057.

[50] S. Bruns, K. E. Johanns, H. U. R. Rehman, G. M. Pharr, and K. Durst. "Constitutive modeling of indentation cracking in fused silica". *Journal of the American Ceramic Society* 100.5 (2017), pp. 1928–1940.

[51] R. D. Dukino and M. V. Swain. "Comparative Measurement of Indentation Fracture Toughness with Berkovich and Vickers Indenters". *Journal of the American Ceramic Society* 75.12 (1992), pp. 3299–3304.

[52] M. T. Laugier. "New formula for indentation toughness in ceramics". *Journal of Materials Science Letters* 6 (1987), pp. 355–356.

[53] D. K. Shetty, I. G. Wright, P. N. Mincer, and A. H. Clauer. "Indentation fracture of WC-Co cermets". *Journal of Materials Science* 20.5 (1985), pp. 1873–1882.

[54] T. Lube. "Indentation crack profiles in silicon nitride". *Journal of European Ceramic Society* 21 (2001), pp. 211–218.

[55] *E438 Specification for Glasses in Laboratory Apparatus.* ASTM International. West Conshohocken, PA, 2011.

[56] *C1327 Standard Test Method for Vickers Indentation Hardness of Advanced Ceramics.* ASTM International. West Conshohocken, PA, 2019.

[57] *E384 Microindentation Hardness of Materials.* ASTM International. West Conshohocken, PA, 2021.

[58] S. Lathabai, J. Rödel, T. Dabbs, and B. R. Lawn. "Fracture mechanics model for subthreshold indentation flaws". *Journal of Materials Science* 26.8 (1991), pp. 2157–2168.

[59] C. Li, J. Ding, L. Zhang, C. Wu, L. Sun, Q. Lin, Y. Liu, and Z. Jiang. "Densification effects on the fracture in fused silica under Vickers indentation". *Ceramics International* 48.7 (2022), pp. 9330–9341.

[60] B. A. Mound. "Cracking in Fused Quartz During Nanoindentation". PhD thesis. 2017.

[61] N. Cuadrado, J. Seuba, D. Casellas, M. Anglada, and E. Jiménez-Piqué. "Geometry of nanoindentation cube-corner cracks observed by FIB tomography: Implication for fracture resistance estimation". *Journal of the European Ceramic Society* 35.10 (2015), pp. 2949–2955.

[62] H. Sawasato, S. Yoshida, T. Sugawara, Y. Miura, and J. Matsuoka. "Relaxation behaviors of Vickers indentations in soda-lime glass". *Journal of the Ceramic Society of Japan* 116.1356 (2008), pp. 864–868.

[63] S. Yoshida, H. Sawasato, T. Sugawara, Y. Miura, and J. Matsuoka. "Effects of indenter geometry on indentation-induced densification of soda-lime glass". *Journal of Materials Research* 25.11 (2010), pp. 2203–2211.

[64] S. Yoshida, J.-C. Sanglebœuf, and T. Rouxel. "Quantitative evaluation of indentation-induced densification in glass". *Journal of Materials Research* 20.12 (2005), pp. 3404–3412.

[65] Y. Kato, H. Yamazaki, S. Itakura, S. Yoshida, and J. Matsuoka. "Load dependence of densification in glass during Vickers indentation test". *Journal of the Ceramic Society of Japan* 119.1386 (2011), pp. 110–115.

[66] Y. Kato, H. Yamazaki, Y. Kubo, S. Yoshida, J. Matsuoka, and T. AKAI. "Effect of B_2O_3 content on crack initiation under Vickers indentation test". *Journal of Ceramic Society of Japan* 118.9 (2010), pp. 792–798.

[67] Y. Kato, H. Yamazaki, S. Yoshida, J. Matsuoka, and M. Kanzaki. "Measurements of density distribution around Vickers indentation on commercial aluminoborosilicate and soda-lime silicate glasses by using micro Raman spectroscopy". *Journal of Non-Crystalline Solids* 358.24 (2012), pp. 3473–3480.

[68] Y.-G. Jung, A. Pajares, R. Banerjee, and B. R. Lawn. "Strength of silicon, sapphire and glass in the subthreshold flaw region". *Acta Materialia* 52.12 (2004), pp. 3459–3466.

[69] F. Ouchterlony. "Stress intensity factors for the expansion loaded star crack". *Engineering Fracture Mechanics* 8.2 (1976), pp. 447–448.

[70] J. P. Lucas, N. R. Moody, S. L. Robinson, J. Hanrock, and R. Q. Hwang. "Determining fracture toughness of vitreous silica glass". *Scripta Metallurgica et Materialia* 32.5 (1995), pp. 743–748.

[71]   J. J. Mecholsky, R. W. Rice, and S. W. Freiman. "Prediction of Fracture Energy and Flaw Size in Glasses from Measurements of Mirror Size". *Journal of the American Ceramic Society* 57.10 (1974), pp. 440–443.

[72]   S. M. Wiederhorn, H. Johnson, A. M. Diness, and A. H. Heuer. "Fracture of Glass in Vacuum". *75th Annual Meeting, The American Ceramic Society*. Cincinnati, 1974, pp. 336–341.

[73]   H. C. Hyun, F. Rickhey, J. H. Lee, M. Kim, and H. Lee. "Evaluation of indentation fracture toughness for brittle materials based on the cohesive zone finite element method". *Engineering Fracture Mechanics* 134.C (2015), pp. 304–316.

[74]   K. Niihara. "A fracture mechanics analysis of indentation-induced Palmqvist crack in ceramics". *Journal of Materials Science Letters* 2 (1983), pp. 221–223.

[75]   D. Broek. *Elementary engineering fracture mechanics*. 1982.

[76]   C. M. Perrott. "Elastic-plastic indentation: Hardness and fracture". *Wear* 45.3 (1977), pp. 293–309.

[77]   M. V. Swain and J. T. Hagan. "Indentation plasticity and the ensuing fracture of glass". *Journal of Physics D: Applied Physics* 9.1 (1976), pp. 2201–2214.

[78]   J. T. Hagan and S. Van der Zwaag. "Plastic processes in a range of soda-lime-silica glasses". *Journal of Non-Crystalline Solids* 64.1-2 (1984), pp. 249–268.

[79]   D. M. Marsh. "Plastic Flow in Glass". *Proceedings of the Royal Society of London. Series A, Mathematical and Physical Sciences* 279.1378 (1964), pp. 420–435.

[80]   Y.-T. Cheng and C.-M. Cheng. "Scaling relationships in conical indentation of elastic-perfectly plastic solids". *International Journal of Solids and Structures* 36.8 (1999), pp. 1231–1243.

[81]   S. Shim, J. Jang, and G. M. Pharr. "Extraction of flow properties of single-crystal silicon carbide by nanoindentation and finite-element simulation". *Acta Materialia* 56 (2008), pp. 3824–3832.

[82]   A. Bolshakov and G. M. Pharr. "Influences of pileup on the measurement of mechanical properties by load and depth sensing indentation techniques". *Journal of Materials Research* 13.4 (1998), pp. 1049–1058.

[83]   S. Shim, W. C. Oliver, and G. M. Pharr. "A critical examination of the Berkovich vs. conical indentation based on 3D finite element calculation ". *Material Research Society Symposium Proceedings* 841 (2005), R9.5.1–R9.5.6.

[84]   E. G. Herbert, W. C. Oliver, and G. M. Pharr. "On the measurement of yield strength by spherical indentation". *Philosophical Magazine* 86 (2006), pp. 5521–5539.

[85]   K. R. Gadelrab, F. A. Bonilla, and M. Chiesa. "Densification modeling of fused silica under nanoindentation". *Journal of Non-Crystalline Solids* 358.2 (2012), pp. 392–398.

[86]   I. M. Ogilvy, C. M. Perrott, and J. W. Suiter. "On the indentation fracture of cemented carbide part 1—Survey of operative fracture modes". *Wear* 43 (1977), pp. 239–252.

[87]   K. L. Johnson. *Contact Mechanics.* Cambridge University Press, 1985.

[88]   S. S. Chiang, D. B. Marshall, and A. G. Evans. "The response of solids to elastic/plastic indentation. I. Stresses and residual stresses". *Journal of Applied Physics* 53.1 (1982), pp. 298–311.

[89]   G. Feng, S. Qu, Y. Huang, and W. D. Nix. "An analytical expression for the stress field around an elastoplastic indentation/contact". *Acta Materialia* 55.9 (2007), pp. 2929–2938.

[90]   K. I. Schiffmann. "Determination of fracture toughness of bulk materials and thin films by nanoindentation: comparison of different models". *Philosophical Magazine* 91.7-9 (2011), pp. 1163–1178.

[91]   L. Ding, Y. Xu, R. Yang, Y. Yang, R. Lu, H. Liu, H. He, Q. Zheng, and J. C. Mauro. "Lateral-pushing induced surface lift-up during nanoindentation of silicate glass". *Journal of the American Ceramic Society* 105.4 (2022), pp. 2625–2633.

[92]   K. Januchta and M. M. Smedskjaer. "Indentation deformation in oxide glasses: Quantification, structural changes, and relation to cracking". *Journal of Non-Crystalline Solids: X* 1 (2019), p. 100007.

[93]   T. Rouxel, H. Ji, V. Keryvin, T. Hammouda, and S. Yoshida. "Poisson's Ratio and the Glass Network Topology - Relevance to High Pressure Densification and Indentation Behavior". *Advanced Materials Research* 39-40 (2008), pp. 137–146.

[94]   T. Rouxel, J. I. Jang, U. Ramamurty, and 2021. "Indentation of glasses". *Progress in Materials Science* 121 (2021), p. 100834.

[95]   T. Haranoh, H. Ishikawa, N. Shinkai, and M. Mizuhashi. "Crack evolution in Vickers indentation for soda-lime-silica glass". *Journal of Materials Science* 17.5 (1982), pp. 1493–1500.

[96]   M. D. Michel, F. C. Serbena, and C. M. Lepienski. "Effect of temperature on hardness and indentation cracking of fused silica". *Journal of Non-Crystalline Solids* 352.3 (2006), pp. 3550–3555.

[97]   N. Cuadrado, D. Casellas, M. Anglada, and E. Jiménez-Piqué. "Evaluation of fracture toughness of small volumes by means of cube-corner nanoindentation". *Scripta Materialia* 66.9 (2012), pp. 670–673.

[98]   C. Li, L. Zhang, L. Sun, C. Wu, D. Duan, Q. Lin, J. Ding, and Z. Jiang. "A finite element study on the effects of densification on fused silica under indentation". *Ceramics International* 46.17 (2020), pp. 26861–26870.